# ATOMISTIC STUDIES OF STRUCTURE-PROPERTY RELATIONSHIPS IN ACTINIDE AND TRANSITION METAL ALLOYS

A Dissertation
Presented to
The Academic Faculty

by

Jacob Startt

In Partial Fulfillment
of the Requirements for the Degree
Doctor of Philosophy in the
George W. Woodruff School of Mechanical Engineering
Nuclear and Radiological Engineering Programs

Georgia Institute of Technology
May 2020

# ATOMISTIC STUDIES OF STRUCTURE-PROPERTY RELATIONSHIPS IN ACTINIDE AND TRANSITION METAL ALLOYS

Approved by:


Dr. Chaitanya Deo, Advisor
George W. Woodruff School of Mechanical Engineering
*Georgia Institute of Technology*

Dr. Yan Wang
George W. Woodruff School of Mechanical Engineering
*Georgia Institute of Technology*

Dr. Hamid Garmestani
School of Materials Science and Engineering
*Georgia Institute of Technology*

Dr. Preet Singh
School of Materials Science and Engineering
*Georgia Institute of Technology*

Dr. Farzad Rahnema
George W. Woodruff School of Mechanical Engineering
*Georgia Institute of Technology*

Dr. Stephen Raiman
Materials Science and Technology Division
*Oak Ridge National Laboratory*


Date Approved: March 25,2020

# ACKNOWLEDGEMENTS

I want to thank first my advisor Dr. Chaitanya Deo for his guidance and instruction while at Georgia Tech and for providing me the opportunity to pursue a doctorate degree early on in my grad school career. I want to thank Dr. Stephen Raiman for his guidance and mentorship, in addition to Oak Ridge National Laboratory, for providing me with an internship opportunity in the Corrosion Group at ORNL. Then I would also like to thank Dr. Remi Dingreville for his assistance and instruction in corrosion related modelling and for providing me an internship opportunity in the nanoscale-physics group at Sandia National lab. Finally, I would also like to thank Dr. Hamid Garmestani for serving as an almost co-advisor during the first half of my grad school career, and for the guidance and opportunity he provided, allowing me to diversify my research focus across both computational and experimental practices.

I would like to thank my friends and family for all of their support both before and during my time in grad school. I would not have made it here without the constant care and support of my mom and dad, and from my two older, but smaller brothers. I also could not have done this without the support and friendship of several people. My childhood friends from Easton have been by my side the entire way and have shared all of my ups and downs. My time at Washington College provided me with some the greatest friends and relationships I will ever have, and I will always be grateful for my time there. Then my friends from Georgia Tech and Atlanta, whether pursuing their own graduate degrees, or just doing their own thing, shared this experience with me and were paramount to me making it through and getting to this point. I could not have done this without any of them.

# TABLE OF CONTENTS

# LIST OF TABLES

# LIST OF FIGURES

# LIST OF SYMBOLS AND ABBREVIATIONS

| | |
|---|---|
| ADSR | accelerator driven subcritical reactor |
| AES | Auger electron spectroscopy |
| AM05 | Armiento-Mattsson 2005 |
| APT | atom probe tomography |
| ARE | aircraft reactor experiment |
| ASA | atomic sphere approximation |
| bcc | body-centered cubic |
| BO | Born-Oppenheimer |
| BWR | boiling water reactor |
| CDD | charge density difference |
| CPA | coherent potential approximation |
| DB | dumbbell |
| DFT | density functional theory |
| EBR | experimental breeder reactor |
| EMTO | exact muffin-tin orbital method |
| FBR | fast breeder reactor |
| fcc | Face-centered cubic |
| FP-LMTO | Full-potential linear muffin-tin orbital |
| GF-KKR | Green's Function Korringa-Kohn-Rostoker |
| GF-LMTO | Green's function linear-muffin-tin-orbital |
| GGA | generalized gradient approximation |
| GTRI | Global Threat Reduction Initiative |

| | |
|---|---|
| GPa | giga-Pascal |
| HEG | homogeneous electron gas |
| HF | Hartree-Fock |
| kMC | kinetic Monte Carlo |
| LDA | local density approximation |
| LEED | low-energy electron diffraction |
| LEU | low-enriched uranium |
| LMFBR | liquid metal-cooled fast breeder reactor |
| LMTO | linear muffin-tin orbital |
| LSGF | locally self-consistent Green's function |
| MD | molecular dynamics |
| MSR | molten salt reactor |
| MSRE | molten salt reactor experiment |
| NEB | nudged elastic band |
| NN | nearest neighbor |
| PAS | positron annihilation spectroscopy |
| PAW | projector augmented wave |
| PBC | periodic boundary condition |
| PBE | Perdew-Burke-Ernzerhof |
| PKA | primary knock-on atom |
| RDF | radial distribution function |
| RPBE | revised Perdew-Burke-Ernzerhof |
| SIE | self-interaction error |
| SCLS | surface core level binding energy shifts |
| sp | spin-polarization |

| | |
|---|---|
| SOC | spin-orbit coupling |
| SQS | special quasi-random structure |
| TB | tight-binding |
| TEM | transmission electron microscope |
| TM | transition metal |
| VASP | Vienna Ab initio Simulation Package |
| XC | exchange-correlation |
| XPS | X-ray photo-electron spectroscopy |

# SUMMARY

In this thesis, structure-property relationships are investigated for a series of nuclear material systems using density functional theory (DFT). Each chapter presents a unique problem within the field of nuclear materials engineering and can demonstrate the application of computational methods in support of existing experimental framework or in the guidance or suggestion of new experimental investigation.

In the first project, point defect formation energies in Th and Th-U metal are modeled using DFT. These defects often have a large effect on a material's mechanical properties and in the highly radioactive environment of a reactor core defects are readily created near the displacement cascades of primary knock-on atoms (PKAs). The second project comprises an investigation of Cr depletion in Ni-Cr surfaces in molten salt reactors. The depletion of Cr atoms in the surface regions of these materials has been observed as the dominant form of corrosion but the underlying mechanisms and driving forces are not well understood. In this project, DFT is used to model the segregation behavior of Cr in fcc Ni surfaces. The oscillatory nature of the segregation energy profile is then discussed in terms of charge transfer and lattice distortion effects. In the third project, DFT is again used to extend the investigation of Cr segregation behaviors, with a focus aimed at understanding the effects of adsorbed salt atoms on segregation behavior near the surface of a Ni-Cr alloy. An emphasis is placed on the relative effects of cations and anions in the molten salt, and on the relative effects of natural salt components versus salt impurities. In the fourth and final project, an understanding is sought for the atomic ordering behavior in U-Zr, an alloy under investigation for use as a metallic fuel in advanced fast nuclear

reactors. In these metals there is a potential for phase decomposition and a redistribution of fissile U atoms and so a complete understanding of the atomic ordering behavior in U-Zr is therefore needed. DFT is employed to investigate this ordering behavior.

# CHAPTER 1. INTRODUCTION

In nuclear power systems, the choice and design of structural components and fuel materials are subject to an often strict and severe level of scrutiny. In these systems it is necessary to choose materials which provide not only the greatest overall economic efficiency and structural performance but materials which also possess inherent stability and passive safety behavior during transient and off-normal reactor events. The elemental components and microstructural makeups of these materials, which are often metallic alloys, must be carefully tailored and prepared so that stable and sufficient neutron fluxes can be achieved and sufficiently maintained.

It is not surprising then that the compositions of these alloys, as well as the specific metals that make them up, can vary greatly from one type of structural component to next all within the same reactor core. It should be even less surprising that the range of suitable alloys and their compositions used in the many different types of reactor design variants can vary to a much greater extent, as many of the different advanced reactor concepts are based on fundamentally different forms of operation. The alloy used to make the reactor core vessel in a molten salt reactor (MSR) is almost surely not going to be the same alloy used to make the reactor core vessel in a boiling water reactor (BWR), for instance.

## 1.1 Metal Alloy Development for Nuclear Systems

It's rare for a common metal or metal alloy to possess every single quality or property that might be desired of it for the specific task at hand or structural function. Often one is faced with making a compromise for an alloy which possesses most of the desired

properties, but which also might come with some small level or degree of undesirable behaviors or characteristics. The goal of scientific research into alloy development is focused on removing or limiting these undesirable qualities while improving or preserving the good qualities. In some cases, the goal may instead be to replicate the desirable properties in other similar materials that do not possess negative traits.

These undesirable features often concern the behavior of the metal when it undergoes harsh conditions such as high temperatures, where potential phase changes, volume expansions, or the formation of intermetallic phases can occur during the operational lifetime of the component. Or they may result in response to high or increased levels of irradiation when changes in defect formation, accumulation, and diffusion properties could totally alter the performance of the material. In other cases, we are concerned with the ability of a metal to handle perpetually harsh conditions, such as the corrosive or degradative conditions present inside molten salt reactors, which are of a more chemical nature.

## 1.2 Thesis Outline

In this thesis, four scientific studies concerning the behavior of transition and actinide metal material systems will be presented and discussed. The primary scientific tool employed in each of these studies is density functional theory (DFT), a computational electronic structure modeling framework in which the quantum mechanical behaviors of a material are studied to better understand macroscopic phenomena. In DFT, the groundstate electronic wavefunction is determined by solving the Schrödinger equation in terms of electron density, allowing us to probe the most fundamental characteristics and properties

underlying the behavior and performance of the subject materials in many different types of reactor conditions. Each study presents a unique problem within the field of nuclear materials engineering and can demonstrate the application of computational materials modelling in support of existing experimental frameworks or in the guidance or suggestion of new experimental investigation.

The rest of this chapter will serve as an introduction to each of the four studies, briefly describing their relevance and necessity. Next, in CHAPTER 2, I will provide a brief introductory level description of DFT and electronic structure theory modelling. Then, each chapter after this, beginning with CHAPTER 3, will be devoted to one of the four studies, which will each be presented as its own contained research report. Finally, a conclusion and summary will be given in CHAPTER 7.

### *1.2.1 Study I: Point Defects in Metallic Thorium*

In this first study, formation energies of various point defects in the atomic lattices of Th and Th-U metals are calculated with DFT. Point defects refer to sites in a lattice where an atom is either missing (*i.e.,* vacancy) or where an atom is jammed in between lattice sites (*i.e.,* interstitial). These defects often have a large effect on the mechanical properties of materials and in the highly radioactive environment of a reactor core defects are readily created during the displacement cascades of primary knock-on atoms (PKAs).

### *1.2.2 Study II: Oscillatory Segregation behavior in Nickel-Chrome Surfaces*

In MSRs, the corrosion of the salt containing pipes and structures is a major concern. The fundamental, or atomic level mechanisms of this corrosion are not well

understood, but it is always accompanied, or possibly even driven, by some form of Cr depletion. In study II, the fundamental behavior of Cr in a Ni surface is investigated. A segregation energy profile for Cr under a clean surface (*i.e.*, under vacuum) is found using DFT, and then analyzed and explained according to the unique behaviors of Cr and Ni alloys observed in the calculations. This segregation behavior, which will be shown to have an oscillatory type shape, and be driven by charge transfer effects, will serve as the basis or reference for subsequent corrosion and surface segregation studies in Ni-Cr alloys.

### *1.2.3 Study III: The Influence of Molten Salt Species on Segregation Behaviors in Nickel-Chrome Surfaces*

The third study again focuses on corrosion related surface behaviors in Ni-Cr alloys. In what can really be thought of as an extension or a part two to the work presented in Study II (Chapter 4), Study III investigates the effects of various absorbed salt species on the segregation of Cr in Ni. As will be shown in Study II, Cr expresses a very particular segregation behavior in Ni surfaces under a clean surface or vacuum, and so the emphasis of Study III will be to evaluate that behavior, or better stated, the changes in that behavior when components of molten salts are adsorbed to the top of the surface and able to interact with the Cr as it segregates. An emphasis will be placed on the relative effects of normal salt components, such as the anions F and Cl, compared with the effects of salt impurities, such as O or H.

### *1.2.4 Study IV: Atomic Ordering in U-Zr Metallic Fuels*

In this final study, the atomic ordering in δ-U-$Zr_2$ is investigated using DFT. There is uncertainty regarding the exact ordering of the B-sites in the $AlB_2$ type structure

exhibited by this U-Zr intermetallic phase. In study IV, several supercell structures which test the ordering in these sites are constructed and modelled using similar DFT techniques used in studies I-III. To gauge, the relative stability of order variants, formation enthalpies are calculated for each structure and compared with experimental values from literature. Specific focus is placed on the structural relaxation behavior of U atoms in regards their nearby coordination of other U atoms.

# CHAPTER 2. THEORETICAL BACKGROUND

The work presented in each remaining chapter of this thesis is dependent on the use of density functional theory (DFT). In this atomistic approach to modelling material behaviors, atoms are modelled down to their individual electrons according to the laws of quantum mechanics. As such, these calculations can be performed without needing to be informed by empirical data, and so are deemed to be *ab initio* or from first-principles. Thus, no prior knowledge of material system's properties is necessary for it to be modelled with DFT or any other first-principles methods. Although, in practice, some intelligent/informed guesses about the materials microstructural properties are often necessary to achieve reasonable calculation times.

A full understanding of density functional theory is best served by looking back and exploring the history of its foundations, rooted in the earliest mean-field electronic structure theory models. Therefore, in the rest of this chapter I will provide a brief description of the development of electronic structure theory, beginning first with the two foundational assumptions employed in all such practical models. Firstly, that a material's properties are uniquely determined by the behavior of its electrons, and secondly, that the nuclei are so much more massive and slower moving than the electrons that the relative motion of the electrons can be said to be instantaneous.

## 2.1 The Schrödinger Equation

The first of these assumptions is uniquely referring to the Schrödinger equation and its description of the motion of the nuclei and electrons in a given material system. For a

system of $N$ electrons and $M$ nuclei at positions of $r_i$ for $i = 1 \ldots N$ and $R_j$ for $j = 1 \ldots M$, which can be described by the many-body wavefunction, $\Psi$, the time-dependent Schrodinger equation is

$$i\hbar \frac{\partial \Psi(r_1, \ldots, r_N, R_1, \ldots, R_M, t)}{\partial t} = H\Psi(r_1, \ldots, r_N, R_1, \ldots, R_M, t) \tag{1}$$

where $H$ is the many-body Hamiltonian, containing the kinetic energy ($T$) and potential energy ($V$) operators of the $M$ nuclei with mass $M_j$, and $N$ electrons with mass $m$, as follows

$$H = T_{M_i} + T_m + V_{M_j - M_j} + V_{m - M_j} + V_{m-m} \tag{2}$$

Written out completely, the Hamiltonian takes the form

$$\begin{aligned} H = & \sum_{i=1}^{M} -\frac{\hbar^2 \nabla_{R_j}^2}{2M_j} + \sum_{k=1}^{N} -\frac{\hbar^2 \nabla_{r_k}^2}{2m} + \frac{1}{2} \sum_{\substack{i=1,k=1 \\ i \neq k}}^{M,M} \frac{Z_i Z_k e^2}{|R_i - R_j|} + \frac{1}{2} \sum_{\substack{k=1,l=1 \\ k \neq l}}^{N,N} \frac{e^2}{|r_k - r_l|} \\ & - \sum_{k=1,i=1}^{N,M} \frac{Z_i e^2}{|r_k - R_i|} \end{aligned} \tag{3}$$

where $e$ is just the charge of the electron and $Z_i$ is the charge of the $i$th nucleus. The first two terms in equation (3) correspond to the kinetic energy of the nuclei and electrons, while the three remaining terms describe the potential energy of the nuclei-nuclei, electron-electron, and electron-nuclei interactions.

Outside of relativistic effects, equation (3) contains much of the information one could want to know regarding the electronic behavior of a material, however, in its current

state it is too difficult to solve for anything but the simplest of cases. In order to make this more manageable we must invoke the second of the two assumptions that are fundamental to the electronic structure theory models.

## 2.2 The Born-Oppenheimer Approximation

An atomic nucleus is massive in relation to an electron, and because of this the electrons are able to move and accelerate much more quickly than the nuclei. The difference in relative mass and acceleration is so extreme, in fact, the electrons are essentially able to respond instantaneously to the movement of the nuclei. This is the basis of the Born-Oppenheimer (BO) approximation, which states that the movement of the nuclei and electrons can be decoupled.

The BO approximation allows us to do two things. First, we can treat the nuclei as if they were static, meaning we only need to solve for the groundstate wavefunction of the electrons around the static nuclei positions. This allows us to reduce equation 41 into the time-independent form of the Schrodinger equation with the form

$$H_{el}\psi(r_1, \dots, r_N) = E_{el}\psi(r_1, \dots, r_N) \tag{4}$$

where $H_{el}$ is the new "clamped-nuclei" Hamiltonian operator, and $E_{el}$ is total energy eigenvalue of the many-body wavefunction, $\psi$, corresponding to just the electrons. Secondly, since the nuclei are now static, this new "clamped-nuclei" Hamiltonian operator, $H_{el}$, takes the form of

$$H_{el} = T_m + V_{m-M_j} + V_{m-m} + V_{ext} \quad (5)$$

where the kinetic energy term of the nuclei has been removed, and the potential energy term corresponding to the nuclei-nuclei interaction has been replaced with a constant $V_{ext}$ term, that serves only to shift the energy eigenvalues by some amount corresponding the average potential field of the nuclei.

Now that the problem has been reduced to the time-independent case, and the Hamiltonian has been partially simplified, the remaining terms that need to be handled are those related to the many-body electron-electron interaction. This is where the main differences between most variants of electronic structure models come into play. Rather than jumping straight into DFT, however, it is helpful to first introduce another electronic structure model, Hartree-Fock (HF) Theory, which both preceded DFT and is still in use today, as it shares many of the same approximations and tricks employed in DFT. This will offer a unique perspective which will help to understand some of the more fundamental aspects of DFT, as well as highlighting DFT's advantages and drawbacks, while also allowing for a more thorough introduction of the ultra-important exchange term of the exchange-correlation behaviors buried in the electron-electron interaction term.

In addition to the assumptions already mentioned, the most successful electronic structure theory models all share a single-particle approach to solving for the groundstate electronic wavefunction of the system. Hartree-Fock Theory explicitly uses this approach to solve for the groundstate wavefunction of the system.

## 2.3 Hartree-Fock Theory

In Hartree-Fock (HF) theory the goal is to calculate the wave-function [1], distinguishing it from DFT methods, which as we will soon see in section 142.4, are set on finding the electron density instead. HF theory assumes that the exact many-body electronic wavefunction, $\psi$, can be approximated by a Slater determinant of single-particle spin-orbitals

$$\psi(\mathrm{x}_1, \mathrm{x}_2 \ldots, \mathrm{x}_N) = \frac{1}{\sqrt{N!}} \begin{vmatrix} \chi_1(\mathrm{x}_1) & \chi_2(\mathrm{x}_1) & \ldots & \chi_N(\mathrm{x}_1) \\ \chi_1(\mathrm{x}_2) & \chi_2(\mathrm{x}_2) & \ldots & \chi_N(\mathrm{x}_2) \\ \vdots & \vdots & \ddots & \vdots \\ \chi_1(\mathrm{x}_N) & \chi_2(\mathrm{x}_N) & \ldots & \chi_N(\mathrm{x}_N) \end{vmatrix} \tag{6}$$

for a system of N electrons each with spin-orbital $\chi_N$ and position $\mathrm{x}_N$.

### *2.3.1 The Antisymmetry Principle*

In the original derivation of Hartree theory, which only just preceded HF theory, only a simple product of single body wave-functions was used to represent the wavefunction. This, however, meant that the many-body wavefunction was not antisymmetric with the respect to the exchange of any two electrons. This is a condition of the Pauli exclusion principle that requires a sign change of the wave-function accompany the interchange of two fermions, which was not possible with just a simple product wavefunction formulation. In HF theory, the antisymmetry principle is automatically obeyed through the use of the Slater determinant and the resulting energy change is termed the *exchange energy*. Additionally, the Slater determinant satisfies the other important conditions of the Pauli Exclusion principle in that every electron becomes indistinguishable

from one another while also causing the wavefunction to disappear to zero if two electrons are made to share the same position.

An interesting consequence of describing the electrons through a Slater determinant (*i.e.*, an antisymmetrized product) and another way to understand the exchange energy, is that we are treating the electrons as if they are able to move independently of one another, only feeling the coulomb repulsion from the average position of *all* electrons. Thus, the exchange energy refers to the reduction in coulomb energy of the system due to the spatial separation of like-spin electrons.

### *2.3.2 Mean-Field Approximation*

By treating the electrons as essentially independent particles within a mean-field determined by all electrons in the systems HF theory is employing what is commonly referred to as a mean-field or single-particle approach to solving the Schrödinger equation. In practice, this is done by first rewriting the Schrodinger equation in terms of the HF spin-orbitals

$$\left[-\frac{\hbar^2}{2m}\nabla^2 + V(r) + V_H(r)\right]\chi_j(\mathrm{x}) = E_j\chi_j(\mathrm{x}) \tag{7}$$

where $V(r)$ is the potential due to the ions, and $V_H(r)$ is referred to as the Hartree potential, which describes the Coulomb repulsion between a single electron and the total electron density, $n(r)$, of the system. The Hartree potential has the form

$$V_H(r) = e^2 \int \frac{n(r')}{|r - r'|} d^3r' \tag{8}$$

where the electron density, $n(r)$, is found by

$$n(r) = 2 \sum_i \psi_i^*(r)\psi_i(r) \tag{9}$$

The form of $V_H(r)$ should make it clear that the electronic wavefunction calculation in HF theory is uniquely dependent on a mean-field approximation of the average electron density.

With the single-particle approach defined, the procedure used to solve for the groundstate electronic wavefunction from this point is actually remarkably similar to the method employed by DFT models. In an $N$ electron system we must now find the $N$ lowest energy spin-orbitals corresponding to the single-electron functions $\chi_j(\mathrm{x})$ for $j = 1 \ldots N$. The total many-body wavefunction is then found from these functions through the Slater determinant defined in equation (6). This task is relatively straightforward, however, in practice these equations must be solved on a computer, and so the spin-orbitals, which are continuous functions, must be numerically approximated in some way.

### *2.3.3 Basis Sets*

The numerical representation of spin-orbitals is done through the use of an appropriately chosen basis set. We can represent each spin-orbital wavefunction as a summation over several basis functions, $\Phi_i(\mathrm{x})$, as

$$\chi_j(\mathrm{x}) = \sum_{i=1}^{K} \alpha_{ji} \Phi_i(\mathrm{x}) \tag{10}$$

where $\alpha_{ji}$ is an expansion coefficient and the summation is over the necessary number, $K$, of functions needed to accurately approximate the orbital. Thus, a higher number of basis functions per orbital will generally result in greater accuracy, but usually at the cost of computational efficiency. The choice of an appropriate basis function is also vital to achieving accuracy and reducing computational expense. The development of more accurate and more computationally efficient basis orbitals is an on-going area of research in both HF and DFT methods.

### *2.3.4 A Self-Consistent Scheme*

Now that the many-body wavefunction has been rewritten in terms of numerically solvable single-particle spin-orbitals we can define the iterative approach necessary to solve for the groundstate wavefunction. A problem that arises with this, however, is that in order to solve for the individual spin-orbitals, we must first know the electron density, $n(r)$, but in order to know the electron density, we must first know the total electronic wavefunction, which as the focus of the entire calculation we cannot possibly the exact form of at the start!

Getting around this problem is not actually that difficult, however, as we just need to provide an "educated guess" to determine the initial electronic wavefunction for the system. In HF theory, this initial guess is made for the expansion coefficients, $\alpha_{ji}$, which allows for an initial determination of the spin-orbitals, $\chi_j(\mathrm{x})$. From this the corresponding

total wavefunction can be found, along with the electron density, $n(r)$. Then through standard diagonalization methods a new $\alpha_{ji}$ coefficient matrix can be found.

This process can be repeated iteratively until the change observed in subsequent coefficient matrices falls below some threshold value. At this point we have "minimized" the electronic groundstate wavefunction corresponding to our initial guess of the ionic positions. This wavefunction can then be used to calculate the forces on the nuclei, whose positions can then be "updated" accordingly. This ionic update represents an outer ionic iteration loop in relation to the inner electronic wavefunction loop. For every new set of atomic positions, a new wavefunction is iteratively calculated and the entire self-consistent iterative process is repeated until some final convergence criteria for the ionic minimalization loop has been reached.

Now that an initial prescription for the calculation of electronic wavefunctions has been laid out, and the most relevant and important methods and approximations used in HF theory have been described, we can finally turn our attention to DFT.

## 2.4 Density Functional Theory

As noted in the previous section, the main difference between Hartree-Fock theory and density functional theory is the quantity being calculated. In HF theory, the electronic wavefunction of the groundstate is directly calculated. In DFT, we instead seek to calculate the groundstate electron density, $n(r)$. The validity of this approach was first proven by Kohn and Hohenberg in the 1960s when they derived two fundamental theorems which together stand as the foundations of all DFT methods.

### *2.4.1 The Hohenberg-Kohn Theorems*

The first of these theorems states *that the total energy of the groundstate system is a unique functional of the electron density* [2]. In other words, we can state the groundstate energy as

$$E[n(r)] \tag{11}$$

where $n(r)$ is the same electron density from earlier and the brackets denote a functional form, or in other words, the energy is a function of the electron density function. This is where DFT gets its name. The implication of this first theorem is that the electron density uniquely determines all the important properties of the system, including the Hamiltonian, which in turn fully determines the wavefunction of each state in the system.

So, in short, a functional of the electron density can be used to solve the Schrödinger equation, as opposed to the wavefunction, dramatically reducing the dimensionality of the problem from one containing $4N$ variables ($N$ being the number of electrons each with three cartesian variables and one spin variable) to a problem consisting of just the four variables required to define the electron density at any location within the system.

The second of these two theorems, equally as important as the first, introduces a variational principle, and states that *the electron density which is able to minimize the energy functional corresponds the true electron density groundstate of the system that would be found through the exact solution to the Schrödinger equation* [3]. This is hugely important as it provides a path for solving for the true groundstate wavefunction of an $N$

particle system, without having to actually solve the intractable $N$-body Schrödinger problem.

### *2.4.2 The Kohn-Sham Equations*

Before we can actually begin to solve for the groundstate of a system, we must first find a corresponding form of the Schrödinger equation which can be solved for using the electron density. This was the basis of the work of Kohn and Sham, in which they developed a method to solve for the electron density using a single electron mean-field approach, like that used in HF theory.

In describing the method they developed, it is helpful to first write down the energy functional in terms of the many single-body wavefunctions, $\psi_i$, corresponding to the individual electrons of a system

$$E[\{\psi_i\}] = E_{known}[\{\psi_i\}] + E_{XC}[\{\psi_i\}] \tag{12}$$

Here, the functional has been split into a linear combination of two functionals which correspond to the terms for which we know the true analytical form ($E_{known}[\{\psi_i\}]$) and those for which we do not know the true form ($E_{XC}[\{\psi_i\}]$). The known terms include the kinetic energy of the electrons, the electron-nuclei Coulomb interaction, the electron-electron Coulomb interaction, and the nuclei-nuclei Coulomb interactions. Written out in that order this looks like

$$E_{known}[\{\psi_i\}] = -\frac{\hbar^2}{m}\sum_i \int \psi_i^* \nabla^2 \psi_i d^3r + \int V(r)n(r)d^3r + \frac{e^2}{2}\iint \frac{n(r)n(r')}{|r-r'|} d^3r d^3r' + E_{ion} \quad (13)$$

The unknown term in equation (12), $E_{XC}[\{\psi_i\}]$, is known as the exchange-correlation functional, and will be discussed further, in a following section.

With this distinction between known and unknown components, the Kohn-Sham equations can be written for the single-electron wavefunctions as

$$\left[-\frac{\hbar^2}{2m}\nabla^2 + V_{eff}(r)\right]\psi_i(r) = \varepsilon_i \psi_i(r) \quad (14)$$

where $V_{eff}(r)$ is an effective potential and is written as

$$V_{eff}(r) = V_{ext}(r) + e^2 \int \frac{n(r)n(r')}{|r-r'|} d^3r' + \frac{\delta E_{XC}[n(r)]}{\delta n(r)} \quad (15)$$

where $V_{ext}$ represents the energy of the electron interaction with the static ion potential field and the second term is the same as the Hartree potential found in section 2.3.2, and represents the Coulomb repulsion between the single electron, $i$, and the electron density, $n(r)$. Since $n(r)$ is defined by all electrons in the system, this Hartree potential actually includes a self-interaction error (SIE), in which the electron is essentially experiencing a spurious interaction with itself due to its own part in the average electron density. The density is not able to be found minus the contribution from a single electron and so the correction for the SIE must be included in the third term on the right in equation

(15), which is the functional derivative of the exchange-correlation energy, $E_{XC}$, representing the unknown terms.

This exchange-correlation functional is the only term in the Kohn-Sham equations that cannot be evaluated exactly as its true form is currently not known. Finding an exact solution or developing better and more accurate approximations for the exchange-correlation functional stands as one of biggest areas of open research in modern DFT development efforts.

Solving the Kohn-Sham equations involves a self-consistent procedure similar to the one employed in HF theory. The scheme for DFT involves the following steps:

1. Provide a guess for the initial electron density $n(r)$ for a system of ions.
2. Calculate the effective potential, $V_{eff}(r)$, corresponding to the ionic positions and trial electron density.
3. Solve the Kohn-Sham equations (eq. (13)) to find the single-electron wavefunctions, $\psi_i$(r), corresponding to each electron in the system.
4. Use these single-electron wavefunctions to calculate a new electron density $n_{KS}(r) = 2\sum_i \psi_i^*(r)\psi_i(r)$ via a mixing scheme utilizing the densities from previous steps [4,5].
5. Compare the new density, $n_{KS}(r)$, with the old density used to find the single-particle wavefunctions, and if the difference is below a specified threshold value then the calculation has converged. If not, then steps 2-4 should be repeated until convergence has been met.

Once the electron density has been found for a particular set of ionic positions, an outer ionic loop, similar to the one used in HF theory, can be used to update the system. Once the exact groundstate electron density has been found the total energy can be found using the Kohn-Sham energy functional (eq. (13)).

### *2.4.3 Exchange Correlation Functional*

The real genius of Kohn and Sham's work in developing DFT was to gather all of the terms for which we do not know the true form and to stuff them into a single term at the end of the energy functional. The resulting exchange-correlation energy, $E_{XC}[n(r)]$ is thus a collection of all of the parts of the many-body interaction which are not able to be accounted for in the mean-field approximation. This primarily consists of three things: (i) the exchange energy, coming from the antisymmetry of fermion wavefunctions, (ii) the correlation energy, related to the interacting part of the electron kinetic energy, and (iii) the SIE correction stemming the single-particle mean-field approximation.

#### 2.4.3.1 Correlation Energy

The exchange energy and SIE correction have already been given some attention, and so now I will provide a brief description of the correlation energy. This effect is related to the spatial correlation of electrons around a nucleus. In the mean-field approximation, in which the wavefunction of a single electron is found according to the average position of all electrons (*i.e.*, the average electron density), the exact positions of the "other" electrons are lost. In practice, this approximation introduces an error because electrons are affected by the position of other nearby electrons.

An easy way to envision this spatial correlation is to imagine two electrons around a single nucleus. These electrons repel each other, and so if one electron is on one side of the nucleus, the second electron is likely to be found on the other side. These electrons are spatially correlated, but our average density approximation will undoubtedly lose some of this spatial information.

The correlation energy can usually be defined as the difference between the exact energy of the groundstate and the Hartree-Fock energy in a complete basis set (referred to as the Hartree-Fock limit)

$$E_{corr} = \varepsilon_{exact} - E_{HF}^{\infty} \tag{16}$$

We can see from this that the HF approximation will always underestimate the energy contribution coming from repulsions between nearby electrons. As stated before, the extent of this underestimation and the true mathematical form of the correlation energy contribution to the energy functional is not known and is an active area electronic structure theory research.

We do not know the exact form of the exchange-correlation functional, so in order to solve the Kohn-Sham equations for a system, an approximation to the functional must be made. Luckily, however, we do know enough about the nature of the interactions buried in the functional to be able to develop some reasonable approximations that have so far been able to yield some fairly accurate results. One of the first of these approximations to find wide success was the linear density approximation (LDA).

#### 2.4.3.2 Local Density Approximation

The LDA is a relatively simple approximation to the exchange-correlation functional [6,7]. In the LDA, it is assumed that the exchange-correlation energy per electron, $\epsilon_{xc}(n(r))$ is equal to the exchange-correlation energy of a homogenous electron gas (HEG), $\epsilon_{xc}^{HEG}(n(r))$, which has been found through rigorous quantum Monte Carlo calculations [8,9]. This approximation is considered simple because in an HEG the electron density is considered constant at all points in space. This then makes the approximation one that depends only on the local value of $\epsilon_{xc}(n(r))$, with the form

$$E_{xc}^{LDA}[n(r)] = \int n(r)\epsilon_{xc}^{HEG}\big(n(r)\big)d^3r \tag{17}$$

Because the LDA assumes a constant electron density, it is only truly valid for systems with slowly varying electron density. Despite this, however, the LDA has shown a surprising amount of success in describing both systems that fit this description and those that deviate from the constant electron density in the HEG. However, the LDA does tend to slightly underpredict the groundstate energy while over predicting binding energies, resulting in too short of bond distances. While this is not always the case, today the LDA today is often outperformed by more modern and recently developed functionals. Such as the type described next.

#### 2.4.3.3 Generalized Gradient Approximation

The next level of exchange-correlation approximation we will discuss is essentially an extension of the LDA and is probably the most widely employed and successful type of

functional used for modelling solid-state systems to this day. These are the generalized gradient approximations (GGA), in which the functional is not just dependent on the local electron density but also now on the gradient of the electron density [10,11].

The gradient is incorporated into the functional through the inclusion of a new function in the functional as follows

$$E_{xc}^{GGA}[n(r)] = \int n(r)\epsilon_{xc}^{HEG}\big(n(r)\big)F_{xc}(n,|Cn|)d^3r \tag{18}$$

This new function, $F_{xc}(n,|\nabla n|)$, is called the enhancement factor and as can be seen has a dependency on both the local density and the gradient of the local density. In solid-state modeling there are several variants or "flavors" of GGA functionals that are often employed for different tasks, and the main differences between these GGA functionals usually come in analytical form of the enhancement factor. This is something that will be discussed briefly in CHAPTER 3.

Relative to the LDA, GGAs usually provide improved atomic and molecular energies and correct for the over binding of LDA, however, sometimes this becomes an overcorrection, resulting in a softening of bonds and lattice constants that are too large.

### *2.4.4 Further Approximations*

We began this discussion by first reviewing the major assumptions that serve as the foundation of all electronic structure theory models and then we reviewed the approximations that define and make up the single-particle mean-field approaches that make the calculation of electronic wavefunctions possible. Lastly, the fundamental

theorems underlying DFT and the distinction between the known and unknown components of the Kohn-Sham energy functional were presented. To round-out our discussion of the theoretical methods employed in this thesis, we will now briefly go over the remaining approximations that are pertinent to the specific DFT methods employed this thesis. This will include brief discussions of the periodic boundaries necessary to model the repeating structures of solid-state systems, k-point sampling, the form of the basis sets used to represent the atomic orbitals in our problems, and the use of pseudopotentials in modelling an atom's valence electrons.

#### 2.4.4.1 Periodic Boundaries and k-point Sampling

At a nanoscale level, in which only a handful of atoms are in focus, solid-state systems must necessarily be thought of as extending infinitely into each of the x, y and z directions. A single unit cell containing just a few atoms, representing the most basic repeatable structure of the lattice, is used to describe the crystal structure of these systems. The infinite structure is made up an infinite number of repetitions of this primitive unit cell in each of the principal directions. As such, it is possible to completely define all of the relevant properties and quantities pertaining to any one crystal structure system by evaluating the electronic structure behavior within just one unit cell.

In most electronic structure models, including DFT and HF theory, this is done through the use of periodic boundary conditions (PBCs). In this instance, the simulation cell is treated as one unit cell, the inside of which is being modeled in the calculation, while the repeating structures outside the cell correspond to images of the single simulation cell.

Even with PBCs, we must still find a way to avoid having to calculate the wavefunctions of an infinite number of electrons. In practice, this is done using Bloch's theorem, which for a system of repeating structures allows one to write the energy eigenstates of the wavefunction as

$$\Phi_k(r) = e^{ik\cdot r}u_k(r) \tag{19}$$

where $u_k(r)$ is a periodic function matching the repetition of the primitive unit cell. The wave-vector $k$ is the crystal momentum of the electron and is unique only within a reciprocal space translation given by the reciprocal space lattice vector such that, $k = k + b_n$, where $b_n$ is a multiple of the reciprocal lattice vector in one dimension. Thus, k can be uniquely defined in each of the three principal directions of the unit cell [12].

As the energy eigenstates are now described by k-space, the important information sought in a calculation (*e.g.*, the energy, etc.) must now be found by integrating across the first Brillouin zone of reciprocal k-space. This means we have replaced the infinite sum over all electrons with an integral of the k-space corresponding to just one reciprocal lattice vector translation. Of course, this an analytical problem that we must now solve numerically using a computer, and so instead integrating over the entirety of k-space, we choose special k-points at unique locations where we can numerically evaluate and sum the integrals.

#### 2.4.4.2 Plane-waves

In order to find solutions using the periodic Bloch function approach of equation (19), we must choose a suitable basis-set expansion for $u_k(r)$. In DFT, one of the most popular choices is to expand the periodic function in terms of plane-waves [13,14], like so

$$u_k(r) = \sum_n c_{n,k} e^{ib_n \cdot r} \tag{20}$$

where n is the total number of plane-waves used in the expansion and $c_{n,k}$ is a coefficient matrix. When we put this back into equation (19), we get

$$\Phi_k(r) = \sum_n c_{n,k} e^{i(b_n + k) \cdot r} \tag{21}$$

In order to make this infinite summation possible to solve, we must truncate it according to a specified energy cut-off $E_{cut}$, of the form

$$E_{cut} = \frac{1}{2} |b_{cut} + k|^2 \tag{22}$$

in which the summation is truncated for the plane-waves whose wavevectors are greater than $b_{cut}$.

#### 2.4.4.3 Pseudopotentials

Before we can finish this discussion of DFT and electronic structure theory modeling, we must discuss one more component of these models which is crucial in

allowing us to perform calculations large enough to tell us something interesting about the material system while keeping the cost of the computation to a minimum.

The component in question here is the use of pseudopotentials to approximate the inner core electrons of each nuclei. In this technique, both the nucleus and the inner most non-interacting electrons, which often play no part in bonding, are replaced with a smooth potential leaving only the valence electrons to be treated explicitly by the calculation. This approximation provides two rather significant benefits which greatly improve the computational cost and efficiency of the calculation: (i) the total number of electrons in the calculation is reduced, allowing for faster computational times, and (ii) the wavefunctions near the core, which can vary significantly and rapidly, instead become smooth, greatly reducing the complexity of the basis sets necessary to accurately model the orbitals.

## 2.5 The VASP Implementation of DFT

The implementation of the DFT methods in this thesis could be considered mostly standard for solid-state modelling and in metal and metal alloy investigation. There are several well-known and popular DFT codes available for modeling materials. For this thesis, the Vienna-Ab-initio Simulation Package, otherwise known as VASP, is used for all studies [15–18]. VASP is arguably the most eminent and widely used DFT code for modeling both solid-state and molecular systems. This is due to its high computational efficiency in modeling all types of material systems and for the wide range of unique DFT techniques it offers to users.

VASP is built on the plane-wave pseudopotential methods, and so only the interacting valence electrons are included in each calculation. The interaction between the

ions and these valence electrons are described by the projector-augmented wave (PAW) method [19,20]. Near the ion core, quantum effects tend to cause the wavefunctions of these electrons to rapidly oscillate, meaning both the complexity and number of plane-waves needed to model these interactions becomes great. The PAW method essentially generalizes this interaction and smooths the wavefunctions near the core (which is out of ion-ion interaction distance). VASP also employs a smearing method in order to determine the occupancies of energy bands near the fermi level. This is akin to a adding a small finite temperature to the system, which pushes the electron orbital occupancy into the lowest energy ground state. This is done solely as computational minimization technique to avoid large changes in the charge density from one iteration to the next (*e.g.*, as a whole electron moves from orbital to another), which could disrupt the self-consistency cycle and prevent minimization.

Each chapter in this thesis, employs these general and standard DFT methods within the VASP framework. As the exact implementation varies between studies, a separate "computational methods" section is provided in each chapter, which describes the all DFT techniques and parameters necessary for someone to repeat the calculations.

# CHAPTER 3. POINT DEFECTS IN METALLIC THORIUM

In the early days of nuclear energy, it was originally thought that the industry would shift towards a thorium-based fuel cycle after the completion of the Manhattan project. This never happened, however, as the relative abundance and already established accessibility of uranium fuel would make it far too convenient of a fuel source to move on from [21]. As a result, interest in Th fuel diminished over time. Recently, however, there has been something of a renewed interest in thorium fuel as it is being considered for use in several of the new generation-IV advanced reactors currently under development. This includes high-temperature molten salt reactor designs [22,23], and the liquid metal-cooled fast breeder reactor (LMFBR) designs [24]. Th is also being considered for use in other design such as fast breeder reactors (FBR) [25] and in the accelerator driven subcritical reactor (ADSR) [26] design being developed in Europe. Th-U, Th-Pu, and Th-U-Pu alloy fuels were also created and tested in the EBR-II breeder reactor at Argonne National Laboratory [27].

Thorium metal exhibits two primary phases under normal pressure conditions. The α phase of Th has a face-centered cubic structure ($Fm\bar{3}m$ space group, A1 Struckturbericht designation) with four atoms in its primitive unit cell. The α phase is the groundstate phase and is stable up to $1350 \pm 10^{\circ}C$ [28], meaning it would likely be the dominant phase during most reactor operating conditions. The high temperature β-phase of Th has a body-centered cubic structure ($Im\bar{3}m$ space group, A2 Struckturbericht designation) with 2 atoms in its unit cell. Despite the high temperatures needed for its formation, understanding of the structure and behavior of β-Th is necessary because in rare off-normal situations it could

potentially form in reactor environments. In transient events, phase transformations in fuel materials, such as α→β could in the undesirable redistribution of fissionable atoms or in potentially disastrous phenomena such as fuel cladding cracking or rupture. When alloyed with small amounts of niobium or zirconium, both commonly used materials in the nuclear industry, the $\alpha \rightarrow \beta$ transition temperature is lowered [29], meaning that the physical and structural properties of the β-Th phase need to be well understood during the design process of any new reactor.

### *3.1.1 Point Defects*

The term "lattice defects" refers to the defects present the atomic lattice structure of a crystalline material. When the adjectival "point" is prefixed, (*i.e.,* point defect) this means one is specifically referring to a crystal defect involving only one atom or lattice site. Most commonly, these are vacancies in the atomic lattice, in which an atom is missing from one lattice site, or interstitial atoms in the lattice, in which an extra atom has found its way into the atomic lattice and rests inside one of the interstitial regions between occupied lattice sites. Many important material properties, ranging from strength and ductility to electrical conductivity, are directly dependent on the type and concentrations of points defects present in its crystalline lattice.

In a reactor core environment, the number of point defects present in both fuel and structural components is significantly elevated by the high levels of irradiation [30]. While the high temperatures in the core generally tend to promote defect annihilation at sinks (*i.e.,* grain boundaries and other interfaces), the rate of annihilation and thus overall defect concentration will ultimately be dependent on things like sink density, defect stability and

the local lattice strains around a defect. Additionally, to annihilate at a sink a defect must first thermally migrate through the surrounding lattice. Since this process of formation, migration and annihilation is constantly occurring under irradiation, the defect balance can be thought of in terms of a defect flux that permeates through the structure [31]. High defect fluxes can induce undesirable changes in the physical dimensions of a material and in its mechanical properties. Therefore, when designing materials for use as fuels or structural components in a nuclear reactor core it is critical to understand the fundamental behavior of its point and lattice defects.

There are currently several established methods for experimentally measuring properties of point defects in metals. Methods for determining point defect formation energies, for example, generally involve altering some kind of system parameter, like temperature, and then measuring the change in some property or variable that can be mathematically correlated to defect concentrations. Once the concentration of some type of defect is known at some temperature, the formation energy of the defect can be calculated [32]. Conversely, if the defect formation energy is known, the concentration at any temperature can be predicted.

A few of the most popular and successful measurement methods include (i) positron annihilation spectroscopy (PAS) in which positrons become trapped in lattice vacancy sites and the measurement of gamma rays that form during the subsequent annihilation events can be used to estimate vacancy concentration [33,34]; (ii) the differential thermal expansion method in which the small changes in volume due to the ‘outward’ movement of atoms during vacancy formation can be precisely measured, separately from the thermal expansion of the lattice, and used to estimate vacancy and interstitial concentrations

[35,36]; (iii) electrical resistivity measurements in which the change in resistivity with temperature due to defects can be decoupled from the change due to lattice vibrations allowing for the calculation of defect concentrations [37]; and (iv) low energy electron microscopy in which bulk defect concentrations are estimated from defect annihilation rates visually able to be measured at step edge dislocations along the surface of a metal [38].

While all of the above-mentioned methods have successfully been used to measure defect formation energies they are not without their difficulties. The combination of the often ultra-precise measurements, high temperatures, and control over other contributing variables to properties like thermal expansion and resistivity mean these measurements often become intractably difficult for complex and sensitive systems. When considering the radiation effects inherent to many nuclear fuel materials it's clear that accurately performing measurements of this nature should prove to be an extremely difficult task. Additionally, for some of these methods, like PAS, which may actually be benefited by a radiation environment, only the formation energy of a vacancy defect can be obtained and for other methods it can be difficult to separate contributions of individual defect types from the overall defect concentration.

### *3.1.2 Ab-Initio Modelling of Point Defects*

Density functional theory offers an alternative method to study point defects. Ab-Initio calculations of systems containing point defects have been successfully demonstrated and shown to produce accurate and reliable results [39,40]. While electronic structure calculations of actinides can be difficult due to complex electronic groundstate and self-

interaction errors associated with the presence of itinerant 5f electrons [41], when proper care and attention is paid to the choice of exchange-correlation functionals, supercell structures, and the handling of strongly correlated systems and relativistic effects accurate DFT simulations of the early actinides are more than possible [42–48]

Ab-Initio simulations involving Th are particularly less complex than those involving the other actinides as most of this complexity stems from the difficulties associated with modelling electrons in the 5f valence band, whereas Th does not possess any true 5f electrons. Th's empty 5f valence initially led to the belief that it should behave more similarly to the tetravalent d transition metals of group IV (*e.g.,* Ti, Zr and Hf) and prompted confusion over why Th would prefer a face-centered cubic (fcc) groundstate structure over the hcp structure exhibited by those other transition metals. It wasn't until Rao *et al*. [49] modelled Th using a linear muffin-tin orbital (LMTO) technique that true understanding of the groundstate behavior and the role of the 5f band in Th began to form. They initially found that under high pressures the 5f band of thorium widens and becomes occupied by one electron driving a phase transition from the fcc to the bct structure. Shortly after, Johansson *et al*. [50] showed that it was the presence of itinerant (*i.e.,* traveling from place to place) electrons in the 5f valence band, although small, that stabilized Th's fcc groundstate structure and proved that its electronic behavior was, in fact, more similar to that of the early actinides (Pa-Pu) than the tetravalent transition metals.

In addition to the two studies already mentioned, there have only been a handful of other ab-initio investigations into Th's groundstate properties. Of these most have only cursorily examined the electronic behavior of Th as part of a larger focus on the properties of the entire light actinide series (Ac-Np and sometimes Pu) [41,46,51–55]. These studies

have almost exclusively focused on Th's groundstate fcc and pressure induced bct allotropes, neglecting the bcc structure formed at high temperatures. Only Johansson *et al*. [50] has used DFT to model the bcc structure while studying phase stability under pressure.

There have been only two theoretical studies to investigate point defects in thorium metal. Daroca *et al.* [56], using a norm-conserving Troullier–Martins pseudopotential [57], calculated the vacancy, di-vacancy, and tetrahedral interstitial formation energies in fcc thorium in addition to He, Xe, and Kr impurity defects. Before that, Nazarov *et al*. [58] using a standard projector augmented wave (PAW) pseudopotential DFT method, calculated the vacancy formation energy in twelve fcc metals, including Th, and compared the accuracy of four popular approximations of the exchange-correlation functional. It was found that the differences between the calculated formation energies for each functional could be attributed to the way each handled electron exchange and correlation across the internal surface formed by the vacancy. The authors then developed and applied a modified version of a correction scheme, previously developed by Mattsson *et al*., [59] to account for the discrepancies between functionals and were able to produce consistently accurate vacancy formation energies among all functionals for each of the twelve metals studied.

The choice of exchange-correlation functional can significantly affect the accuracy of DFT defect calculations. The results of Nazarov *et al*. showed that it was not uncommon for different functionals to produce significantly different results for the same property. Lattice constants often differed by more than 0.1 Å and bulk moduli by more 20-30 GPa. Vacancy formation energies could differ by more than 0.2-0.4 eV, which could be as much as a 30-50% difference in some cases. The correction scheme was able to account for the differences, but it was developed specifically to handle the internal surface of a vacancy.

The internal surface that could be associated with an interstitial defect is invariably more complex and would show an increase in the electron density rather than a than the decrease seen with a vacancy.

A functionals ability to properly handle exchange and correlation across the complex bonding surrounding an interstitial in addition to its ability to predict simpler properties like lattice constants and bulk moduli will directly affect the accuracy of any calculated formation energies. Therefore, when attempting to calculate these types of complex properties, particularly those for which very little experimental data exists, it is vital to test the performance of multiple functionals in the prediction of other known properties that would have a direct impact on the unknown property of interest. An exchange-correlation functional's ability to consistently reproduce real properties should instill a high degree of confidence in the calculated properties of other related but experimentally unknown properties.

### *3.1.3 Point Defect Formation Energies in Th Metal*

In this work, both the groundstate fcc and high-temperature bcc phases of Th are modelled using DFT. First, the basic atomic structures of each phase are modelled to calculate lattice constants, elastic constants, elastic moduli, and Debye temperatures. These properties are then benchmarked against existing experimental and computational data to assess performance of exchange-correlation functionals in modelling the Th system. Formation energies are then calculated for self-defects (*i.e.,* point defects involving only Th) in the pure fcc and bcc Th phases and then for impurity defects (*i.e.,* a U atom) in the groundstate fcc Th phase.

In order to evaluate exchange functional performance in modelling Th properties all calculations are performed using three different GGA (generalized gradient approximation) functionals: (i) the PBE-GGA developed by Perdew, Burke and Ernzerhof [11]; (ii) the RPBE-GGA (*Revised* PBE) developed by Hammer *et al*. [60]; and (iii) the AM05-GGA developed by Armiento and Mattsson [61]. The PBE, one of most commonly used functionals for modelling solid metallic systems, was used by both Daroca *et al*. [56] and Nazarov *et al.* [58], and while generally considered the most universal functional for modelling most properties of metals it does not always perform as well as some of the newer functionals. In this work we use the PBE to benchmark our calculations against those by Nazarov et al.. In addition to the PBE, the other functionals used this work, the RPBE and AM05, which were both originally developed to improve chemisorption energies in surface simulations, have shown success in modelling both basic system properties like lattice and elastic constants [62–64] while also producing accurate defect properties [59,61,65].

## 3.2 Computational Methods

### *3.2.1 DFT Parameters*

All calculations are performed using the Vienna Ab initio Simulation Package (VASP), which utilizes a plane wave basis set together with the projector augmented wave (PAW) method to calculate the Kohn-Sham electronic groundstate of a many-body system [15–18]. A standard (scalar-relativistic) Th PAW potential with $6s^2 6p^6 5f^0 6d^2 7s^2$ valence electrons with a [Xe, 5d, 4f] core and a standard U PAW potential with $6s^2 6p^6 5f^3 6d^1 7s^2$ valence electrons with a [Xe, 5d, 4f] core are used for the U impurity defect calculations

[19,20]. A plane wave basis cut-off energy of 500 eV was used for both Th and U atoms. The method of Methfessel-Paxton of the 1st order [66] is used to determine electron partial occupancies with a smearing width of 0.2 eV. As mentioned in the previous section, all three functionals, (the PBE, the RPBE, and the Am05) are used for all calculations. Additionally, calculations on the perfect unit cells showed that spin-polarization has a negligible effect on the total energy for both phases.

### *3.2.2 Calculation of Structural and Elastic Properties*

Structural relaxations were first performed for the primitive fcc and bcc unit cells, employing periodic boundary conditions and allowing for the full relaxation of cell volume, cell shape, and atomic positions. Electronic and ionic convergence criterion of 1.0e-6 eV and 1.0e-5 eV, respectfully, were used regarding the total energy of the system. K-point grids of 14 x 14 x 14 and 21 x 21 x 21 were used to converge the total energy to below 1 meV for the 4 atom fcc and 2 atom bcc primitive unit cells, respectively.

Once structural relaxations were complete, and lattice constants were found for each phase, finite lattice distortions were applied to each relaxed unit cell allowing for the calculation of the elastic tensor and the elastic constants based on the stress-strain relationships[67]. The elastic tensor was found for both rigid ions and for internally relaxed ions, where the ionic contribution is determined by inverting the ionic Hessian matrix and multiplying with the internal strain tensor. The Voigt-Reuss-Hill approximation [68], in which the polycrystalline elastic moduli are found by taking the average of the bounds set by Voight [69] and Reuss [70], was used to calculate the bulk modulus (B), shear modulus

(G), Young's modulus (E), Poisson's ratio (σ), and Debye temperature ($\theta_D$) [71] for cubic lattices according to the following equations:

$$B = \frac{1}{3}(c_{11} + c_{12}) \tag{23}$$

$$G = \frac{1}{2}\left(\frac{c_{11} - c_{12} + 3c_{44}}{5} + \frac{5c_{44}(c_{11} - c_{12})}{4c_{44} + 3(c_{11} - c_{12})}\right) \tag{24}$$

$$E = \frac{9GB}{G + 3B} \tag{25}$$

$$\sigma = \frac{3B - E}{6B} \tag{26}$$

and

$$\theta_D = \frac{h}{k_B}\left(\frac{3}{4\pi V_a}\right)^{1/3} v_m \tag{27}$$

Where $h$, $k_B$ and $V_a$ are Planck's constant, Boltzmann's constant and the average atomic volume, respectively. The average sound of speed, $v_m$, is found from the following equation:

$$v_m = \left[\frac{1}{3}\left(\frac{2}{{v_t}^3} + \frac{1}{{v_l}^3}\right)\right]^{-1/3} \tag{28}$$

Where $v_t$ and $v_l$ are the transverse and longitudinal sound velocities in an isotropic material and can be calculated using Navier's equation using the density, $\rho$, with the shear and bulk moduli [72]:

$$v_l = \left(\frac{3B + 4G}{3\rho}\right)^{1/2} \tag{29}$$

$$v_t = \left(\frac{G}{\rho}\right)^{1/2} \tag{30}$$

### *3.2.3 Calculation of Defect Formation Energies*

Single unit cells are, by themselves, not large enough to calculate defect formation energies. Instead large supercells, containing many multiples of these primitive unit cells in each direction are needed to prevent the defect from interacting with itself through the periodic boundaries at the edge of the simulation box. The procedure for calculating a defect formation energy using DFT involves finding the energy difference between the defect containing supercell and the energy of an equivalently sized supercell without the defect, (*i.e.*, an ideal or perfect crystal structure of the same size). For the fcc structures, a 3 x 3 x 3 supercell containing 108 atoms was used in the defect calculation. For the bcc structures, a 4 x 4 x 4 supercell containing 128 atoms was used. K-point grids of 6 x 6 x 6 and 3 x 3 x 3 were used to model each of these fcc and bcc supercells, respectively. For pure Th, defect formation energies are calculated for both fcc and bcc phases. For Th-U, however, in which only one U atom is included (*i.e.*, the defect), defects are only modeled in the more stable groundstate fcc phase.

There are several types of point defects that can exist in a crystal lattice. The most common of these is the vacancy defect, in which an atom is missing from a lattice site, leaving a hole in the lattice. Interstitial defects are also fairly common and are readily produced in highly radioactive environments. There are several types of interstitial defects,

which are named according the polyhedral shape formed by the nearest neighbor shell of atoms around the defect, or by the specific structure formed by the defect. The interstitials modelled in this study are the octahedral, tetrahedral, <100> dumbbell, <110> dumbbell, and <111> dumbbell defects. The last defect modelled in this work is the substitutional defect. In this defect, an impurity or solute type atom takes the place of a host atom in an ordered lattice. Each of these defect structures are shown in **Figure 3.1**. Each of these defects was modelled in both Th phases, including both pure Th and Th-U supercells (Th-U defects are only modelled in the fcc phase). Vacancy defects were only modelled for the pure Th phases, however, while the substitutional impurity type defect was only modelled for the Th-U supercell.

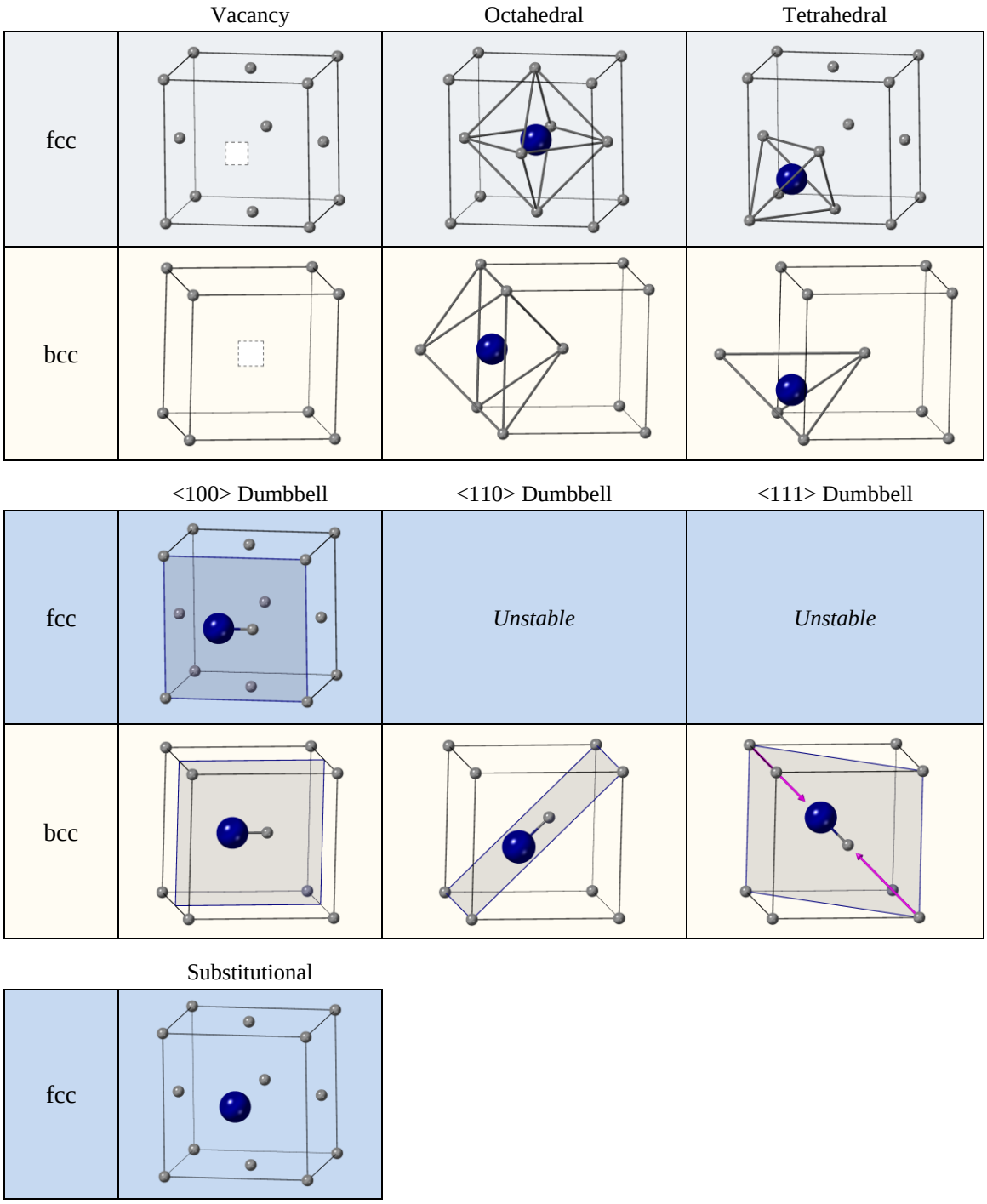


**Figure 3.1.** Point defect structures in the fcc and bcc lattices. The white squares indicate a vacant lattice site, the large blue atom represents the defect atom site, and the small grey atoms represent normal host atoms.

In these calculations, only isolated defects are considered and the energy of an isolated atom at ground state is assumed to be zero, letting us define the vacancy formation energy as:

$$E_{vac}^{f} = E_{(n-1)Th} - \frac{n-1}{n} E_{nTh} \tag{31}$$

Where $E_{(n-1)Th}$ is the total energy of an $(n-1)$ Th atom supercell containing one vacancy and $E_{nTh}$ is the total energy of the ideal Th supercell containing $n$ lattice sites fully occupied by Th atoms. Using the same relationship between total energies, the formation energy of a Th self-interstitial is then:

$$E_{int,Th}^{f} = E_{(n+1)Th} - \frac{n+1}{n} E_{nTh} \tag{32}$$

Where $E_{(n+1)Th}$ is the total energy of a supercell containing one Th interstitial. To calculate formation energies of U defects in the Th supercell an additional term accounting for the total energy of single U atom in its groundstate orthorhombic α phase, $E_U$, is included. This gives the formation energy of a substitutional U atom as:

$$E_{sub,U}^{f} = E_{(n-1)Th+U} - \frac{n-1}{n} E_{Th} - E_U \tag{33}$$

Where $E_{(n-1)Th+U}$ is the total energy of an $(n-1)$ Th supercell containing one substitutional U atom occupying the regular lattice site of a Th atom. Lastly, the U interstitial formation energy is:

$$E_{int,U}^{f} = E_{nTh+U} - E_{nTh} - E_{U} \quad (34)$$

Where $E_{nTh+U}$ is the energy of the $n$ Th atom supercell containing one U atom in an interstitial position.

As an additional note, since the high temperature bcc phase is mechanically unstable at the DFT simulation temperature of 0 K, it is not possible to perform a full-relaxation of all atoms in defect containing supercells. Therefore, to model defects in the bcc supercells, a nearest-neighbor (NN) relaxation scheme is employed, in which geometric relaxation is allowed only for a shell of atoms around the defect site containing all of the first, second and sometimes third nearest neighbors, depending on the specific defect. All other atoms in the supercell are constrained to their initially defect-free relaxed positions, while every atom is allowed to participate in the electronic relaxation.

## 3.3 Results and Discussion

### *3.3.1 FCC Structural and Elastic Properties*

The calculated lattice constants and elastic properties for the fcc α-Th phase are presented and compared with experimental values and with previous calculated values in Table 3.1. The experimental lattice constant of the α-Th phase was found by Chiotti [73] using X-ray diffraction at room temperature. The calculated lattice constants presented here were found at 0 K, and so a small correction can be added to each constant to account for thermal expansion at room temperature. Based on expansion coefficients supplied by Gschneidner et al. [74], this correction amounts an $\sim 0.015$ Å addition at room temperature (This addition is not included in the reported table values). Even with this room-

temperature correction, every functional except the RPBE under-predicted the experimental lattice constant. The PBE functional produced the most accurate lattice constant of the three functionals used in this work, even outperforming the full-potential linear muffin-tin orbital (FP-LMTO) model employed by Soderlind et al.[41,51].

**Table 3.1.** Fcc lattice constants ($a_0$), elastic constants ($\boldsymbol{c_{ij}}$), and elastic *moduli (B, G, C, C'Zen, E)* and the Poisson's ratio ($\boldsymbol{\sigma}$), calculated using the PBE, RPBE, and AM05 functionals. Previous PBE values and FPLMTO values from a full-electron method are also listed.

FCC Structural and Elastic Data

| Functional | $a_0$ (Å) | $c_{11}$ (GPa) | $c_{12}$ (GPa) | $c_{44}$ (GPa) | $B$ (GPa) | $G$ (GPa) | $C'_{Zen}$ (GPa) | $E$ (GPa) | $\sigma$ |
|---|---|---|---|---|---|---|---|---|---|
| *Expt.* | 5.089[1] | 78.0 [2] | 45.9 [2] | 51.3 [2] | 58.0 [2] | 40.6 [3] | 14.9 [3] | 103.1 [3] | 0.268 [3] |
| PBE | 5.053 | 83.5 | 41.7 | 54.6 | 55.6 | 37.2 | 20.9 | 91.2 | 0.227 |
| | 5.03[4] | 84.0 [4] | 39.8 [4] | 57.6 [4] | 54.5 [4] | 39.2 [4] | 22.1 [4] | 94.9 [4] | 0.210 [4] |
| | 5.045[5] | | | | | | | | |
| | 5.044[6] | | | | | | | | |
| RPBE | 5.091 | 81.2 | 36.4 | 54.0 | 51.3 | 37.9 | 22.4 | 91.3 | 0.204 |
| AM05 | 4.955 | 89.5 | 43.3 | 65.6 | 58.7 | 43.2 | 23.1 | 104.1 | 0.205 |
| FP-LMTO | 4.91 [6] | 53.3 [7] | 35.3 [7] | 45.9 [7] | 42.1 [7] | 24.3 [7] | 10.0 [7] | 60.9 [7] | 0.254 [7] |

[1] Chiotti [73]
[2] Armstrong et al. [75]
[3] Frye [76]
[4] Bouchet et al. [54]
[5] Daroca et al. [56]
[6] Nazarov et al. [58]
[7] Soderlind;et al. [41,51]

The three independent elastic constants for a cubic crystal, $c_{11}$, $c_{12}$, and $c_{44}$, are also reported in Table 3.1 along with experimental elastic constants found by Armstrong et al. [75] and experimental elastic moduli found by Frye et al. [76]. The experimental elastic constants were measured at 300 K for a pure Th sample using resonance and pulse-echo techniques. In this method, the elapsed time is measured between applied high-frequency pulses and their associated echoes. The elapsed times yield sound wave

propagation velocities which in turn yield elastic constant properties. The author used their measured constants to calculate Voight and Ruess moduli which were found to be in relatively good agreement with experimentally measured moduli. The experimental moduli were similarly measured at room temperature and were found through tensile and compression tests. The measured stress and strain curves directly yielded Young's modulus of elasticity and Poisson's ratio, which together allowed for the calculation of the Shear modulus.

The PBE and RPBE produce roughly similar values that were close to the experimental values, while AM05 over-predicted the experimental constants and the FP-LMTO underpredicted. The PBE showed the lowest average deviation from experimental constant (5.1 GPa), with the RPBE very close behind (5.8 GPa), and the AM05 (10.2 GPa) and FP-LMTO (14.3 GPa) coming in fairly far behind. Somewhat interestingly, however, it's the elastic constants of AM05 functional that actually produced the most accurate elastic moduli, (*i.e.*, bulk ($B$), shear ($G,\ C'_{Zen}$), and Young's ($E$) Moduli). The FP-LMTO method, on the other hand, produced the most accurate Poisson's ratio.

Calculated Debye temperatures and the related speeds of sound (*e.g.*, longitudinal, transverse, and average) are reported for the α-Th phase in Table 3.2. The all-electron FP-LMTO method was more accurate then each of the pseudopotential DFT methods in predicting the Debye temperature. Each of the functionals performed fairly similarly to one another, over-predicting this temperature by approximately the same amount. To find the 0 K experimental value, Anderson et al.[72], used inelastic neutron scattering to probe the phonon spectrum of thorium, and extrapolated the 0 K Debye temperature from room temperature data using the experimental elastic constants of Armstrong et al. [75]. The

density is also reported here for completeness; however, the density is just an extrapolation of the calculated lattice constant and so the behavior is identical.

**Table 3.2.** Calculated density ($\boldsymbol{\rho}$), longitudinal sound speed, transverse sound speed, average sound speed ($\boldsymbol{v_m}$), and Debye temperature ($\boldsymbol{\theta_D}$) for the fcc α-Th phase. Reported values correspond to those using the PBE, RPBE, and AM05 functionals, in addition to PBE and FP-LMTO values from literature**.**

| Functional | $\boldsymbol{\rho}$ $(\boldsymbol{g\ cm^{-3}})$ | $\boldsymbol{v_l}$ $(\boldsymbol{m\ s^{-1}})$ | $\boldsymbol{v_t}$ $(\boldsymbol{m\ s^{-1}})$ | $\boldsymbol{v_m}$ $(\boldsymbol{m\ s^{-1}})$ | $\boldsymbol{\theta_D}$ $(\boldsymbol{K})$ |
|---|---|---|---|---|---|
| PBE | 11.95 | 2967.41 | 1763.75 | 1952.90 | 182.65 |
| | 12.11 [1] | 2970.22 [1] | 1799.88 [1] | 1989.15 [1] | 186.90 [1] |
| RPBE | 11.68 | 2953.30 | 1801.58 | 1989.70 | 184.71 |
| AM05 | 12.67 | 3029.71 | 1846.46 | 2039.46 | 194.53 |
| FP-LMTO | 13.02 [2] | 2378.32 [2] | 1365.08 [2] | 1516.26 [2] | 145.95 [2] |
| *Expt.* | 11.787 [3] | | | | 158 [3] |

[1] Bouchet et al. [55]
[2] Soderlind; et al. [77]
[3] Anderson et al.[72]

### *3.3.2 BCC Structural and Elastic Properties*

Lattice constants of the bcc β-Th phase are reported in Table 3.3. The experimental β-Th lattice constant was also found through X-ray diffraction by Chiotti [73]. The measurements were taken at 1450 ºC using a specialized XRD apparatus, in which the Th specimen was heated by heat radiating from a nearby tantalum filament. Temperature measurement and control was maintained using an optical pyrometer.

We can see a similar trend in the functional performance here with the PBE coming closest to the experimental value and the AM05 somewhat severely (relatively) under-predicting the lattice constant. The β-Th phase is a high-temperature phase, however, and so thermal expansion is expected to be significant in the reported experimental value,

which was found at 1450 ˚C [29]. Unfortunately, accurate thermal expansion coefficients were not available for this phase so an expansion corrected lattice constant cannot be found.

**Table 3.3.** Bcc lattice constants ($a_0$), elastic constants ($\boldsymbol{c_{ij}}$), and elastic moduli *(B, G, C, C'$_{Zen}$, E)* and the Poisson's ratio ($\boldsymbol{\sigma}$), calculated using the PBE, RPBE, and AM05 functionals.

BCC Structural and Elastic Data

| Functional | $a_0$ (Å) | $\boldsymbol{c_{11}}$ | $\boldsymbol{c_{12}}$ | $\boldsymbol{c_{44}}$ | $\boldsymbol{B}$ | $\boldsymbol{G}$ | $\boldsymbol{C'_{Zen}}$ | $\boldsymbol{E}$ | $\boldsymbol{\sigma}$ |
|---|---|---|---|---|---|---|---|---|---|
| *Expt.* | 4.11 [1] | | | | | | | | |
| PBE | 4.019 | 34.88 | 71.22 | 38.62 | 59.1 | -61.2 | -18.2 | -280.2 | 1.29 |
| RPBE | 4.049 | 32.7 | 66.2 | 36.6 | 55.0 | -51.0 | -16.8 | -223.5 | 1.18 |
| AM05 | 3.952 | 36.6 | 76.5 | 45.2 | 59.1 | -55.61 | -20.0 | -236.08 | 1.12 |

[1] Chiotti [73]

Evaluating the β-Th phase elastic constants is a bit more challenging in relation to those of the α-Th phase. For one, no experimental data on the bcc Th elastic constants exists, so there is no direct way gauge the accuracy of the three elastic constants. We can use the physical meaning of the elastic moduli, however, and the Born stability criteria of a cubic crystal [78] to understand what the calculated results suggest about the bcc phase. For instance, the negative values obtained for the shear and Young's moduli suggest mechanical instability in this phase at 0 K. This is furthered by the fact that only two of the Born criteria (1) $c_{11} + 2c_{12} > 0$ and (2) $c_{44} > 0$ are satisfied, while the third (3) $c_{11} - c_{12} > 0$ is not. One can also calculate the extreme shear moduli $C'$ identified by Zener [79] as $(c_{11} - c_{22})/2$, finding in this case a negative value for both PBE and RPBE constants suggesting an instability towards a tetragonal distortion of the lattice.

The large difference between the two shear constants $C'$ and $C''$ (ie. $c_{44}$) suggests a large degree of anisotropy within the crystal (at 0 K) in relation to the directionality of shear distortions.

### *3.3.3 Defect Formation Energies*

#### 3.3.3.1 Pure Th Defects

Calculated defect formation energies for both the pure fcc α- and bcc β-Th phases reported in Table 3.4. These energies are also shown in **Figure 3.2**. The vacancy formation energies in the fcc phase found by each exchange-correlation (XC)-functionals are nearly identical and matched well with other theoretical works. Amazingly, each functional produced the same trends regarding the energies of the relative defect types, with the only real differences being in the overall absolute energy of the defects. For both phases the AM05 defects had the highest energies, followed by the PBE and then the RPBE. Interestingly this inversely matched the size of the lattice constant predicted by each functional and so may be related.

Only one experimental defect formation energy was available from literature; the fcc vacancy formation energy, which was found by Kim et al. using the PAS method [80]. Unfortunately, there is a large deviation between the theoretical values of each functional and this experimental value. Daroca et al. [56] previously postulated, however, that this discrepancy is more likely to be due to the assumptions used by Kim et al. for fitting coefficients within the standard trapping model.

The calculated β-Th vacancy formation energy does not have an experimental value to compare to but is lower than the α-phase formation energy, which agrees with the prediction by Kim et al. that the vacancy formation energy in the bcc phase would be lower than in the fcc phase. The prediction was based on a similar trend observed in other metals exhibiting both fcc and bcc phases, such as in Fe alloys [81] and CuZn alloys [82] and on the fact that in vacancy formation, only four bonds are broken in the bcc structure relative to six in the fcc structure.

**Table 3.4.** Defect Formation Energies in fcc α- and bcc β-Th lattices. Listed values correspond to those calculated in this work using each functional and those from literature consisting of experimental values and previously calculated DFT values.

| | $E^f_{vac}$ | $E^f_{oct}$ | $E^f_{tet}$ | $E^f_{<100>}$ | $E^f_{<110>}$ | $E^f_{<111>}$ |
|---|---|---|---|---|---|---|
| FCC | | | | | | |
| Expt. | 1.28 ± 0.23 [1] | | | | | |
| PBE | 2.191<br>2.10 [2]<br><br>2.22 [3] (2.41 [3]*) | 4.627 | 5.237<br>5.45[2] | 4.878 | unstable | unstable |
| RPBE | 2.110[1] | 4.502[1] | 5.067[1] | 4.712[1] | unstable | unstable |
| AM05 | 2.358 | 4.868 | 5.550 | 5.139 | unstable | unstable |
| BCC | | | | | | |
| PBE | 1.382 | 4.068 | 4.278 | 3.950 | 3.216 | 4.112 |
| RPBE | 1.232 | 3.849 | 3.983 | 3.781 | 3.140 | 3.951 |
| AM05 | 1.575 | 4.178 | 4.347 | 4.030 | 3.252 | unstable |

[1] Kim et al. [80]
[2] Daroca;et al. [56]
[3] Nazarov et al. [58]
* Vacancy formation energy after correction was applied

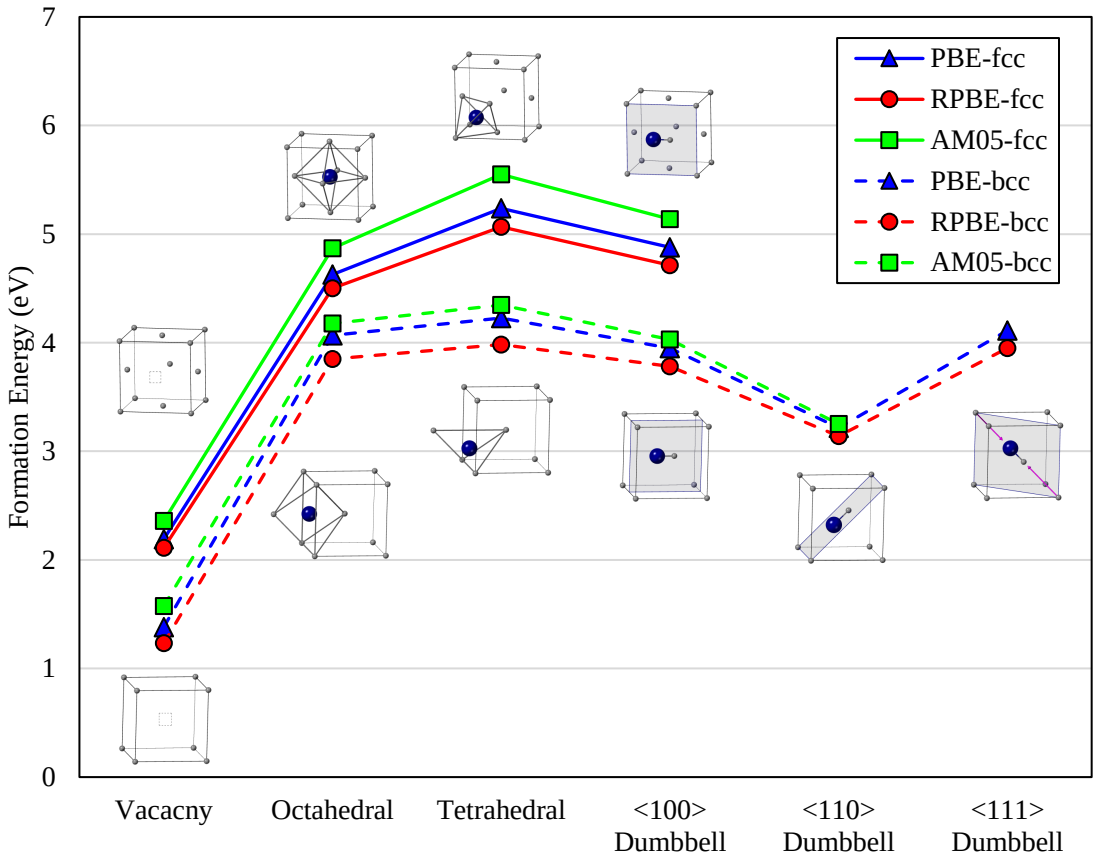


**Figure 3.2.** Defect Formation Energies in fcc α-Th (solid lines) and bcc β-Th (dashed lines) lattices. PBE values are shown in blue, RPBE values are shown in red, and AM05 values are shown in green.

There are no experimental interstitial formation energies for Th with which to compare with, but we can draw comparisons with trends observed in other fcc and bcc metals can be made**. Figure 3.3** shows the self-interstitial formation energies calculated in this work plotted alongside self-interstitial formation energies found for other fcc metals by several other authors who employed various theoretical methods. The energies shown in this figure have been normalized to the octahedral defect, set to 1 eV. From this we can

see that the that defect energies calculated in this work match the overall trend exhibited by fcc defect formation energies. In all cases, the vacancy formation energy is by the far the lowest in energy, and easiest for the lattice to accommodate, whereas the tetrahedral defect, being the most tightly bonded between its neighbors is the highest in energy. We can also see that the <110> and <111> defects, which were found to unstable in these simulations, are not unstable for all fcc materials.

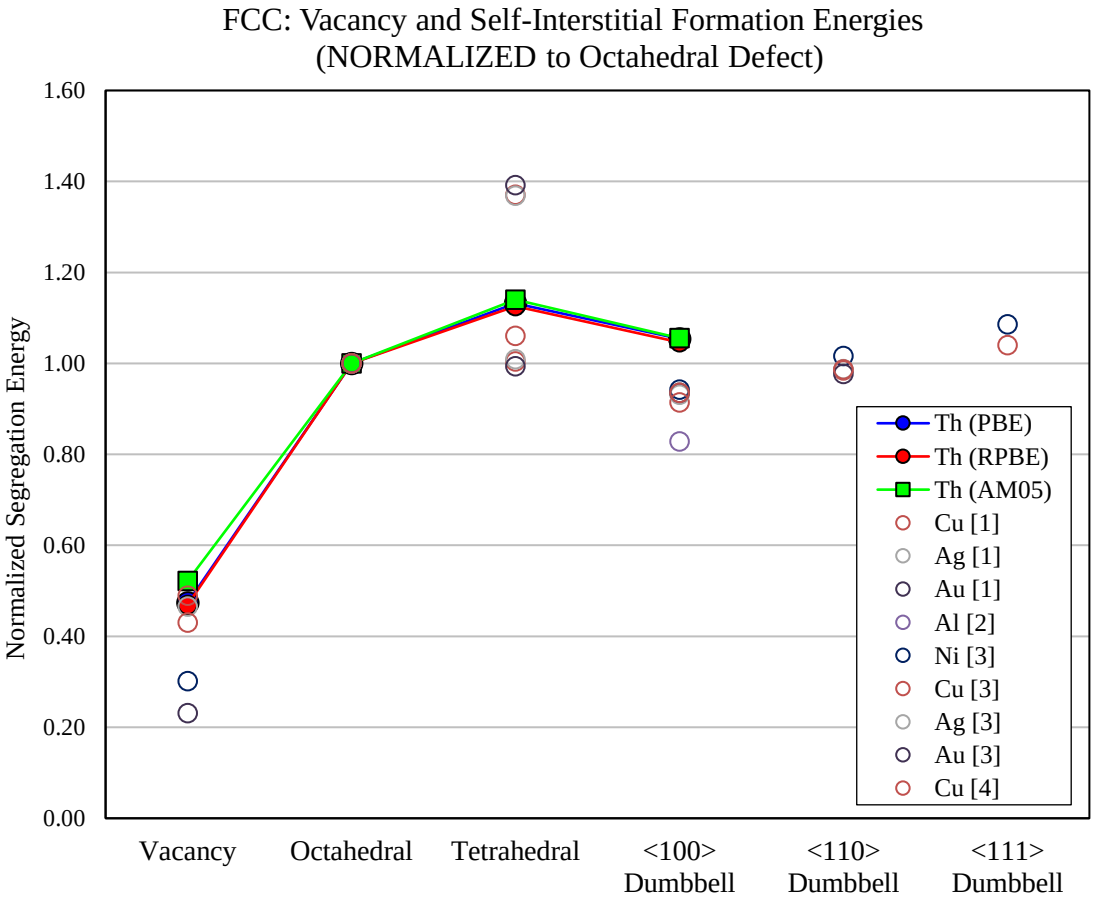


**Figure 3.3.** Aggregation of pure fcc metal defect formation energies. The lines correspond to the energies calculated for pure fcc α-Th in this work. Open circles denote values found in literature for various other pure fcc metals. All values were theoretically calculated. *References:* [1] Bandyopadhyay et al.[83]; [2] Klaver et al. [84]; [3] Lam et al. [85]; [4] Ingle et al. [86]

Perhaps the most important observation, in terms of this present study, is the relative consistency exhibited by the functionals. **Figure 3.3** shows us that the differences between each functional are very minor in relation to the overall spread of the defect formation energies. Really, the only noticeable difference is in the vacancy defect energy, for which the AM05 predicted a slightly higher energy than the PBE and RPBE. This difference is likely born out of the difference in the form of the functionals themselves and how surfaces (*i.e.,* low electron density regions) are treated by each. This will be discussed further in the section 3.3.4.

A similar comparison of bcc metal defect formation energies is shown in **Figure 3.4**. Defect formation energies for bcc metals are much more abundant in the literature, thus there are far more previously calculated values shown than for the fcc system. In **Figure 3.4**, these energies are now normalized to the <100> dumbbell defect, which was set to 1 eV. (The choice of which defect to normalize to in each system was made according to whichever defect was most consistently prevalent or available in each of the studies). In the bcc system we can see some similar trends to the fcc system, however, there is now more variability in the relative defect energies. The bcc structure is more loosely packed than the fcc structure, and so there is likely more ability for the lattice to accommodate an interstitial, hence the lower overall energies compared to fcc, but also the greater variability in each defect, like the tetrahedral defect, which was no longer the highest in energy on average. In the bcc structure, the tetrahedral defect is still generally more tightly packed than other defects, but not nearly as tightly packed as in the fcc structure.

Most importantly, however, we can see that the relative functional performance is fairly consistent. There is some slight deviation in the AM05 energies for the octahedral and tetrahedral defects, but it is not much. We also still see the slightly different values obtained between the AM05 and the other two functionals.

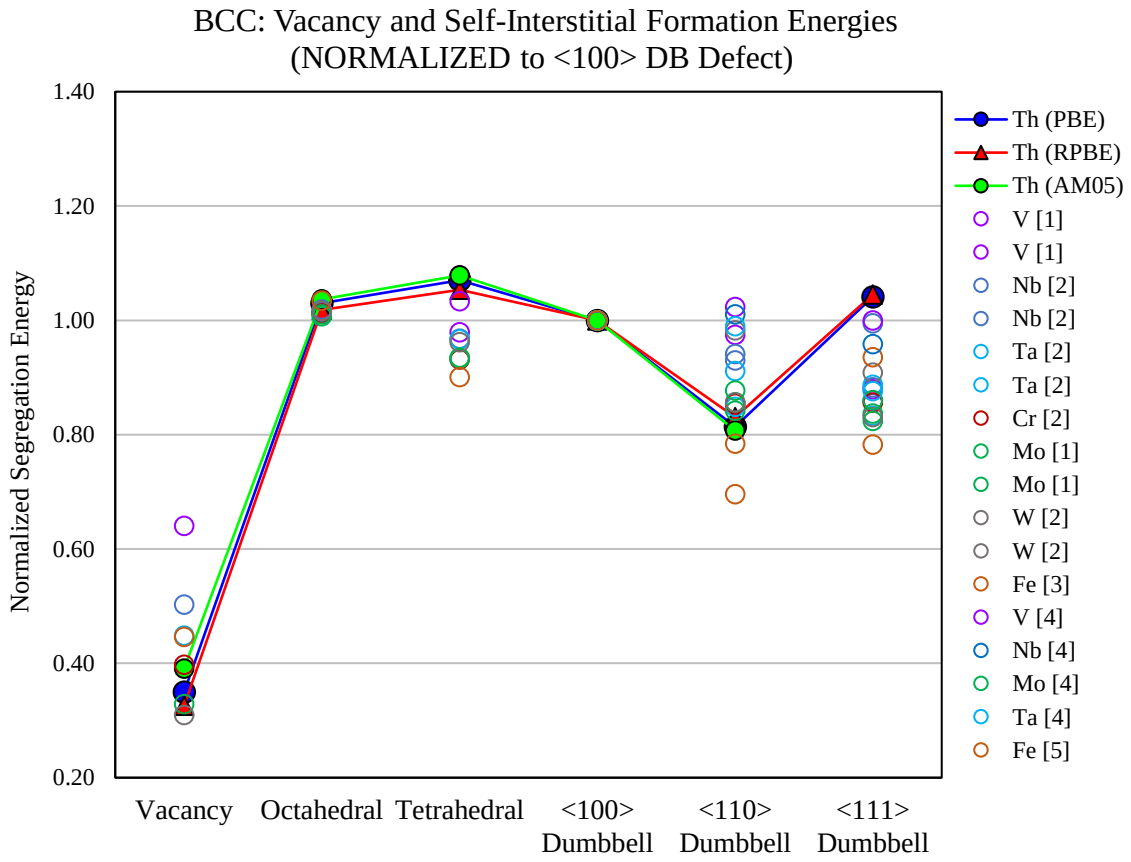


**Figure 3.4.** Aggregation of calculated pure bcc metal defect formation energies. The lines correspond to the energies calculated for pure bcc β-Th in this work. Open circles denote values found in literature for various other pure fcc metals. All values were theoretically calculated. *References:* [1] Han et al. [87], [2] Nguyen-Manh et al. [88], [3] Chu Chun et al. [89], [4] Finkenstadt et al. [90]

3.3.3.2 U Impurity Defects

U impurity defect formations energies in the fcc Th lattice are reported in Table 3.5 and shown in **Figure 3.5**. These U formation energies show a similar trend compared to the other Th-self defects, with the low strain inducing substitutional defect (replacing the vacancy defect) exhibiting the lowest energy and the very tightly bound tetrahedral defect requiring the highest energy to form. Interestingly, we also see a reversal in the overall magnitude ordering corresponding to the three functionals. The AM05 functional now produces the lowest energy, while the PBE functional produces the highest. This change is not immediately explainable, however, but it likely stems from each functionals ability to handle the complex bonding involving the newly added 5f electrons of the U atom. Additionally, the fact that the substitutional defect energies produced by each functional are very similar to another and do not show the same separation observed in the vacancy energies, further supports the notion that vacancy energy differences coming from each functionals performance across surface boundary regions.

**Table 3.5.** U defect formation energies in fcc α-Th. All listed values correspond to those calculated.

| | $E^f_{sub,U}$ | $E^f_{oct,U}$ | $E^f_{tet,U}$ | $E^f_{<100>,U}$ |
|---|---|---|---|---|
| PBE | 1.440 | 3.561 | 5.160 | 3.390 |
| RPBE | 1.478 | 3.631 | 5.364 | 3.440 |
| AM05 | 1.378 | 3.473 | 4.959 | 3.291 |

Again, there are no experimental formation energies in literature to compare with and unfortunately in this case, comparisons with other inclusion defects in fcc metals are made more difficult, relative to the self-interstitial defects, by the large variation of possible

atom sizes and defect position configurations in alloys. Daroca et al.[56], however, did calculate formation energies for He, Xe and Kr substitutional and tetrahedral defects in α-Th and found that as the size of the impurity atom increased (closer to the size of the Th atoms) the overall formation energies of the defects also increased. A similar aggregation of theoretically calculated defect formation energy data as the ones made in the previous section, but now for fcc impurity defects, is presented in **Figure 3.6**. From this we can see that the uranium defects follow a similar trend as the Th-self defects, with one exception being that the energy of the U octahedral defect in Th appears to sit at the low end of the range of the of octahedral defect energies.

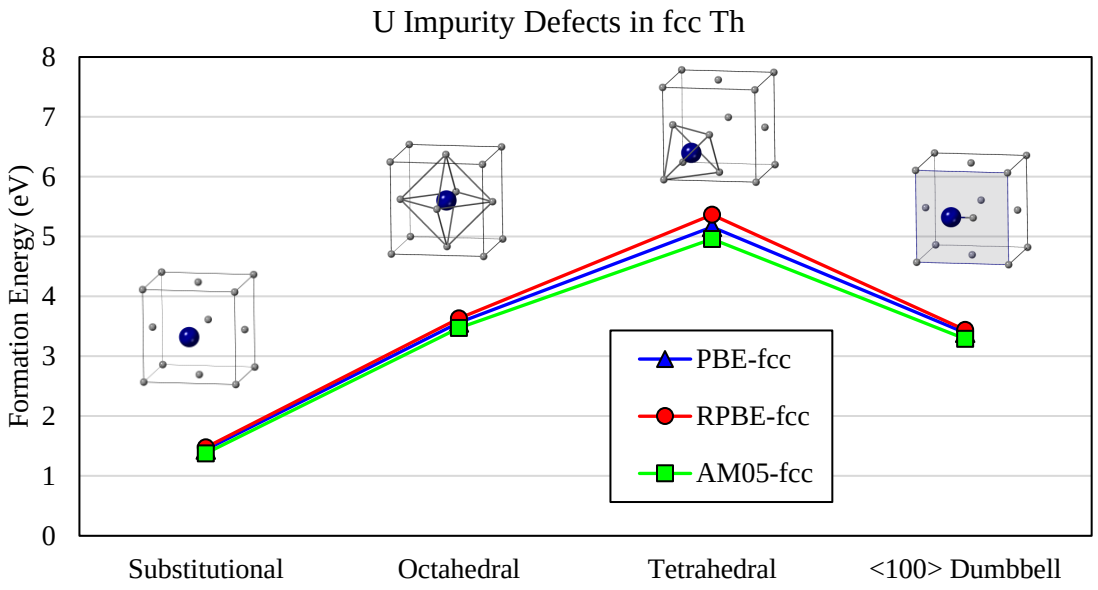


**Figure 3.5.** U impurity defect formation energies in fcc α-Th lattice. PBE values are shown in blue, RPBE values are shown in red, and AM05 values are shown in green.

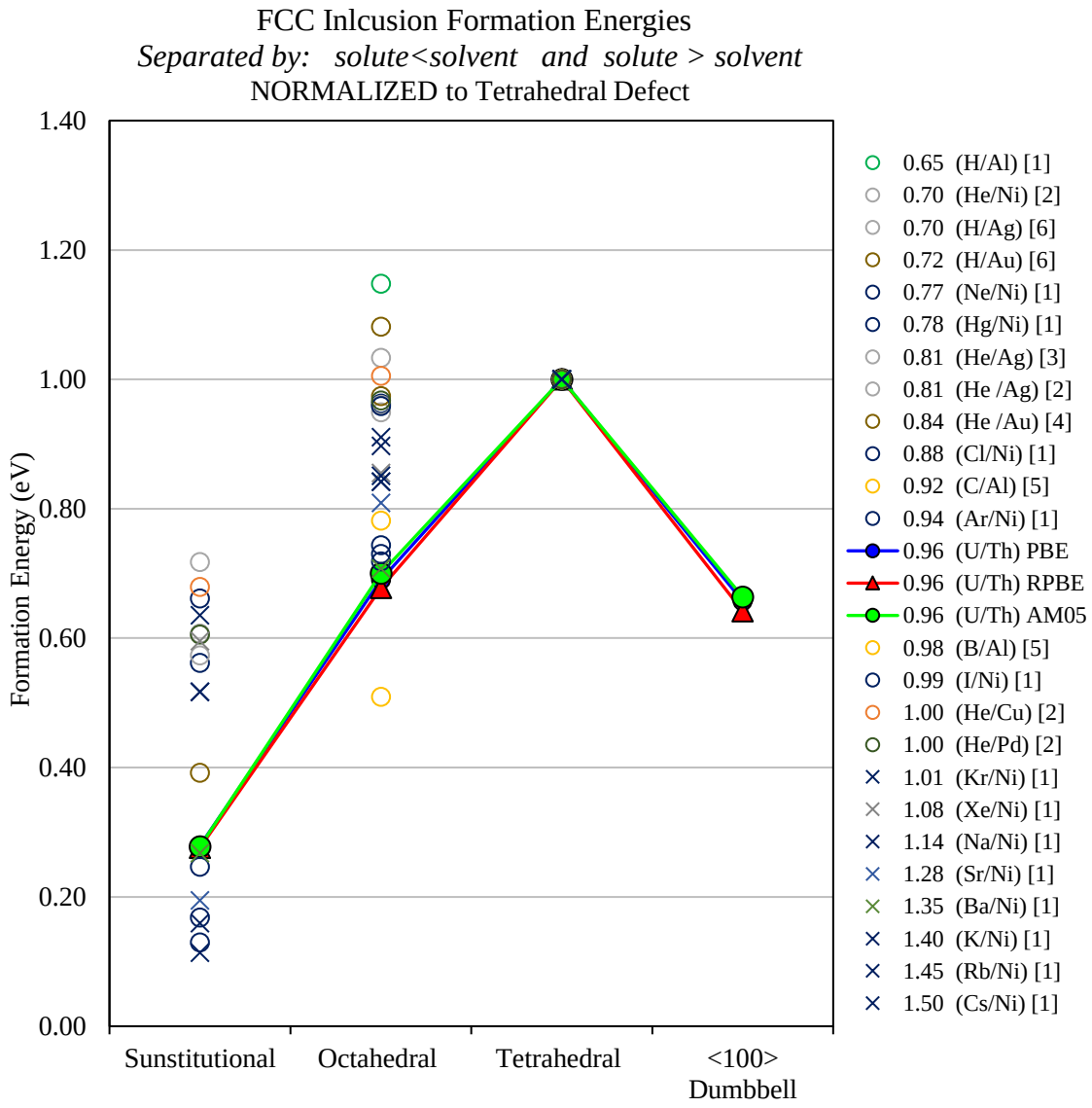


**Figure 3.6.** Aggregation of impurity defect formation energies in fcc metals. The lines correspond to the energies calculated for U defect containing fcc α-Th in this work. Open circles denote values found in literature for various other pure fcc metals. All values were theoretical calculated. *References:* [1] Connetable et al. [91]; [2] Zu et al. [92]; [3] Zhu et al. [93]; [4] Zhu et al. [94]; [5] David et al. [95]; [6] Han et al. [96]

### *3.3.4 Functional Performance*

While each of three functionals performed fairly well overall in the calculations in this work, it's difficult to gauge their true accuracy in the modeling of point defects because of the lack of experimental data. In place of this, several known structural and elastic properties which might have an influence on or be related to a lattice's ability to accommodate strain and tension around a defect were modelled first. In general, the PBE was most accurate among the three in modelling these basic properties, like the lattice constants and elastic constants. The RPBE was always right behind the PBE, however, while the AM05 showed a more varied range of accuracy, occasionally coming out on top (*e.g.*, some elastic moduli). The biggest observation that can be taken away from the defect calculations was the overall consistency shared between each functional. The defect energies found through each functional were offset by a small energy, but this appeared proportional to and likely related to the lattice constant spacing found by each functional. The only real consistent difference, which was itself still only minor, was in the AM05 prediction of the vacancy formation energies. This difference likely came from the differences in the form of each functional.

The PBE and RPBE functionals are actually very similar to one another, hence the reason for their similar performance. In fact, the RPBE is really just a "corrected" or "revised" version of the PBE, in the which the only difference between the two is the form of one term buried in the exchange side of the functional. This specific term is called the exchange enhancement factor, $F_x(s)$, and is a function of the reduced gradient density, $s$. In the original derivation of the PBE, this enhancement factor has the form

$$F_{xPBE}(s) = 1 + \kappa - \frac{\kappa}{(1 + \mu s^2/\kappa)} \tag{35}$$

Where $\kappa$ is a constant and is equal to 0.804 and the reduced gradient density, $s$, is proportional to electron density gradient as follows

$$s \propto \frac{|\nabla n|}{n^{4/3}} \tag{36}$$

This form has proven to be quite acceptable for the PBE, which itself has seen large success, producing countless accurate descriptions of materials and becoming one of the most widely used functionals in all of DFT since its development in the mid-90s. One area where the PBE has sometimes lacked, however, is in regions where a high electron density changes to a low electron density, like at a surface termination, or across the internal surface formed by a vacancy defect. In a letter, Zhang et al. showed however, that much of this deficiency could be improved by changing the value of the $\kappa$ from 0.804 to 1.245 [97]. They subsequently released a new functional named the revPBE, which was able to produce improved atomic total energies and molecular atomization energies in surface systems.

This change, however, caused the revPBE to locally violate something called the Lieb-Oxford bound, which provides a lower bound for the indirect part of the many-body Coulomb repulsion in an electronic system. In response to this violation, Hammer et al. [60] developed and published the RPBE functional, where instead of just changing the value of $\kappa$ (which in doing so meant that revPBE was no longer truly ab-initio) changed the form of the entire function itself to better mimic the revPBE in lower electron density

regions while still locally respecting the Lieb-Oxford bound. The form of this new exchange enhancement factor in the RPBE is

$$F_{xRPBE}(s) = 1 + \kappa\left(1 - e^{-\frac{\mu s^2}{\kappa}}\right) \tag{37}$$

We can directly show how each of these functions perform in regions of low electron density by plotting them for a hypothetical one-dimensional system populated an arbitrary electron density, loosing resembling the repeating atomic lattice. This is shown in **Figure 3.7**. As can be seen, the behavior of the two functionals most significantly deviate in the low electron density regions.

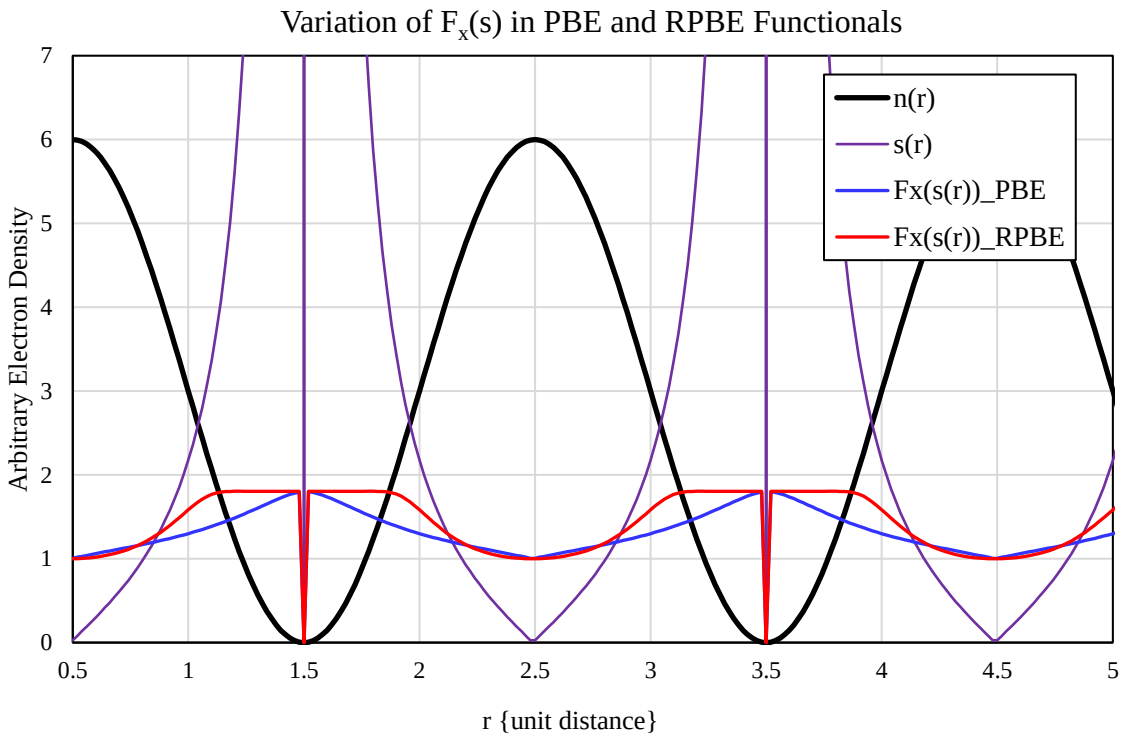


**Figure 3.7.** Variation in the exchange enhancement factors of the PBE and RPBE functionals. This shows a plot according to an arbitrary electron density (thick black line) which loosely resembles the repeating atoms in a lattice. The light purple line shows the reduced density gradient, which is proportional to the electron density according to equation (36). The exchange enhancement factors are plotted as a function of this reduced density gradient. The PBE is shown in blue, and the RPBE is shown in red.

As we have now shown that the main difference in PBE and RPBE behavior occurs in low electron regions, one might have thought there would be greater separation between the vacancy defect formation energies, which are the only places in any of the simulations in this work where electron density significantly decreases. Instead, however, we see more of a difference in the combined behavior the PBE and RPBE with the fundamentally different AM05 functional.

The derivation of the AM05 functional is fairly complex, and so only a brief description of the relevant pieces will be discussed. Where the PBE and RPBE are built upon the local description of the electron exchange and correlation in the homogenous electron gas (HEG), the AM05 determines exchange and correlation through an interpolation of the HEG behavior and a known jellium surface behavior. In this way, the AM05 can be thought of sub-system functional incorporating the effects of two distinct functionals, with the electron gas largely driving the bulk region behavior and the jellium surface contributing in near surface and low electron density regions. The AM05 is thus not dependent on the gradient of the electron density gradient, and so is not a true GGA functional. However, in the hierarchy of DFT functionals it is most directly related to the GGA tier for most intents and purposes.

The AM05 functional was developed specifically to improve upon the PBE treatment of surfaces while maintaining its treatment of the bulk region, so it makes sense that the only real difference we see in the formation energies in this work are for the internal surface containing vacancy defects. It's difficult to gauge the accuracy of the two functional variants, however, as the only experimental value is itself somewhat questionable. Because of the separate derivation of each functional type, it's also difficult to extrapolate the various success (or failure) of each in predicting bulk structural properties to the vacancy defect surface. We can, however, somewhat extrapolate the basic bulk behavior in order to gauge the interstitial defect accuracy. Doing so suggests that we should have the highest confidence in the PBE functional defect energies, as the PBE performed the most admirably in the bulk property calculations.

## 3.4 Conclusion

Point defect formation energies were modelled for fcc and bcc Th crystal lattices. In the fcc lattice, both Th-self defects and single uranium impurity defects were modelled. In the high temperature bcc β-Th lattice, only Th self-defects were modelled. A focus was placed on the relative performance of the PBE, RPBE, and AM05 functionals in predicting defect properties. Experimental defect formation energies in the Th system are scarce, however, so the primary evaluation of functional performance was centered on the functionals ability to reproduce common and well known bulk structural properties, such as lattice and elastic constants. In this, the PBE functional outperformed the other functionals for most properties with the RPBE close behind and the AM05 third.

The only real difference observed between the functionals in determining defect formation energies, other than the magnitude shifts in the general energy profile, was in the prediction of the vacancy defect. This was understandable as the main difference between each functional was in its treatment of surface regions, such the internal surface of a vacancy. Overall, we can separate the evaluation of functionals by the type of defect (*i.e.*, vacancy or interstitial). For the vacancy type, the lack of reliable experimental values leaves the functional evaluation inconclusive, but for the interstitial type of defect, which can be more closely connected to the bulk structural and elastic properties we should have the highest confidence on the PBE functional, out the three modelled. This work is presented in the hope that it might inspire future experimental investigations into the defect formations might be undertaken, from which accurate experimental defect formation energies could be obtained.

# CHAPTER 4. OSCILLATORY SEGREGATION BEHAVIOR IN NICKEL-CHROME SURFACES

Surface segregation is the phenomenon in which the top layers of an alloy's surface or interface exhibit an atomic composition different from the rest of the alloy [98]. Understandably, this phenomenon bears great significance in surface chemistry as it can directly influence the chemical reactions that drive important processes like catalysis, oxidation, and corrosion [99–102]. There are several factors that have been found to influence an alloy's segregation behavior, principal among these are differences in the pure metal surface energies of the alloy's component species and elastic strain release associated with atomic size mismatches between the component species [103–108]. The segregation behavior is ultimately governed by the combination of these properties, as well as other phenomenological and microscopic properties of the alloy such as heat of solution effects, which lower the Gibbs energy of the surface the most.

Because of the unique structural and electronic characteristics of a free surface, these driving forces can lead to a different segregation behavior in each of the top atomic surface layers. A commonly observed behavior in several transition metal alloy systems is a non-monotonic compositional variance with the distance to the free surface [109–114]. In a bimetallic alloy, this variance, often referred to as oscillatory segregation, can occur as an increase in the composition of an alloy component (relative to the bulk) in a single or several buried surface layers accompanied by a decrease in the composition of that same component species in the top layer. In terms of segregation energy, which is a measure of the change in the internal energy of system associated with moving a solute atom from a

bulk position to any of the top surface layers, this oscillation appears as a change in the sign of the energy as the atom moves from any one layer to the next. Examples of this oscillatory type behavior are shown in **Figure 4.1**, which depicts the calculated segregation energies found by Yu et al. [115] for several 3d, 4d, and 5d transition metals in a Ni(111) surface using density functional theory (DFT).

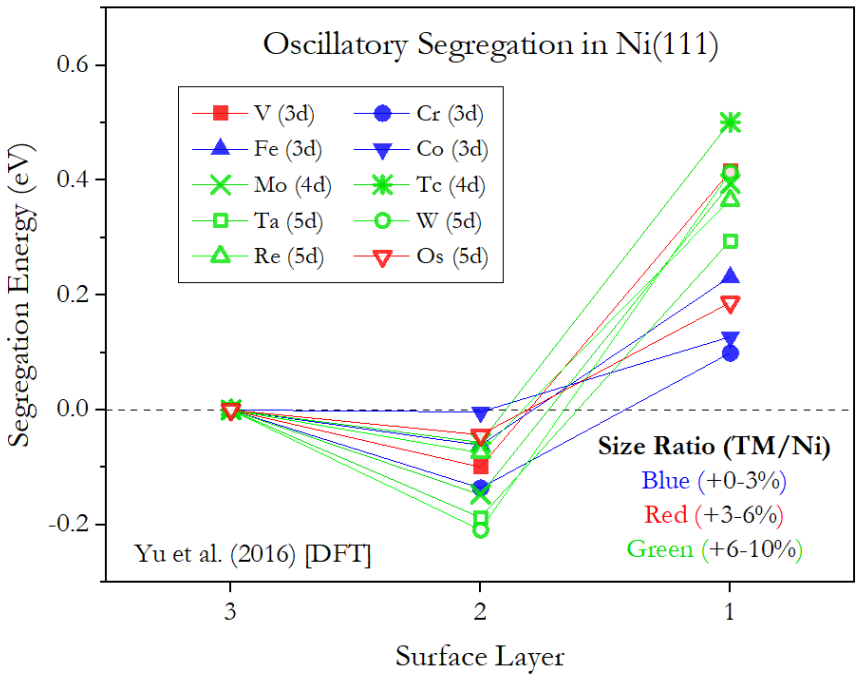


**Figure 4.1.** Oscillatory segregation energies calculated with DFT by Yu et al. (2016) [116] for transition metal (TM) segregation in a Ni(111) surface. Colors represent the relative atomic size ratio (van der Waals radii) of the segregating transition atom and the host Ni atom (Blue = +0-3% of the van der Waals radius, Red = +3-6% and Green = +6-10%). Solid symbols depict 3d transition metals, line type symbols depict 4d transition metals, and hollow symbols depict 5d transition metals, as indicated in the legend.

The energies fall into the negative when the solute atom is in the second layer, suggesting preferential segregation of the solute species to that layer, but then the sign of

the energy changes and becomes positive as the solute atom is moved to the top layer. The exact cause for this behavior has been up for some debate. While it's generally agreed upon that the large positive increases in the first layer segregation energy of these alloys are due to the differences between the pure metal surface energies of the individual alloy components in combination with atomic size mismatch effects [103–108], the cause for the second layer decrease, however, has only been somewhat notionally attributed to size mismatch and the easement of the accompanying lattice stresses as the top layers relax around the segregating atom [116,117]. Other longer-range oscillatory composition behaviors that extend many atomic layers deep into the surface have been studied quite extensively and can usually be attributed to short-range ordering behaviors or order-disorder transformation effects [111,113,114,118,119] but the very short-range oscillations exhibited in just the first few layers of these alloys have received very little focus thus far.

While atomic size mismatch is one possible explanation for this behavior, it may not be the main or only culprit in all cases as indicated by the lack of congruity in the distribution of size ratios among the second layer segregation energies in **Figure 4.1**. Additionally, Yu et al., also found non-oscillatory segregation behaviors for some transition metals in Ni, which are not shown in **Figure 4.1.** As Ni is generally one of the smallest transition metals, all of the metals studied by Yu et al., including those which did show an oscillatory behavior and those which did not, were larger than the host Ni, further raising the question of the extent of size mismatch effects.

This then begs the question, aside from relative surface energy and atomic size effects, what other factors could be influencing this oscillatory segregation behavior? The heats of solution pertaining to the relative bonding strengths of alloy components have been

found to have a sizeable effect in some systems, however, the strength of its influence has been inconsistent. A prime example of this is the Ni-Cr system, where the heat of solution contribution was found to be exceedingly small relative to other systems [116] and the relative atomic sizes of Cr and Ni are nearly identical [120,121] but as can be seen from **Figure 4.1**, the energy of Cr segregation in the second layer deviates from any expected trends and drops much lower into the negative than one would expect if the discussed features were the main driving factors.

In this study, we present a density functional theory study of Cr segregation in a Ni surface and show that there is indeed a buildup of lattice strain around the segregating Cr atom, but rather than these strains coming from a size mismatch they instead appear as a result of a rather significant amount of electronic charge transfer between the Cr and the neighboring Ni lattice. The Ni lattice effectively strips the Cr of a valence electron, leaving the Cr with a positive charge, which then leads to internal lattice strains as it interacts with its negatively charged Ni neighbors and with the non-uniform charge density exhibited by the free surface. We will show this by first calculating the segregation energy profiles of a single Cr atom moving through the top five layers of Ni (100) and (111) surfaces. We then more closely examine the extent of electronic charge transfer between alloy constituents through Bader charge analysis [122–125], followed by the displacement of the Cr atom, specifically in relation to the intrinsic charge density of the relaxed surface, and then finally the atomic displacements of the Cr's first and second nearest neighbors. Outside of a few investigations on the surface adsorption effects of highly electronegative O containing species [126,127] and a handful of studies on nanoalloy and nanoparticle systems

[128,129], the presence and effects of electronic charge transfer during segregation in clean alloy surfaces has received very little focus before this.

Additionally, Ni-Cr alloys, aside from being a particularly interesting case for the study of surface segregation, have many uses in industrial and commercial applications. From dental prosthetics [130,131] to high-temperature heating elements [132] and thermocouples [133] to, and perhaps most significantly, their promising potential for use in salt-facing piping and container components in molten salt nuclear reactors [134–138] and concentrated solar power systems [139–142], the bulk of the alloys' designed uses are predicated on its excellent corrosion and wear resistant properties at both low and high-temperatures and in harsh or volatile conditions. As many of these properties specifically involve interactions and the exchange of material at surface interfaces, the segregation behaviors exhibited by Ni-Cr alloys will almost certainly have a role in the alloy's performance for these applications.

## 4.1 Methods

DFT calculations in this work were performed using the Vienna Ab-Initio Simulation Package (VASP) [15–18] which uses a plane-wave basis set with a maximum cutoff energy of 400 eV, and the projector augmented wave (PAW) [19,20] description of electron-ion interactions. The PAW pseudopotentials used in this work came supplied with the VASP package and treated the semi-core p-states explicitly [143]. The Perdew-Burke-Ernzerhof (PBE) [11] generalized gradient approximation was used for the description of the exchange-correlation energy functional. Minimization of the electronic self-consistent loop was achieved when the energy difference between loops was below $10^{-6}$ eV and the

ionic minimization was satisfied when the individual forces on all atoms fell below 0.02 $eV \cdot Å^{-1}$. Partial orbital occupancies were set according to the smearing method of Methfessel-Paxton of order one [66], with a smearing width of 0.2 eV. Despite Ni being a ferromagnetic material, the introduction of Cr and high temperatures has been shown to remove magnetic ordering [144–146]. For this reason, we have chosen not to include spin polarization in these simulations. This has been demonstrated to have the effect of increasing the surface energy in some Cr surfaces, which subsequently increases the first layer segregation energy of Cr in Ni [147]. Nonetheless, these differences should not affect the arguments presented in this letter.

Segregation calculations were performed using surface slabs consisting of 144 atoms and 9 atomic monolayers for both the Ni(100) and Ni(111) surfaces. The slab structures were constructed so that the bottom 3 layers remained fixed in place while the top 6 layers were allowed to fully relax. A 14 Å vacuum was placed between the slabs in the Z direction and a 4 x 4 multiplication of the base unit cell was applied in the X-Y plane, resulting in 9 layers of 16 atoms each for both surfaces. Finally, a 6 x 6 x 1 Gamma-centered k-point grid was used to model each surface. The two slab surfaces used in this work are shown in **Figure 4.2**, which depict the Cr atom in the fifth layer of each slab and then each subsequent position of the Cr atom in the above layers.

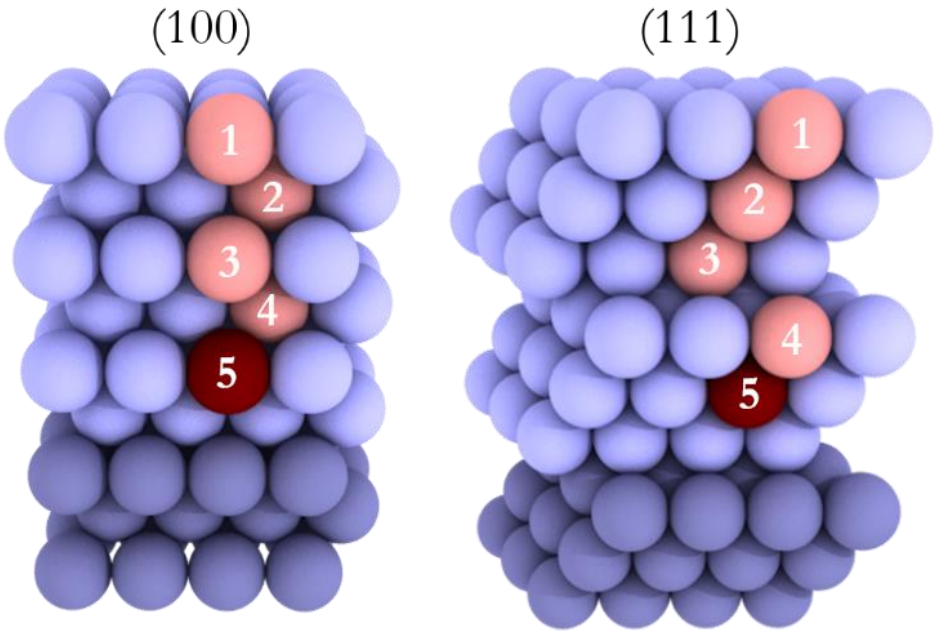


**Figure 4.2.** Cross-sectioned surface slabs used to model Cr segregation in the fcc Ni (*left*) (100) and (*right*) (111) surfaces showing the embedded Cr atom deep in the center of each slab. The Cr atom (dark red) is shown in the fifth layer, (*i.e.*, in the bulk reference position), and the lighter red atoms indicate the eventual position of the Cr atom as it's moved up through the surface. The darker blue atoms at the bottom of the slab depict Ni atoms that were restricted from moving during relaxation while light blue atoms indicate Ni atoms that were fully allowed to relax.

## 4.2 Results and Discussion

### *4.2.1 Segregation Energies*

Segregation energies are calculated in reference to the energy of the bulk-like state when the Cr atom is in the fifth layer (*i.e.*, the most distant point from the surface). The energy represents the difference between the energy of a surface with the Cr located in one of the top surface layers and the energy of the surface with Cr located in this fifth layer bulk reference state. A positive segregation energy for any layer position indicates a higher relative energy for that surface configuration and thus preferential Ni segregation in that

layer, while a negative energy indicates a lower total energy and thus preferential Cr segregation.

Calculated segregation energies for the (100) and (111) surfaces are shown in **Figure 4.3** (a) as a function of distance from the free surface, where each point represents the subsequent layer positions held by the Cr atom, as depicted in **Figure 4.2** by the lighter red colored atoms. The calculated segregation profiles for each surface show remarkable similarity to one another despite the physical and structural differences of each surfaces, which may be indicative of a strong electronic influence as opposed to differences stemming from the relative relation of the surface plane. The high segregation energies found for the first layer of both surfaces are in line with the notion that the higher surface energies generally exhibited by chromium surfaces relative to nickel surfaces should lead to the segregation of Ni in the first layer [147–151]. The first layer behavior also agrees well with the previous spin polarized DFT values of Yu et al. [116] and with Jeng et al.'s [152] experimental Auger electron spectroscopy measurements which showed preferential segregation of Ni to the top layer in a Ni-15%Cr alloy. That the energies of the (111) surface are lower than the corresponding (100) energies may be indicative of the lower surface energy and greater stability generally associated with (111) surfaces and allude to a greater ability for the (111) surface to facilitate and adapt to the electronic and structural disturbance introduced by the Cr atom.

The energy oscillation between the first and second layers was found to occur almost equally in both surface facets. A negative segregation energy was also found for the third layer but at a lower magnitude relative to the second layer, which suggests that the driving mechanism behind both negative energies is likely of the same nature for both

layers and that it becomes weaker further away from the free surface. Finally, a second oscillation was also found to occur, albeit a very subtle one, as the Cr atom moved between third and fourth layer positions, for both surfaces.

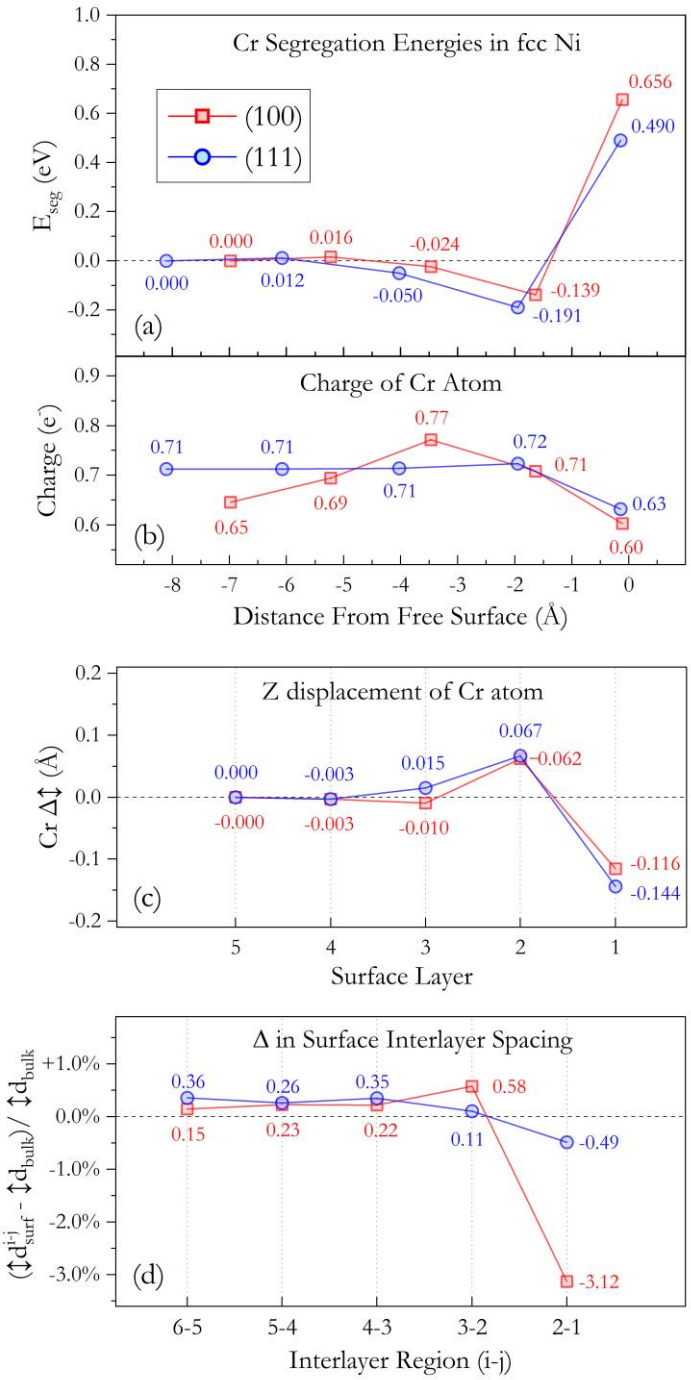


**Figure 4.3.** (a) The calculated segregation energy profiles for Cr in the (100) and (111) fcc Ni surfaces as function of distance from the free surface. (b) The corresponding atomic Bader charge of the Cr atom each for each of layer of both surfaces. (c) The out of plane displacement of the Cr atom in the Z (surface normal) direction found relative to average Z height of all other Ni atoms in the same plane. (d) The change in the interlayer distance between two surface layers (*e.g.*, 2-1 is the region between first and second layers) in the pure Ni surfaces relative to the natural spacing of the planes in the ideal bulk region.

The calculated Bader charge of the segregating Cr atom is also plotted for both surfaces in **Figure 4.3** (b) as a function of distance from the free surface. While there doesn't seem to be a consistent or obvious trend that can be immediately drawn from the charge profiles, the overall magnitude of the charge on the Cr atom is in itself quite remarkable considering this is a metallic system. The Ni lattice is able to strip more than half an electron's worth of charge from the isolated Cr atom, effectively ionizing it no matter where its located in the surface. The driving force for this charge striping may be related to electronegativity. Ni has a slightly higher electronegativity (1.91), than Cr's (1.61). Differences in electronegativity do not usually become significant enough to effect bonding until greater than 0.2-0.5, and so, while small, the electronegativity difference between Ni and Cr may suggest that Ni could be inducing some level of partial ionic bonding to occur around the Cr atom, as it strips away its electron charge.

This level of charge transfer in itself quite interesting in the context of oxidative and corrosive interactions, and particularly in regard the role it might play in the mechanisms fundamental to the Cr depleting corrosion in ionically charged molten salt systems [137,153–161]. Halide salts essentially become an ionically charged liquid when in molten form, so it seems probable that a partially charged Cr atom at or near the surface of the alloys may interact more strongly with the salt ions than the more relatively neutral Ni atoms. We see this same kind of behavior during oxidation processes. Cr oxidizes much more quickly than Ni in Ni-Cr and Fe-Ni-Cr alloys and steels, often forming a passivating $Cr_2O_3$ oxide layer on the surface. Cr exhibits much higher activities and diffusion rates in these alloys, particularly when Ni content is increased [162–164]. This could be taken as

supporting evidence to the occurrence of this high level of charge transfer between Cr and Ni.

### *4.2.2 Z Displacement of the Cr Atom*

The significance of the solute-host charge transfer in this system is in how the partially ionized Cr atom now interacts with its neighboring Ni atoms, which have themselves become slightly more negative, and in the Cr's interaction with the non-uniform charge density exhibited by the relaxed structure of the free surface.

**Figure 4.3** (c) shows the Z displacement (surface normal direction) of the Cr atom relative to the average Z position of all other Ni atoms in the same layer. Again, the behaviors in both surfaces are nearly identical, showing a large negative displacement in the first layer and a positive upwards displacement in the second layer of both facets. The most significant Z displacements are those occurring nearer to the surface, much like the calculated segregation energies, resulting in displacement profiles that bear a striking resemblance to the segregation energy profiles if either was inverted. It's the single, and subtle, deviation from this inverse segregation mimicry, and from the near identical behavior shared between both surfaces, however, that provides the most evident clue as to what is really driving the displacements. The deviation here is referring to the opposite displacement observed in the third layer of each surface. In the (100) surface, the Cr has a negative displacement when in the third layer, shifting slightly downwards towards the bulk of the material, but in the (111) surface, the third layer Cr exhibits a positive displacement, moving upwards just slightly towards the free surface.

#### 4.2.2.1 Relaxation of the Surface

The cause for this behavioral divergence comes from subtle differences in the natural atomic lattice structure exhibited by the two Ni surfaces. Namely, the interlayer spacing between the surface planes, and the extent to which they expand or contract in response to the reduced coordination states experienced by the atoms in top handful of layers. The fluctuations exhibited by each of the top five interlayer regions are shown for the pure Ni (100) and (111) surface facets in **Figure 4.3** (d) as the change in the interlayer spacing ($\updownarrow d_{surf}^{i-j}$) between each pair of surface layers (i-j) relative to the interlayer spacing of the corresponding planes in the bulk region ($\updownarrow d_{bulk}$). **Figure 4.3** (c) and **Figure 4.3** (d) are vertically aligned such that the atomic layers in (c) sit between the corresponding interlayer regions in (d). A negative value in the relative interlayer spacing indicates those planes have contracted and sit more closely to one another at the surface than in bulk, while a positive change indicates an expansion of the two lattice planes. A visual depiction of the surface layer relaxation is shown in **Figure 4.4**. Both surfaces show a significant compression of the first two planes followed by varied expansions of the remaining sub-surface layers. The main distinction is that the bulk of the expansion in the (100) surface is located in the highest sub-surface layers (*i.e.,* between layers two and three) while the expansions in the (111) surface appear to be more dispersed among the deeper sub-surface layers with the smallest expansion actually occurring between layers two and three.

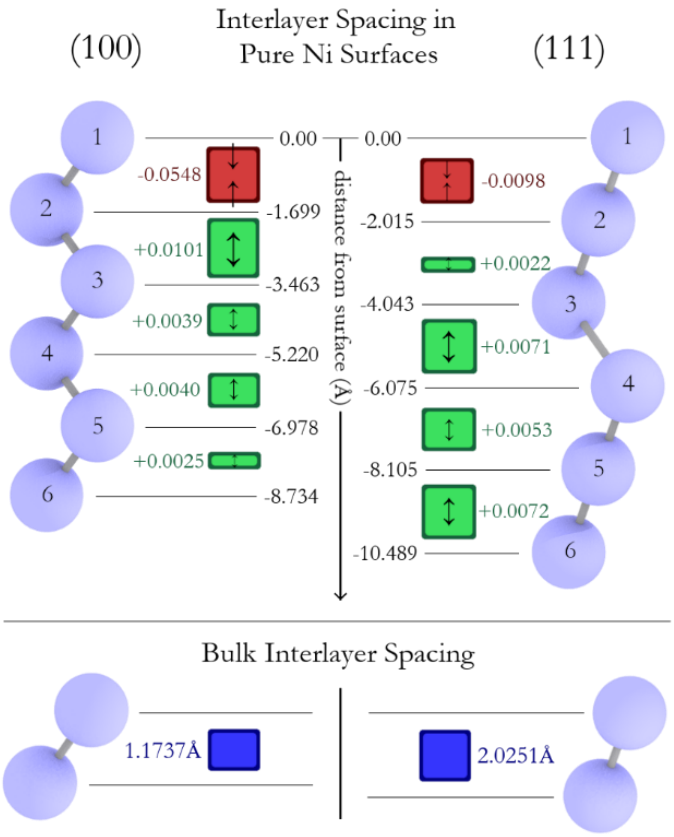


**Figure 4.4.** A visual depiction of the change in interlayer spacing exhibited at the (100) and (111) Ni surfaces, plotted in Figure 4.3 (d). The size and colors of the squares represent the magnitude and direction of the layer spacing change. Red squares show compression, green squares show expansion and the blue squares represent the ideal bulk spacing. The physical distance of each layer from the free surface and the actual change in the interlayer spacing are written in Å next to each layer, and interlayer region, respectively.

Because the surfaces exhibit slightly different relaxation behaviors, the local environment directly acting on the Cr atom is not just different between each surface but for the third layer specifically, it is opposite. In the (100) surface, the Cr sees a more compressed interlayer region just beneath it (interlayer region 4-3 in **Figure 4.3** (d)), relative to the more expanded region just above it (interlayer region 3-2 in **Figure 4.3** (d)). Conversely, in the (111) surface the Cr sees the opposite of this arrangement with the more

"compressed" region now located above (region 3-2) and the more "expanded" region below (region 4-3). In both cases, the Z displacement of the Cr atom was directed towards the more compressed, or smaller, of the two neighboring interlayer regions. This observation is significant because it is not restricted to just the third layer. Carefully examining **Figure 4.3** (c) and **Figure 4.3** (d) will show that the directionality of the Cr's displacement in all but the (100) surface's fourth layer is pointed towards the more "compressed" of the neighboring interlayer regions. That the fourth layer does not follow this trend is not a large concern as the displacements in these relatively deep layers are fairly small to begin with and so are practically negligible.

Recalling the partial ionization of the Cr atom, a reasonable assumption for the displacement behavior in these surfaces could be that the positively charged Cr is experiencing a stronger attraction to what is likely a higher relative electron density in the more compressed interlayer region and so is being pulled in its direction. In the deep surface layers, the Ni lattice is more tightly bound and supported, and so both the relaxation of the layers themselves (*i.e.*, the compression and expansion) and the displacement of Cr atom are subdued relative to the higher up layers just at the free surface. This, however, likely leads to a small buildup of stress which could raise the total energy of entire surface system. In the higher surface layers, the Ni lattice is more fluid and can more easily adjust and adapt to alleviate these stresses and so the Cr atom is able to push through and get much closer to the regions higher in electron density.

#### 4.2.2.2 Charge Density Difference

A useful tool in examining charge transfer effects in materials is a charge density difference (CDD) plot. This plot takes the electron charge density, calculated by a DFT simulation, and removes any charge density that is not changed or affected by the introduction of some defect or structure of interest. The resulting density plot shows a clear depiction of where electron density has accumulated or has been reduced and, in some cases, can visibly show the formation of bonds. In the case of our Ni-Cr surfaces, this charge density difference can be described mathematically as

$$\Delta\rho = \rho_{NiCr} - \rho_{Ni} - \rho_{Cr} \tag{38}$$

Here $\rho_{NiCr}$ is the charge density of the surface containing the Ni atoms and the segregating Cr atom, in units of $e^{-}\cdot A^{-3}$, and $\rho_{Ni}$ and $\rho_{Cr}$ are the charge densities belonging to just the Ni atoms in the surface and just the single Cr atom, respectively. These two charge densities are found by taking the atomic coordinates from the Ni-Cr simulation, removing either the single Cr atom or every Ni atom, and re-calculating the charge density. The resulting density difference ($\Delta\rho$) represents the change in electron density associated with substituting a Cr atom into a vacancy site in the Ni lattice.

In **Figure 4.5** we show the CDD corresponding to the charge transfer around the Cr atom in each of the top three surface layers for both the (100) surface (a-c) and the (111) surface (d-f). These plots show a cross-section of the charge density and so contain two distinct types of isosurfaces. The first type is the minimum isosurface value necessary for the charge transfer to be shown, which is depicted as a 3D volume with either a solid red

surface (for electron gain) or a solid blue surface (for electron loss). The second type of isosurface shows the magnitude of density difference within the 2D cross-sectional slice of the main 3D charge density. The color scale bars correspond to the density gradient in this second 2D isosurface.

It's clear the Cr atom is losing significant charge to the Ni lattice. In every configuration a sharp and intense region of electron density loss is visible immediately around of the Cr atom, which means the Cr keeps fewer electrons around itself when it's in the Ni lattice compared to if it were just a single neutral atom in space. This is just as the Bader analysis suggested. A red shell of charge density gain is also consistently present in each configuration, shown encompassing the inner blue core. This red shell represents the bonds formed between Cr and first nearest neighbor (1nn) Ni atoms which are not present in the $\rho_{Ni}$ and $\rho_{Cr}$ densities. The large blue 'plume' of low electron density extending out above the surface when the Cr is in the first layer is also interesting in the context of corrosion and oxidation. While the plume is not an exact depiction of the actual charge at the surface, it shows how the relative charge density might appear to oxidative or corrosive particles hitting and moving across the surface and how these species might perceive the Cr and Ni atoms differently.

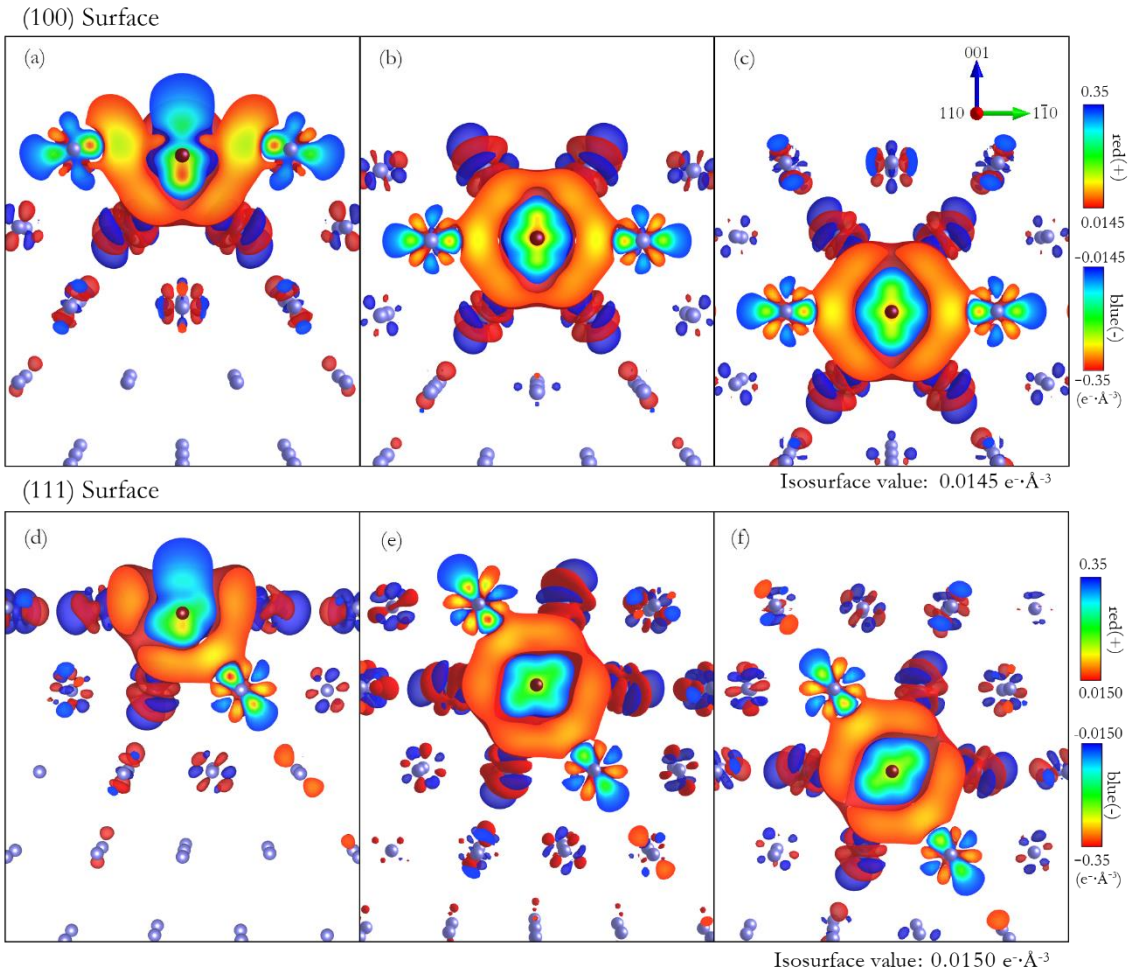


**Figure 4.5.** Charge density difference (CDD) associated with substituting the Cr atom into each of the top three layers of the (100) (a-c) and (111) (d-f) surfaces. The images show the simulation cell cleaved in half vertically along the plane of the Cr atom. Two distinct types of isosurface are visible because of this. First, the regions of electron gain and loss are depicted by the 3D red and blue regions, respectively, and only show areas in which the change is greater than the minimum isosurface value noted at the bottom of each set of panels. The second surface, the flat 2D cross-section of these 3Dregions, visible perpendicular to the plane of the image itself, shows the relative magnitude of the charge difference within thin the 3D cloud. The color scale bars, which depict change ranging from the minimum isosurface value to the maximum difference ($\pm 0.35\ e^{-}\cdot A^{-3}$), correspond to this inner 2D isosurface. The distinct blue orb like region around the Cr atom (dark red) show how electronic charge the has been stripped from the Cr and repositioned closer to the Ni atoms (light blue) in the red shell like region around the blue core.

The CDD plots in **Figure 4.5** also show the asymmetry of the charge density in the interlayer regions above and the below the segregating Cr atom. These asymmetries are visually very subtle but carefully examining the relative size and shape of the red shell regions above and below the Cr atoms will reveal slight differences. Recall in the (100) surface the Cr shifted towards first interlayer region when it resided in either of the first two layers and towards the third interlayer region when it sat in the third layer. In **Figure 4.5** (a-c), the relative size of the density increase is just slightly larger or "bulkier" in the regions the Cr was found to have shifted towards. The same applies equally to the (111) surface configurations shown in **Figure 4.5** (d-f), however, because of the ABC stacking of the (111) planes the relative sizes of the above and below densities are slightly harder to discern. Differences in the way this red shell region interacts with the other smaller red "gain" regions of the above and below Ni atoms are apparent in the (111) surface, however.

### *4.2.3 Distortion of the Nearest Neighbor Ni Atoms*

A sizeable distortion of the lattice sites around the segregating Cr atom was also observed in these simulations. A contraction of the first nearest neighbors (1nn) towards the Cr atom was observed in the deeper layers of both surfaces while a varied contraction and adjustment of the 1nn's and 2nn's was seen when Cr was in one of the top two layers in each surface. The 1nn and 2nn displacements are shown around the Cr atom for the top three layer configurations of each surface in **Figure 4.6**.

The displacements, which are shown with color coded arrows that have been dramatically scaled up in length for visibility, show a sizeable buildup of strain forms around the Cr when it's in the deeper bulk like layers, and that as the Cr gets closer to the

surface the surrounding Ni atoms are able to more easily adjust their positions to alleviate the Cr induced stresses. When the Cr is in the second layer this results in a slightly reduced level of contraction in the 1nn Ni atoms with a slight upwards shift in the Ni atoms directly above the Cr. When the Cr is the first layer, the 1nn and 2nn Ni atoms all move upwards around the Cr, lifting slightly out and away from of the surface and forming what could be described as a volcano like shape around the recessed Cr atom.

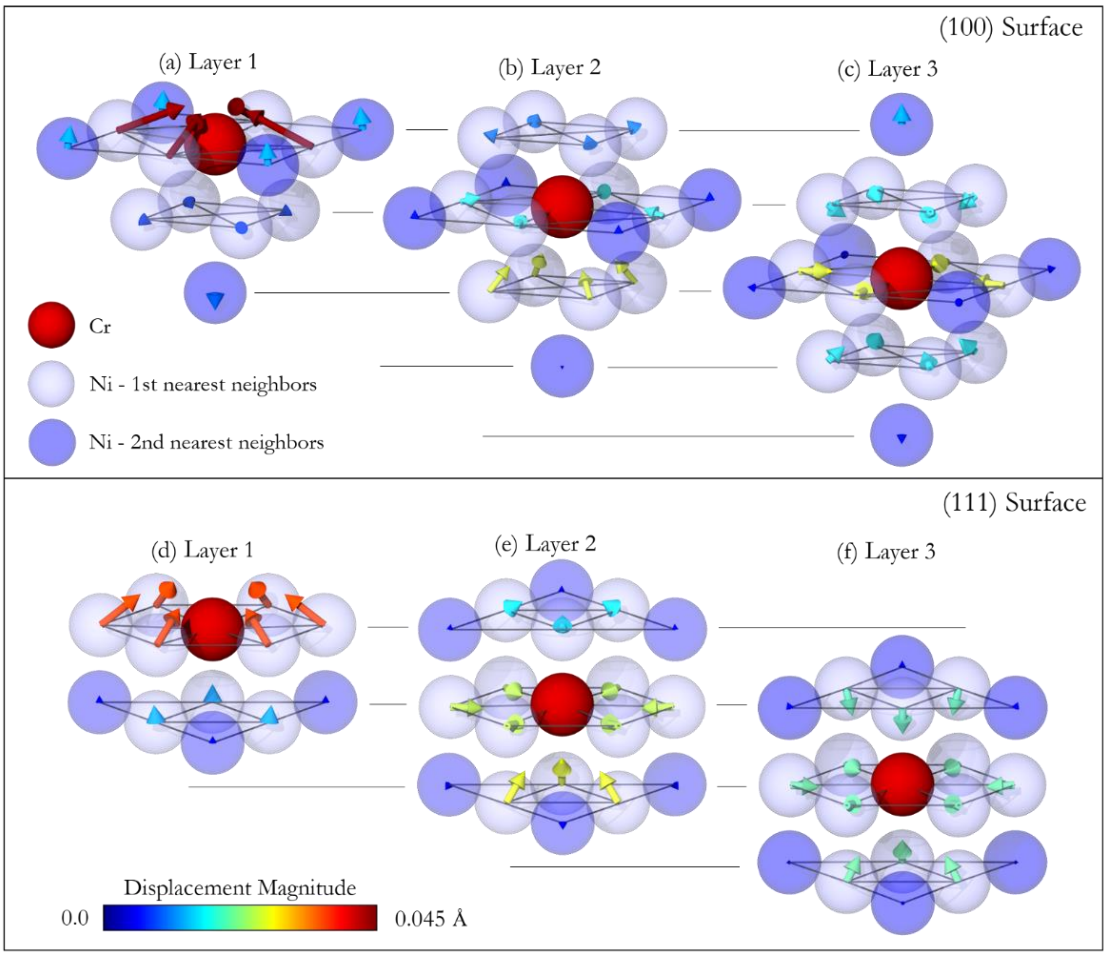


**Figure 4.6.** Displacement of the first and second nearest neighbor (1nn and 2nn) Ni atoms around the Cr in the top three layer configurations of each surface. The Cr atom is depicted in red, the 1nn atoms in light blue and the 2nn atoms in the darker blue. The displacements are drawn 25x larger in scale for visibility and colored according to the relative magnitude of each displacement. Each surface shows similar behavior: a more or less uniform contraction around the Cr in the third layer, a contraction of the same plane and below plane Ni atoms but upwards shift of the above plane Ni atoms when the Cr is in the second layer, and a significant upwards and inwards shift of all the nearby Ni atoms when Cr is in the first layer.

This distortion behavior coincides quite well with the conventional view of oscillatory segregation behaviors in alloys. This is that the negative second layer segregation energy results from the elastic release of stresses induced by the solute atom

in the lattice, which are unable to escape and dissipate when they are locked deep in the bulk regions. This appears to be true for these Ni-Cr surfaces as well, with the distinction being, however, that these stresses arise from the partial ionic like interactions of the Cr and Ni, and not from pure atomic size mismatch which had been only notionally suggested before [116,117]. As can be seen **Figure 4.1**, the size mismatch between Cr and Ni is very small with Cr being the slightly bigger of the two. One should expect then, if anything, to the see the Ni atoms be slightly pushed away by the Cr atom and compressed against the further out Ni lattice, exactly the opposite of what we see happening in these surfaces.

This lattice contraction results from the positive Cr atom pulling on the 1nn and 2nn Ni atoms, which have themselves become slightly negative in charge after taking electrons from the Cr. The relaxation and alleviation of these charge induced stresses in the top two layers is clearly visible in the size and direction of the 1nn and 2nn displacements seen in these configurations in **Figure 4.6**. The Ni displacements in these layers also coincide with the Z displacements of the Cr atom, showing how the surface is able to adjust and reorient itself to account for the slightly out of plane positions held by the Cr, while also alleviating stress.

The negative second layer segregation energy found for both surfaces is more likely than anything to be a result of the elastic release of this charge induced lattice stress, stemming from both the ionic like interaction of the Cr and Ni and from the interaction of the Cr with the non-uniform charge density of the surface.

## 4.3 Conclusions

In summary, these results show that the oscillatory segregation behavior of Cr in Ni can be attributed to the redistribution of charge around the Cr atom and an ensuing release of the induced elastic strain near the free surface. This is opposed to the previously held, and slightly different, belief which incorrectly posited that the energy lowering elastic strain release at the surface occurs in order to alleviate stresses stemming from an atomic size mismatch between the host Ni and solute Cr atoms. As Cr and Ni are nearly identical in size, the link between size mismatch and the observed elastic strain was weak. Our DFT calculations, however, show evidence that a stronger link may exist between the elastic strain buildup and an ionic-like bonding behavior between the Cr and its closest Ni neighbors. This ionic behavior resulted from the electron charge transfer between the Cr and Ni atoms, in which the Ni lattice partially ionized the Cr atom by stripping nearly an entire electrons worth of charge from it. This electron striping behavior occurred nearly equally regardless of the Cr's position in the lattice (*i.e.,* whether in the bulk or near the surface) and regardless of specific surface facet.

The positively charged Cr atom showed a tendency to interact strongly with electron dense regions in the lattice. This ionic interaction could be broken down into two distinct components. First, the partially ionized Cr atom was found to be strongly attracted to, and physical pulled towards, the neighboring inter-surface layer region that exhibited a greater degree of compression (or lesser degree of expansion) and thus a higher electron density. This resulted in the Cr atom shifting out of plane with its nearby Ni atoms. Second, the Ni atoms encompassing the Cr atom, which were also partially ionized by the additional valence charge, were found to contract towards the Cr atom. This results in a further accumulation of lattice stress in the deeper surface layers. Closer to free surface, the lattice

was able to more easily adjust and relax to alleviate the induced stresses, lowering the overall energy of the system, and thereby the segregation in the second layer.

The occurrence of this high level of electric charge transfer between the Cr and Ni is important in regard to the design of molten salt reactor systems. The salt essentially becomes a molten ionic “soup” when heated to operational temperatures within these reactor systems and so strong interactions between the salt and the ionically charged Cr atoms embedded in the alloy surface are likely to always be present. As it’s not likely that the charged ionic nature can be engineered out of the salt, focus must be placed on designing alloys that can limit this Ni-Cr trasnfer interaction. Alloy additions that can limit the electron transfer between Ni and Cr might offer some level of passive protection against, or at minimal, reduction in, overall corrosion and so should be pursued.

# CHAPTER 5. THE INFLUENCE OF MOLTEN SALT SPECIES ON SEGREGATION BEHAVIORS IN NICKEL-CHROME SURFACES

Molten salt has long been considered an excellent candidate for use as a coolant media in heat-transfer applications. This is because of their excellent chemical stability at high temperatures (> 500°C), low melting points, high thermal conductivities and specific heats, radiolytic stability, and low vapor pressures (< 1 atm) [165–168]. Coolants that exhibit these properties would be particularly useful for the development of concentrated solar and molten salt nuclear reactor technologies designed for efficient energy generation and hydrogen production [136,165,169]. The potential for use in nuclear reactors is especially exciting as molten salts could serve as a fuel carrying medium inside the reactor core potentially allowing for online refueling and recycling of minor actinides and fission products without the need to temporarily shut down the reactor [170,171].

The choice of salt for these applications largely comes down to those with low enough melting points and those with phase stability within operational temperatures, which is why the most commonly investigated salts are eutectic mixtures [172,173]. Three such salts currently under investigation are the halide-based FLiBe (LiF-$BeF_2$), FLiNaK (LiF-NaF-KF) and NaCl-$MgCl_2$ mixtures.

High-temperature compatibility with salt-facing structural materials is an equally important factor when designing salts for use in molten salt systems. While most proposed salts and structural materials show good individual long-term high-temperature stability,

corrosion interactions at the salt/container interface tend to limit the overall lifetime and performance of many structural components. In many other material systems, it is common for passive oxide films to form on surfaces that serve to inhibit further oxidation and corrosion but in molten salt systems most passivating surface layers are quickly dissolved in the molten salt [174,175]. This means corrosion effects must be limited by designing molten salt systems with only highly compatible salts and structural materials.

Insights from the Aircraft Reactor Experiment (ARE) and the Molten Salt Reactor Experiment (MSRE) carried out at Oak Ridge National Laboratory in 1955 and 1965, respectively, led to the development and choice of Ni-based superalloys, such as Hastelloy-N, for container and piping materials in molten salt systems [136,176]. Ni is commonly alloyed with other metals such as Cr to increase its high-temperature corrosion and steam oxidation resistance and to improve its creep strength [177]. The additional Cr content also allows for the growth of a passivating oxide layer on the outer air-facing surface of components [178].

Unfortunately, despite the improved corrosion resistance, corrosion does still occur. In Ni-Cr alloys facing a high-temperature molten salt for extended periods of time corrosive degradation will accrue along surface interfaces via the dissolution of Cr atoms into the salt [153,154]. Experimental studies have observed that Cr depletion is accelerated when impurities and oxidizing contaminants are present in the salt and when initial Cr contents in the alloys are high [137,158,160,165,166].

While many studies have focused on measuring corrosion rates and other related characteristics associated with Cr-depletion in Ni alloys, far less effort has gone onto

studying the little understood atomic-level mechanisms underlying this form of corrosion. Understanding these mechanisms could considerably aid in the development of salts and materials for future molten salt systems. These systems are particularly difficult to study experimentally, however, due to the highly corrosive and volatile high-temperature environments and due to the extreme sensitivity of these systems to the effects of contamination. In this study, therefore we employ the use of Density Functional Theory (DFT) to investigate the local atomic-level interactions that might be occurring at the surface between alloy and salt constituents in an effort to assist or guide the next generation experimental and theoretical studies.

## 5.1 Literature Review

First, however, a thorough review of the existing experimental and theoretical understanding of segregation phenomena in Ni-Cr and other relevant alloy systems is warranted. In the available literature, only a handful of studies can be found which investigate Cr segregation effects in Ni or Fe alloys, most of which are not entirely applicable to the high temperature and corrosive conditions that come with molten salts. For example, several of the most recent of these studies have almost exclusively focused on nanoparticle materials, which cannot be expected to behave similarly to bulk material surfaces due to the significant difference in surface area to volume ratios [179–182]. Additionally, many of these studies have been focused on the role of magnetic ordering in Cr segregation, something that is not likely to be present in the salt containing alloys under the operating conditions required for molten salt systems [144–146,179].

The remaining studies, which are applicable to molten salt systems, are limited and at best represent only selective cases which were often performed under inert argon or vacuum atmospheres. Nonetheless, they do present some useful information. For example, Takahashi et al. [183] investigated Cr segregation in 304 stainless steel using atom-probe tomography (APT) after heating at several different high temperatures and found that the Cr concentration in the top few atomic layers increased while a Cr depletion zone, with a 0% Cr concentration, formed just below those top layers. The Cr-depletion zone was observed to disappear after heating above 600°C. Clauberg et al. [184] also investigated Cr segregation, but in an Fe–25%Cr–2%Ni–0.1%Sb–N alloy using Auger electron spectroscopy (AES) and low-energy electron diffraction (LEED), observing the preferential cosegregation of Cr and N up to 500°C before Ni and Sb segregation dominated. Lastly, Jeng et al. [152] used AES to investigate Cr segregation in a representative Ni-15%Cr alloy and found, that while under a vacuum and within a temperature range of 500 to 650°C (the max temperature studied), Ni preferentially segregated to the surface, contrary to the predictions of early empirically derived theoretical models at the time. Many of these early segregation models were later found to be unable adequately model the segregation phenomena in many alloys systems, however.

Other techniques like X-ray photo-electron spectroscopy (XPS) measurements of surface core level binding energy shifts (SCLS) can yield highly accurate surface segregation information but only for a limited range of alloys where the solute shares a Z+1 (atomic number) relationship with the host material [185,186]. The lack of existing experimental studies regarding not just Cr segregation, but the surface segregation behavior in many of the transition metal alloys, can likely be attributed to the difficulties and

limitations associated with the LEED and XPS-SCLS methods, and to the inherent sensitivity of many metal surfaces to their surrounding environments. Bohra et al. [179], for example, was unable to transfer their Ni-Cr nanoparticle specimens from the glove box to the TEM (transmission electron microscope) without acquiring significant levels of oxygen contamination along the way.

The limited availability of experimental segregation data has made the development of reliable and consistently accurate theoretical segregation models difficult. Several early empirical models, born out of the Langmuir-Mclean relation or Miedema's model [187] and the tight-binding (TB) approximation[188–194] failed to reliably predict surface segregation features observed in many transition metal alloy systems. On the contrary, though computationally expensive, non-empirical ab-initio models based on the Green's function linear-muffin-tin-orbital (GF-LMTO) method with the atomic sphere approximation (ASA) were able to consistently reproduce segregation behaviors in transition and rare-earth alloys in line with available experimental data [107,108,147,195,196]. These works prompted several more ab-initio studies which would seem to successively improve upon the accuracy of ab-initio segregation behavior predictions by extending the level of approximation or ab-initio formulation with methods like the coherent potential approximation (CPA) [103,104,197], or the Green's Function Korringa-Kohn-Rostoker (GF-KKR) method [198]. These studies were some of the first to highlight and prove the importance of surface energy and crystal structure in surface segregation phenomena.

Following the early successes of the previous all-electron ab-initio methods, which had achieved a high level of scientific confidence in behavior prediction, the projector

augmented wave (PAW) based density functional theory (DFT) method, with a significantly lower computational cost, would move to the forefront of ab-initio segregation modelling efforts. The plane-wave based DFT models allowed for the simulation of larger system sizes than the all-electron methods could achieve, enabling investigators to explore more complex segregation behaviors in a far more encompassing range of transition metal alloy systems. [116,199–202]. In one such investigation, Yu et al. [116] was able to fit DFT data calculated using the Perdew-Burke-Ernzerhof (PBE) [11] description of the generalized gradient approximation (GGA) for the exchange-correlation functional to a model which incorporated the weighted contributions from phenomenological properties like the relative surface energy, heats of solution, and atomic size mismatch, and was able to achieve a consistently high degree of accuracy when compared with known experimental data. This is the same theoretical segregation study cited in CHAPTER 4. Recall, their calculated segregation energies for Cr in a Ni (111) surface under a vacuum precisely matched the previously mentioned AES experimental measurements made by Jeng et al. [152].

While these models have generally shown a high level of accuracy and should serve to instill confidence in DFT segregation calculations, the potential effects of surface adsorbates or other surface interactions on segregation have largely been overlooked and excluded from the analyses of these segregation studies. In many systems this may be fine, but in those which exhibit surfaces sensitive to their external environments, like those susceptible to oxidation (*e.g.,* Cr containing Ni alloys) or to the corrosion observed in molten salt systems, a more thorough analysis of segregation behaviors should be sought.

Fortunately, this can be fairly easily done in plane-wave DFT surface calculations through the direct inclusion of surface adsorbates in segregation calculations.

It is a fairly simple task to repeat the segregation simulations of Chapter 4, with salt adsorbates placed onto the surface just above the segregating Cr atom. In fact, this type of adsorption-segregation calculation has been demonstrated already for several other types of material systems interacting with common atmospheric species like O and C [199,203–205]. In almost all of these cases the interaction of the surface with its neighboring environment significantly affected the surface segregation behavior within the alloy, even completely reversing the tendency of solutes to segregate in some cases. Yin et al. [206], for example, used GGA-DFT calculations to study the effect of F adsorbates on Cr segregation in the (111) surface of a Ni-Cr alloy and they indeed found that the Cr segregation energies in the F covered surfaces were not just lowered but were actually reversed relative to that in a clean or vacuum covered surface, meaning that segregation of Cr to the top layer was now predicted to be energetically favorable when F atoms were present above the segregating Cr atom.

While the halide species in molten salts are believed to play some role in the corrosion of Cr containing alloys, as demonstrated for F by Yu et al., a detailed analysis of the corrosion studies in existing Cl and F literature, such as that provided by Raiman et al. [135] suggests that overall corrosion rates seem to be most strongly correlated to salt purity, and that salts considered to be very pure generally demonstrate significantly lower corrosion rates relative to their more impure counterparts, regardless of the type of salt or alloy material. High moisture levels, for example, have specifically been linked to increased levels intergranular corrosion in several Ni-based alloys [137,160]. This raises

the question of what effects impurity species, such as O and H, might have on surface segregation behaviors in these alloy systems relative to the F and Cl halide species.

In light of this, the present study investigates the relative roles of adsorbed salt species and $H_2O$ based impurities in the surface segregation phenomena of a Ni based alloy. An electronic level description of the atomic interactions among the Ni, Cr, and salt ions during surface segregation is modeled using the plane-wave GGA-DFT method for a single Cr atom segregating in a Ni surface. The low-index (100) surface of fcc (face-centered-cubic) Ni was modeled for the relative simplicity of its unique surface adsorption sites and for the fact that the (111) fcc surface has already received some focus in this regard. Calculations are first performed for surface configurations in which a single Cl, F or O atom is placed into one of three adsorption positions above the Cr atom. The adsorption sites correspond to the top, bridge, and hollow positions of the (100) surface and will be described shortly. Then a second set of segregation calculations is performed with Na, Mg, or H individually attached to the back of each of adsorbed anions.

## 5.2 Methods

### *5.2.1 Surface Segregation Energy*

The calculation of surface segregation energies was described already in CHAPTER 4, but for completeness a description will be provided here as well. Recall that this calculation is a relatively simple one which involves finding the internal energy difference between a system with a solute atom located at the surface and a reference system with the same solute atom located somewhere in the bulk region. This allows for the calculation of segregation energies to be obtained for each individual atomic layer of

the surface. For any specific atomic surface layer, $i$, the segregation energy, $E_{seg,i}$, of a Cr atom in a Ni surface is then simply

$$E_{seg,i} = E_{DFT,i} - E_{DFT,bulk} \tag{39}$$

Where $E_{DFT,i}$ is the DFT calculated energy of a surface with a Cr atom located in the $i$-th surface layer and $E_{DFT,bulk}$ is the DFT calculated energy of a surface with a Cr atom located in a layer corresponding to the bulk region. In this case, $i = 1$ would correspond to the top-most layer, $i = 2$ to the second atomic layer from the surface, and so on until the layers become indistinguishable and representative of the bulk region.

### *5.2.2 Density Functional Theory Calculations*

The DFT calculations in this work were performed using the Vienna Ab-Initio Simulation Package (VASP) [15–18] utilizing plane-wave basis sets and the projector augmented wave (PAW) [19,20] description of the electron-ion interactions. The Perdew-Burke-Ernzerhof (PBE) [11] form of the generalized gradient approximation (GGA) is used for the description of the exchange-correlation energy functional. Other XC-functionals have been developed that might offer better descriptions of surface systems, such as the RPBE or AM05, but there is specific lack of experimental data to compare to in this work, so the PBE functional which has a proven track record in modeling solid alloy systems was chosen for this work. The use of other functions would likely result in slight adjustments to lattice constants and segregation energies, but overall trends are likely to remain the same. As experimental data in these systems is either not existent or precise

enough to resolve minor differences in segregation energy magnitudes, the use of these other less vetted XC-functionals is not totally warranted.

For all calculations, the maximum energy cutoff for the plane-wave basis sets was limited to 400 eV, the minimum energy break condition for the convergence of the electronic self-consistent loop was set at $10^{-6}$ eV, and the ionic convergence break condition was met when forces on all atoms fell below 0.02 $eV \cdot Å^{-1}$. For all structural relaxation calculations, partial orbital occupancies were set according to the smearing method of Methfessel-Paxton of order one [66], with a smearing width of 0.2 eV.

All frozen-core PAW pseudopotentials used in these calculations came supplied with the VASP library. In some cases, based on the analysis and recommendations of Jain et al. [143], pseudopotentials were chosen for atoms that treated the semi-core p-states as explicit valence states that could partake in bonding interactions. The pseudopotentials used for each atom type in this work are listed in **Table 5.1**, according their listed name in the VASP database, along with the electronic valence configuration and number of valence electrons included in each pseudopotential. The "_pv" extension indicates the pseudopotentials that treat semi-core p-states explicitly. The inclusion of semi-core p-states in these calculations was seen to lower the calculated segregation energies by more than 0.05 eV in some cases.

**Table 5.1.** PAW pseudopotentials used in this work. The _pv extension indicates pseudopotentials in which semi-core p-states are treated explicitly.

| Atomic species | PAW pseudopotential | Valence configuration | Valence electrons |
|---|---|---|---|
| Nickel | Ni_pv | $3p^6\ 3d^8\ 4s^2$ | 16 |
| Chromium | Cr_pv | $3p^6\ 3d^5\ 4s^1$ | 12 |
| Chlorine | Cl | $3s^2\ 3p^5$ | 7 |
| Fluorine | F | $2s^2\ 2p^5$ | 7 |
| Oxygen | O | $2s^2\ 2p^4$ | 6 |
| Hydrogen | H | $1s^1$ | 1 |
| Sodium | Na_pv | $2p^6\ 3s^1$ | 7 |
| Magnesium | Mg_pv | $2p^6\ 3s^2$ | 8 |

Additionally, just as in CHAPTER 4, non-spin polarized calculations were performed in this present study. Again, this choice was made to prevent the formation of magnetic ordering effects in the Ni-Cr surfaces. It has long been experimentally known that the Curie temperature and magnetic moments in Ni alloys decrease quickly with the addition of even small concentrations of Cr [145,146,207,208]. The operating temperatures expected for molten salt systems are far above the Curie temperatures of these Ni-Cr alloys, and so magnetic ordering effects are not likely to be present in these alloys or at their surfaces during operation. Spin-polarization was thus excluded from these calculations in order to most accurately represent the Ni-Cr surface behaviors expected in molten salt systems.

In previous ab-initio calculations, spin-polarization has also been shown to have a sizeable effect on the calculated surface energies of Cr surfaces[147] and so the results presented in this work will be discussed in relation to those spin-polarization effects to an extent.

### *5.2.3 Surface Slab Construction*

The (100) surface slab used in these calculations was the same as the one used for the clean surface calculation in CHAPTER 4. To construct this surface, an initial fcc unit cell containing 4 Ni atoms was modeled to determine the optimum lattice spacing for a non-spin polarized PBE calculation. The lattice constant was calculated using the Birch-Murnaghan equation of state fitting method in order to avoid error inducing Pulay stresses in the calculation of the stress tensor. This yielded a lattice spacing of 3.512 Å for the 4 atom fcc Ni unit cell. This 4 atom unit cell was then reduced in the X-Y directions and rotated to align the <110> direction with the X-axis, resulting in the less commonly used 2 atom primitive unit cell for the fcc lattice. The new X and Y direction lattice constants were then 2.483 Å while the Z direction lattice constant remained 3.512 Å. This 2 atom structure was then used as the base unit structure for the creation of the (100) surface slab supercells.

Testing found that 4 primitive unit cell lengths in the X and Y directions were enough to remove spurious interactions between both the embedded Cr atom and the surface adsorbates with their images across the periodic boundaries of the supercell. A similar test of the height of the vacuum region above the surface found that a 14 Å vacuum was adequate in preventing interactions between the periodic slabs and surface adsorbates in the Z direction and allowed for relatively “tall” surface adsorbate structures to be modelled with confidence. A gamma centered k-point grid of 6 x 6 x 1 was found to be sufficient in minimizing the calculated energies for these 4 x 4 surface slabs.

The segregation calculations in this chapter were performed using two different variants of this slab supercell which differed only in the number of atomic layers included

in the Z direction. For the initial segregation calculations, the full slab, which was the same slab was used for the clean surface calculations in CHAPTER 4, was used to model the configurations in which only a single anion was adsorbed to the surface. Recall that this slab, which we'll refer to as the full slab and which is the larger (or taller) of the two slabs variants, included 9 atomic layers, consisting of 144 atoms in total. In this full slab, atoms in the bottom 3 layers were fixed in place and restricted from moving during relaxation so as to enforce a bulk region structure on the bottom end of the slab, enforcing the "half-slab" structure. It was found that with 9 layers in total, when the top 6 layers were relaxed, the 2 layers immediately adjacent to the restricted layers (*i.e.,* layers 5 and 6 if layer 1 is the top layer of the surface) maintained the spacing of the bulk lattice in the Z-direction.

This 9 layer half-slab variant, shown in **Figure 5.1**, was specifically used for the calculations in which the Cr atom segregated under a surface covered by only a single F, Cl, or O adatom (adatom = *ad*sorption *atom*). As stated before, in these surfaces, when the Cr atom was located in the fifth layer (from the surface) it was considered to be in the bulk, and so served as the reference bulk energy, $E_{DFT,bulk}$, for the segregation energy calculation. This is important to restate here because as we will see that for next slab variant the fifth layer is no longer selected as the bulk reference layer.

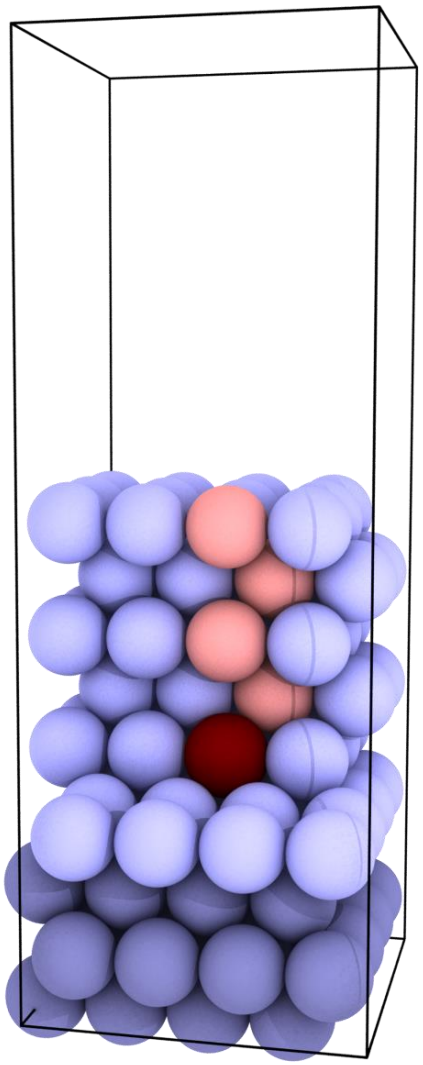

**Figure 5.1.** The 9 layer (100) fcc Ni surface slab used in this work for modelling the single anion segregation energies. The Cr atom (Dark Red) is shown embedded center of the fifth atomic layer and its subsequent positions in each of the above layers are indicated by the light red atoms. Atoms shown in light blue depict fully relaxable Ni atoms, and atoms shown in dark blue are Ni atoms that have been locked to enforce a bulk behavior.

The second slab variant used in this work was a shorter variant of the slab shown in **Figure 5.1**, consisting of only 6 atomic layers and 96 atoms in total. This smaller slab was used for the second set of calculations in which Cr segregation was modelled under

surfaces containing the more complex surface adsorbate structures consisting of anion-cation pairs. In this slab, only the bottom two layers were restricted during relaxation and the reference bulk layer was chosen to be the third atomic layer from the top of the surface, a commonly chosen reference layer in many ab-initio segregation calculations. This shorter slab variant was used for these calculations primarily to reduce the computational cost and because it would be observed from the first set of calculations that the energy differences between surfaces with the Cr atom in the fifth, fourth and third layers would be negligible no matter what is adsorbed to the surface and so were not necessary to further evaluate.

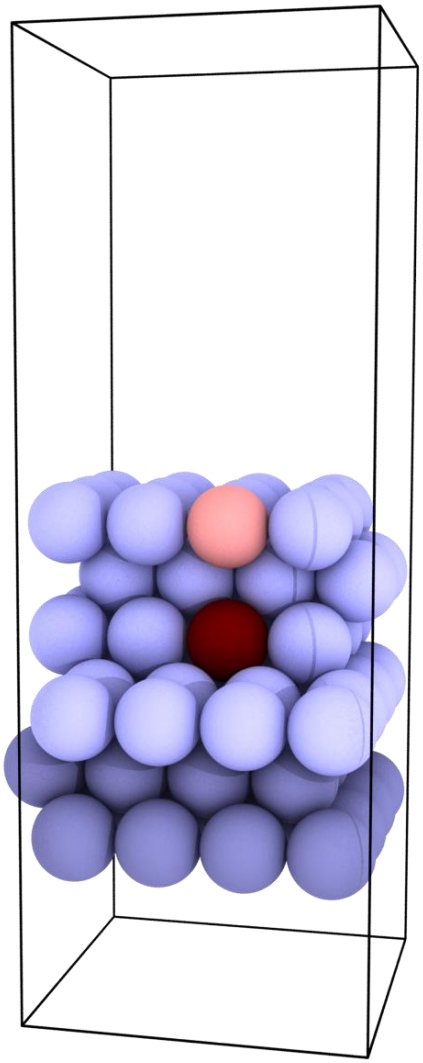

**Figure 5.2**. The 6 layer (100) fcc Ni surface slab used in this work for modelling the single anion segregation energies. The Cr atom (Dark Red) is shown embedded center of the third atomic layer and its subsequent position in the first layer is indicated by the light red atom. Atoms shown in light blue depict fully relaxable Ni atoms, and atoms shown in dark blue are Ni atoms that have been locked to enforce a bulk behavior.

## 5.3 Results and Discussion

The calculated segregation behavior of Cr in a clean Ni (100) surface was already presented and discussed in CHAPTER 4, however, it will be useful to briefly review that behavior here at the start of this discussion because it will serve as the reference behavior

for which many of the remaining calculations will be compared to. The clean surface segregation profile is shown again in **Figure 5.3** for just the (100) surface.

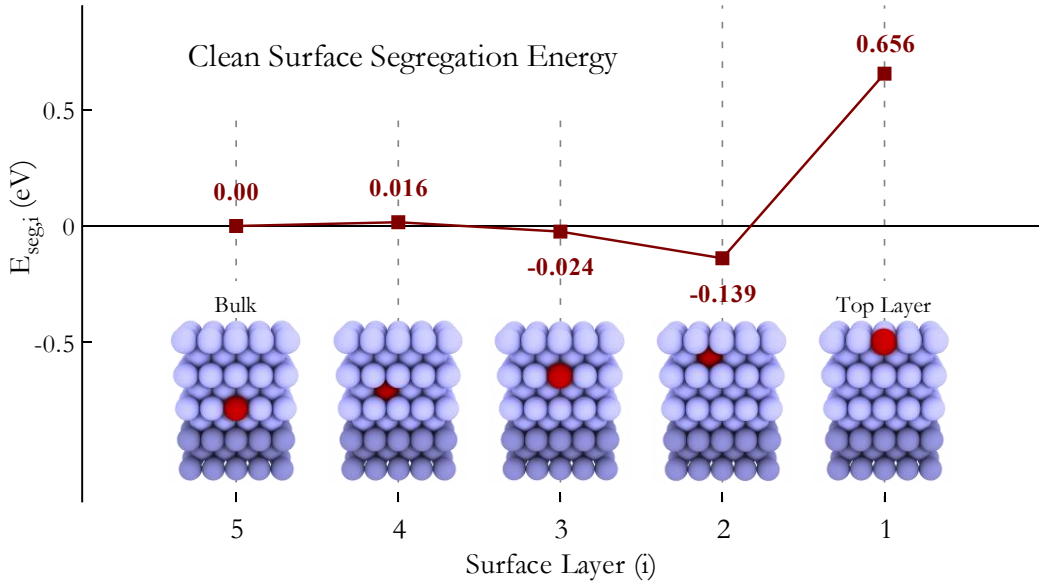


**Figure 5.3.** Calculated segregation energy profile for a single Cr atom in a clean fcc Ni (100) surface covered by only vacuum space. This is the same energy profile presented for the (100) surface in Figure 4.3 (a)**.**

In CHAPTER 4, much of the emphasis and focus was placed on understanding the driving forces behind the oscillatory shape observed in the clean surface profile. In this chapter, we will focus our attention instead on the segregation behavior observed in the first layer, or more specifically the large positive energy and how it will be affected by the addition of salt to the surface. This is done for two reasons: (1) the interaction between the Cr atom and the adsorbed salt species is the most direct and at its strongest when Cr is in the first layer and (2) as will be shown shortly in section 5.3.2, the stability of an isolated adsorbate structure in any one of the specific adsorption sites is uniquely dependent on

forces in the x-y plane (*i.e.*, the surface normal plane) being symmetrically equivalent in all directions. Because of the ABAB stacking of the (100) planes, it is impossible for the x-y forces to remain symmetric for some of the adsorbate structures when the Cr atom is in the second layer. This causes the adsorbate structures to shift and move their position making direct energy comparisons difficult.

### *5.3.1 Surface Energies*

As we learned in CHAPTER 4, the oscillatory segregation behavior in the Ni surface can be attributed to a combination of lattice distortion effects stemming from a significant amount of electron transfer from the Cr to the Ni lattice. The focus of CHAPTER 4 was really on the sub-surface segregation behavior (*i.e.*, the second layer and below) and so a treatment of the first layer behavior was not sought or provided. The reasoning for this was simply that the first layer behavior (*i.e.*, the high positive energy) was largely driven, and dominated, by the relative surface energy differences between Cr and Ni, a segregation phenomenon that has already been widely studied and discussed in literature [103,104,116]. In isolated Ni-Cr surfaces, this always results Ni segregating to the first layer because the surface energy of Ni is almost always lower than that of Cr for nearly every orientation of the surface. In other words, Cr has a much higher aversion than Ni to being in the significantly under-coordinated state in the first layer of a free surface, something which partly traces back to its less filled valence d shell [147].

While the surface energies of Cr and Ni have been calculated before with DFT methods, it is useful to calculate them again here for surfaces corresponding to the exact surface slabs used this study and under the specific simulation parameters of these DFT

calculations. Surface energy calculations require a different type of surface slab than the half-slabs employed in this work, however. For the calculations, a "mirror" slab must be used, in which both ends of the slab are allowed to fully relax, forming a mirror image of one another while the "bulk" behavior is enforced in the center of the slab either by locking the center atomic layer(s) in place there or by increasing the number of atomic layers the Z direction enough so that the slab naturally forms a bulk region (*i.e.*, a true thin-film material).

The necessity of the mirror slab is a consequence of the mathematical description of the surface energy, which corresponds to the work required to create a surface of area $A$ by cleaving a bulk crystal in two. In cleaving the crystal, we are left with two identical surfaces, and so this must be taken into account in the equation and in our simulations, hence the dual surfaces present on either end of the slab. Written in terms of DFT slab energies, the surface energy, $\gamma$, is found according to

$$\gamma = \frac{1}{2A}(E_{slab} - nE_{bulk}) \tag{40}$$

Where $E_{slab}$ is the energy from the slab calculation, $E_{bulk}$ is the energy per atom in the perfect bulk crystal, $n$ is the number of atoms used to construct the surface slab, $A$ is the unit area of the surface within the simulation cell, and the $1/2$ parameter comes from the duel surface formation.

In this work, a mirror slab was first created by modifying the original 9 layer slab into one that was doubled in height (*i.e.*, 17 layers in total) and allowed to fully relax at both ends with only the layer at the very center being locked in place. Three versions of

this new 17 layer mirror slab were then used the calculate surface energy for an fcc Ni (100) surface, an fcc Cr (100) surface and a bcc Cr (100) surface. These are reported in **Table 5.2** along with the experimental Ni and Cr surface energies and both spin-polarized (sp) and non-spin-polarized (non-sp) DFT energies from previous studies.

**Table 5.2.** Aggregation of DFT calculated and experimental surface energies of the low index surfaces in fcc Ni, bcc Cr and fcc Cr. The sp column indicates whether or not spin-polarization (sp) effects were included in the DFT calculation.

| | | | | | **Surface Energy, $\gamma$** | |
|---|---|---|---|---|---|---|
| **System** | **Author/Study** | **Method** | **sp** | **facet** | **eV/Å$^2$** | **J/m$^2$** |
| fcc Ni | De Boer et al. (1988) [209] | Exp | - | - | 0.1436 | 2.300 |
| | Tyson et al. (1977) [151] | Exp | - | - | 0.1469 | 2.354 |
| | This work | DFT | non-sp | 100 | 0.1401 | 2.244 |
| | | DFT | non-sp | 111 | 0.1218 | 1.952 |
| | Vitos et al. (1998) [148] | DFT | non-sp | 100 | 0.1514 | 2.426 |
| | | DFT | non-sp | 111 | 0.1255 | 2.011 |
| | Skriver et al. (1992) [210] | DFT | non-sp | 111 | 0.167 | 2.67 |
| | Alden et al. (1994) [147] | DFT | non-sp | 100 | 0.167 | 2.67 |
| | | DFT | sp | 100 | 0.173 | 2.77 |
| | | DFT | non-sp | 111 | 0.164 | 2.63 |
| | | DFT | sp | 111 | 0.168 | 2.69 |
| fcc Cr | - | Exp | - | - | - | na |
| | This work | DFT | non-sp | 100 | 0.1812 | 2.904 |
| | | DFT | non-sp | 111 | 0.1491 | 2.389 |
| | Skriver et al. (1992) | DFT | non-sp | 111 | 0.193 | 3.09 |
| bcc Cr | De Boer et al. (1988) [209] | Exp | - | - | | 2.450 |
| | Tyson et al. (1977) [151] | Exp | - | - | | 2.380 |
| | This work | DFT | non-sp | 100 | 0.2405 | 3.854 |
| | Vitos et al. (1998) [148] | DFT | non-sp | 100 | 0.1529 | 3.979 |
| | | DFT | non-sp | 111 | 0.2573 | 4.123 |
| | Skriver et al. (1992) [210] | DFT | non-sp | 110 | 0.227 | 3.63 |
| | Alden et al. (1994) [147] | DFT | non-sp | 100 | 0.210 | 3.36 |
| | | DFT | sp | 100 | 0.140 | 2.23 |

From these values, one can see that regardless of whether Cr is in the fcc or bcc crystal configuration, and independent of the specific surface face, or whether the surface is magnetically ordered or not the surface energy of Cr is usually higher than that of Ni. We can also see the effect of spin-polarization on the surface in these calculations. As Alden et al.'s [147] energies show, there is not much effect in the Ni surface when sp effects are turned on, however, in Cr, the inclusion of sp and the magnetic ordering that follows was found to lower the surface energy significantly. This effect comes from the behavior of the electrons in the half-filled d-band and has been observed in other 3d metals in the middle of the periodic row like Co and Mn [211,212]. Alden et al.[147] showed that this effect was specific to the individual surface facet in Cr, and that the degree of the energy difference was related to the level of magnetic saturation possible in each surface facet, hence the differences between the (111) and (100) surfaces in Cr.

As stated before, however, magnetic ordering in Ni-Cr alloy is lost when Cr content is increased to even small concentrations and its suppressed even further by the high-temperatures it should experience during operation in a reactor. By not including sp effects the surface energy of Cr surfaces is increased, which should then cause the segregation energy for Cr in the first layer of Ni increase. This is exactly what was seen in CHAPTER 4 when comparing the calculated non-sp (111) segregation energy profile found with the sp segregation energy profile found by Yu et al.[116] for the same surface (shown in **Figure 4.1**). Even with sp effects, the profile found by Yu et al. essentially showed the same shape and general behavior, just with a slightly lower segregation energy for the first layer, suggesting that the overall effects of sp in this current study are essentially unimportant.

With an understanding in place for the first layer segregation behavior of a clean surface, we can now begin to examine the effects of placing salts on the surface and how their interaction with the Cr might alter the segregation behavior.

### *5.3.2 Single Anion Influenced Segregation*

Molten salts can come in many forms, with many different elemental compositions. These salts generally consist of a halide species (*i.e.*, usually Cl or F) mixed with some other combination a metal species. In bonding, the halide forms the anion and the other metal(s) form the cations of the ionic bonds. In the liquid molten state, however, the anion-cation bonds become very weak and so the anion and cations can loosely be thought of as independent ionized particles floating in an "ionic soup". The structure and ordering of this soup is not totally random, however, as the ions will still feel the influence of strong local ionic forces and coordinate accordingly.

In DFT adsorption studies, it is not computationally feasible to simulate the entirety of this ionic liquid above the surface and so adsorption is usually modelled by placing single or isolated atoms directly onto the surface. This approximation is usually valid because an adsorption interaction is a uniquely local phenomenon, most strongly governed by the direct bond formed between the adatom and the surface. Beyond this, it is not too difficult to account for the more extended local effects by adding additional liquid or adsorption particles just near adsorption site.

In this section, the effects of the adsorbed halides Cl and F, and the salt impurity O, on the segregation behavior of Cr will explored.

#### 5.3.2.1 Adsorption Sites

Every crystal surface possesses unique adsorption sites which the adatoms will usually prefer to sit in. The (100) surface was chosen for this study, in fact, because of the simplicity of its unique sites, of which there are only three. These are the top site, the bridge site, and the hollow site, and they are shown in **Figure 5.4**. These sites are unique because they correspond to positions on the surface where forces in the x-y plane are symmetrically equivalent. Any atom sitting in one of these sites will feel equal forces acting on it from all directions (excluding the surface normal direction) and so will be trapped in place. Visually, or graphically, the top site can be thought of as being on top of a mound or hill, while the bridge site is situated in the center of a saddle point, and the hollow site is located in the bottom of a well.

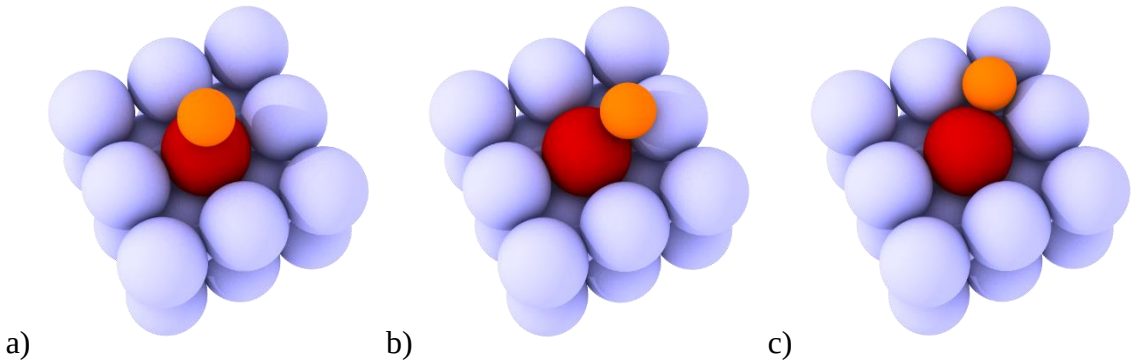


**Figure 5.4.** The three unique adsorption sites of the (100) surface. In these images, the blue atoms represent Ni atoms in the surface, the orange atom is the adatom, and the red atom is the position of the Cr atom in relation to the adatom. Figure a) is called the top site, Figure b) is the bridge site, and figure c) is the hollow site.

Because the top and bridge sites are in positions situated near the tops of slopes, if forces around the site become asymmetric, an isolated adatom can be pushed out of these

sites and into the well site. This behavior does occur in some of the calculations that will presented in the following sections and will be discussed when appropriate.

#### 5.3.2.2 Chlorine Influenced Segregation

The segregation energy profiles of Cr segregating under an adsorbed Cl adatom, situated in each of the three (100) adsorption sites, are shown in **Figure 5.5**. It's immediately clear that the Cl adatom has an effect on segregation. The first layer energies have decreased for each site, with the top site configuration producing the strongest effect and the hollow site having the weakest effect. The second layer energies are not as clear, however, as true energies for the top site and bridge sites were not able to be found, indicate by the black square marker. In these configurations, the adatom was pulled out of the initial site and into the hollow by the off-center Cr atom in the second layer. In the second layer hollow site configuration, however, we see an increase in the segregation energy. This is indicative of the attraction between Cr and Cl relative to the Cr-Ni and Cl-Ni interactions. In this scenario the Cr and Cl atoms are pulling each other strongly, squeezing the layer of Ni atoms between them an increasing the amount of stress in the system.

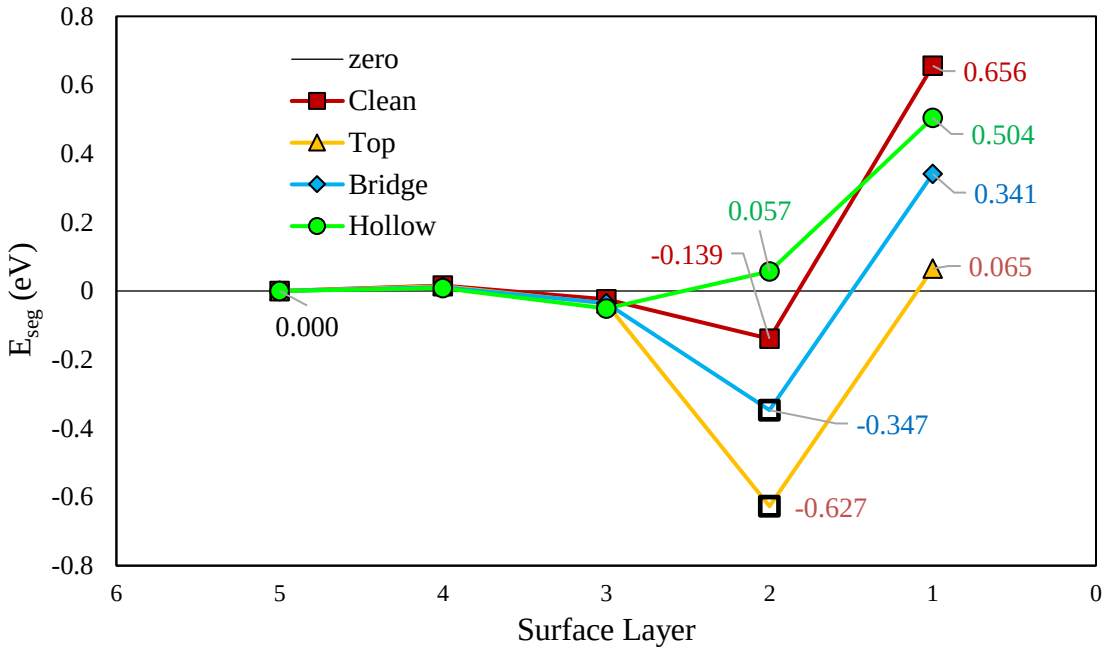


**Figure 5.5.** Calculated Cr segregation energies when a single Cl occupies each adsorption site on the (100) surface. The red line depicts the segregation profile found for Cr under a clean surface. The black square markers for the second layer energies indicate sites that were unstable which resulted in the adatom falling into the hollow site.

### 5.3.2.3 Fluorine Influenced Segregation

Next, we plot the same segregation energy profiles, but this time with F adsorbed to the surface instead of Cl. This is shown in **Figure 5.6**. In this case, F is seen to produce an even greater decrease the first layer energies. Now though, not only have these first layer energies decreased, but they have become negative too. This means a F adatom has the effect of completely reversing the segregation behavior in this surface, making Cr segregation to the top layer now most favorable. There is some difference in the second layer behavior relative to Cl, however, in that the top and bridge site F's remained stable and stationary in their sites. While, the reason they remain stable is difficult to quantify,

the segregation energies that result do seem to support the notion that the Cr-F or Cr-Cl bond interaction is adding stress to the system when the Cr is in the second layer. In this case, the top site, in which the Cr and F are furthest from each other, shows the smallest energy increase while the hollow site, in which the Cr and F are closest to each other, shows the greatest energy increase.

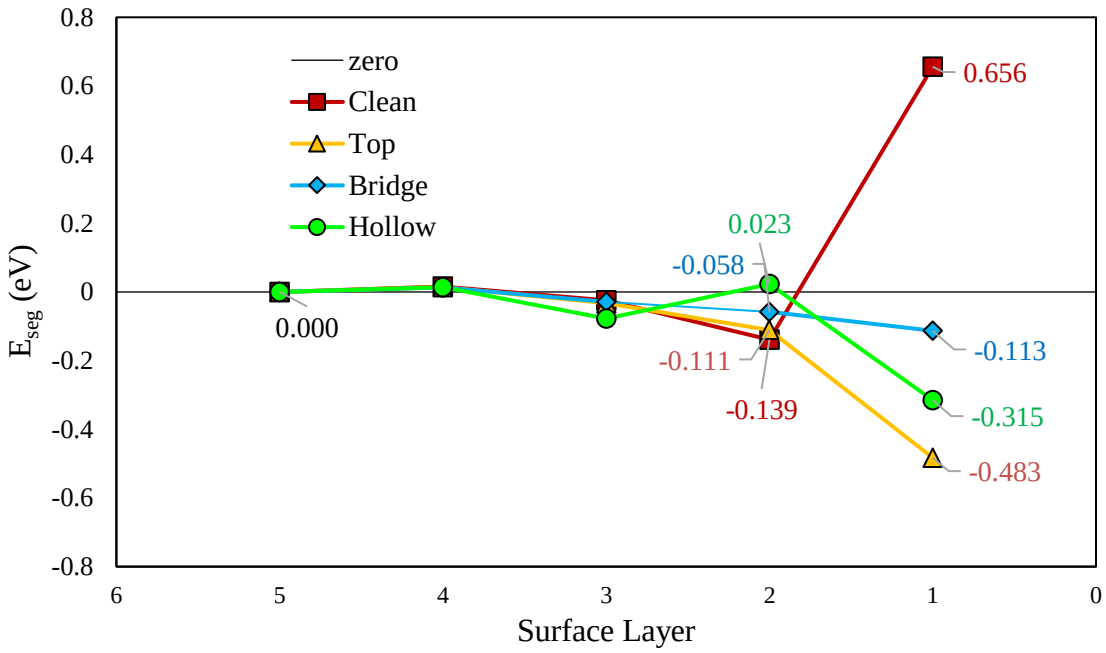


**Figure 5.6.** Calculated Cr segregation energies when a single F occupies each adsorption site on the (100) surface. The red line depicts the segregation profile found for Cr under a clean surface

### 5.3.2.4 Oxygen Influenced Segregation

Finally, the O adatom influenced segregation is shown last, in **Figure 5.7**. Here, the magnitude of the effect the O adatom has on Cr segregation, relative to both Cl and F, is massive. The first layer energies in the top and bridge sites have significantly decreased

very far into the negative, and by far more than the what the Cl or F adatoms were able to produce. This is indicative the strong attractive interaction between Cr and O, which again is also suggested by an increased second layer hollow site energy. Oddly, however, the hollow site energy for the first layer did not decrease like the top and bridge site energies did, which could suggest that O would prefer to bond with fewer atoms at the surface. In the second layer, we again see unstable top and bridge site configurations like what was seen for Cl. This may actually suggest that this effect is related to the size of the adatom and the ability for its interaction to actually reach the Cr atom buried in the second layer. Of the three anions, Cl is by far the biggest, followed by O and then by F. It may be that the range of F's influence is simply not long enough to reach the second layer Cr effectively and so the Cr-F interaction is not strong enough to pull the F out of its adsorption sites.

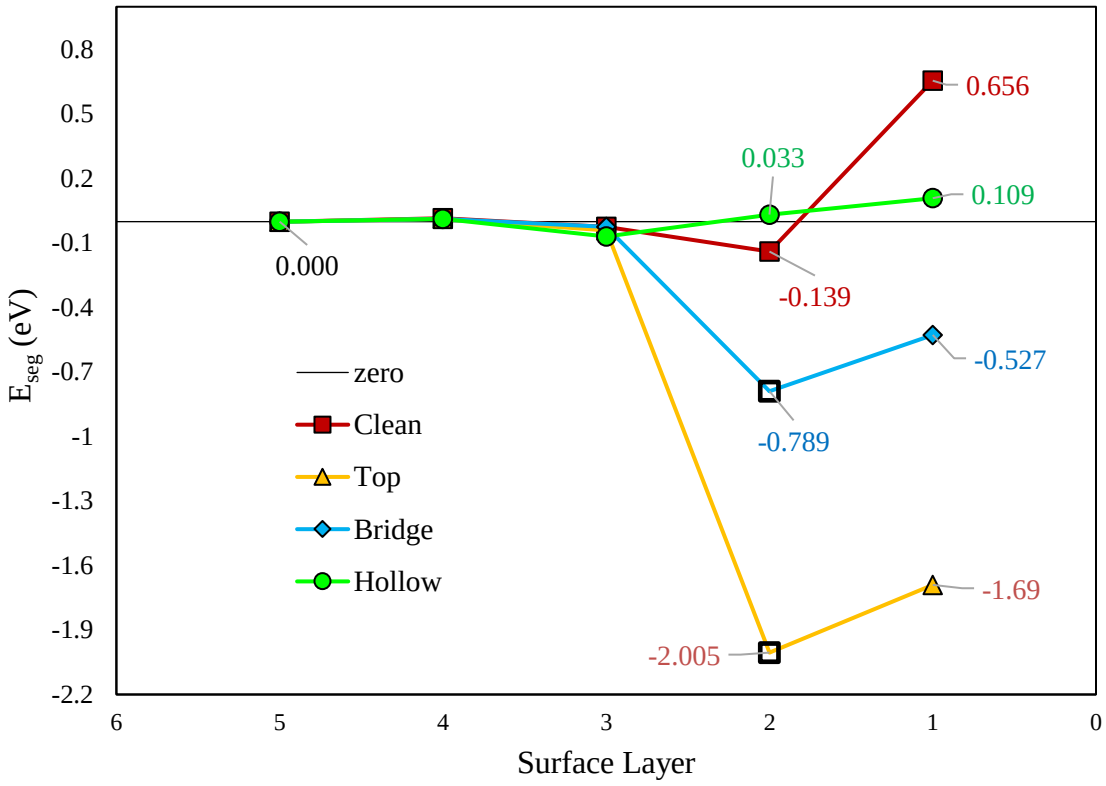


**Figure 5.7.** Calculated Cr segregation energies when a single Cl occupies each adsorption site on the (100) surface. The red line depicts the segregation profile found for Cr under a clean surface. The black square markers for the second layer energies indicate sites that were unstable which resulted in the adatom falling into the hollow site

### *5.3.3 Anion-Cation Influenced Segregation*

The isolated anions were able to impart interesting effects on the segregation behavior in the Ni-Cr surface. Unfortunately, attaching a single F, Cl and O atom to the surface may not be the most ideal method to approximate the molten salt. Atoms in the molten salt are likely to be ionized, with anions carrying an extra electron with them while the cations will likely be missing one or more electrons from their nearly empty valence shell, and so a neutral atom on the surface will not be truly representative. Additionally, salt ions in contact with the surface will not be isolated. Instead they will be surrounded by

countless other salt ions, which will likely have a diverse and rapidly changing influence on the electronic bonding behavior of the adatom.

In order to move the DFT calculations in this work closer to reality, a second set of adsorption influenced segregation calculations was performed with an additional cation species attached to the back of the adsorbed anion. The cations in these simulations were chosen to represent common salt species (*e.g.,* Na and Mg) and a common salt impurity associated with O (*e.g.,* H). The addition of these cations has a duel effect. First, the anion will pull a significant amount of electron density on to itself from the cation, making the anion more characteristic of an actual negatively charged salt ion. Second, the presence of the cation itself brings the entire adsorption model closer to the actual thing. It's still not the ideal scenario, but as more atoms are included in the local environment around the adatom, the model will be able to achieve a greater accuracy.

In performing this second set of simulations, some key changes in the slab configuration and the order of the segregation calculations are made. First, as could be seen in **Figure 5.5** and in **Figure 5.7**, the anion influence does not really extend beyond the second layer. Because of this, and in an effort to save on computational cost, the range of the segregation calculation can be adjusted. Now, instead of traversing the top five layers, the calculations will traverse only the top three layers, with the third layer configuration serving as the new bulk reference state. Because of this change, the height of the slab can now be reduced from 9 layers in total to 6, with only the bottom two layers remaining fixed during relaxation. In accordance with this change, all segregation energies from the previous sections, when cited from here on, will be reported using the third layer of those calculations as the reference state.

A second change included in these anion-cation calculations is that second layer energies are not calculated. As was evident in the single anion calculations, the instability of the adsorbate, with respect to its position, was a problem and prevented a valid comparison and analysis of the second layer energies. With the addition of the cation to the simulation, the structure of the adsorbate becomes far more complex and it is easy to see how these new structures would distort and shift when pushed by the asymmetry of the of the second layer Cr position. Because of this, energies are now only calculated for the Cr when it is in the third and first layers.

#### 5.3.3.1 Adsorption Configurations

Because of the relative ease at which isolated surface adsorbates are distorted by the surface, and because we are solely interested in the Cr/Ni-anion-cation chain interaction only two adsorbate configurations were able to be used in these simulations. These configurations, which are shown in **Figure 5.8**, have been named the top-straight configuration and the bridge-angled configuration. In this naming convention, the word before the hyphen indicates the specific adsorption site of the base anion (*i.e.*, either in the top or bridge site) and the word after the hyphen indicates the direction or orientation of the anion-cation chain. In this case, the straight orientation describes a pole like structure sticking straight out from the surface, while the angled description indicates that the anion-cation pole is oriented at an angle from the surface. As will be seen, neither of these configurations was stable for every anion-cation combination.

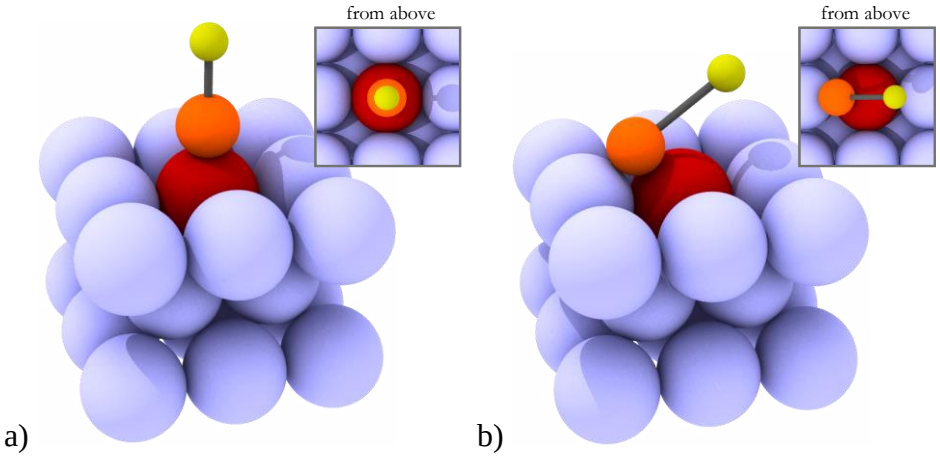


**Figure 5.8.** Anion-cation configurations used in this work. The left configuration (a) is the top-straight configuration, in which the anion (orange atom) is in the top site above the Cr (red atom) and the cation (yellow atom) is oriented directly above it. The right configuration (b) is the bridge-angled configuration, in which the anion is in the bridge position and the cation is oriented above it at an angle so as maintain the symmetry of forces needed to keep the structure locked in the bridge position.

An anion-cation structure based out of the hollow site was not included in these calculations for two reasons: (i) although it was technically the most "stable" of the three adsorbate sites in this work, hence the propensity for the other adatoms to shift into it, this behavior is expected to change when surface coverage increases (*i.e.*, when the rest of the salt atoms also interacting with the surface are considered) and (ii) when the anion is in the well site, the entire adsorbate structure sits low enough in the surface that the cations begin to interact with the nearby Ni atoms in the first layer. While this interaction might technically be interesting int itself, it is not in the scope or goal of this current investigation. It is important to be sure that we are only modeling and comparing the isolated set of interactions that take place within the Cr-anion-cation chain, or within the Ni-anion-cation chain when the Cr is in the third layer.

Each anion-cation pair (Cl, F, O – Na, Mg, H) is modelled using both of the absorbate configurations just described. All of the combinations modelled in this work are listed in Table 5.3.

**Table 5.3.** All anion and anion-cation pairs modelled in this work.

| Anion\Cation | - | Na | Mg | H |
|---|---|---|---|---|
| Cl | Cl | NaCl | MgCl | HCl |
| F | F | NaF | MgF | HF |
| O | O | NaO | MgO | HO |

5.3.3.2 Chlorine-Cation Influenced Segregation

The Cl-cation pair segregation energies are shown first in **Figure 5.9**. Again, recall these energies correspond to the energy difference between the configuration with Cr in the third layer and the configuration with Cr in the first layer. It's quite clear the cations provide something of a nullifying effect on the of the strength of the anion's influence on Cr segregation. In every case, the first layer segregation has increased relative to the single anion configuration. Mg seems to have the strongest effect in this reversing behavior, almost returning causing the energy to return to original level, in the clean surface.

One should also see that in **Figure 5.9**, a segregation energy is not reported for the H-Cl top-straight configuration. It was found that for H-Cl, and H-F as we will see in the next section, the top-straight configuration was unstable above the Ni-Cr surface. In these scenarios, the H-Cl and H-F molecules preferred to bond tightly to one another, and in doing so would break their bond with the surface and move up into the void of the vacuum.

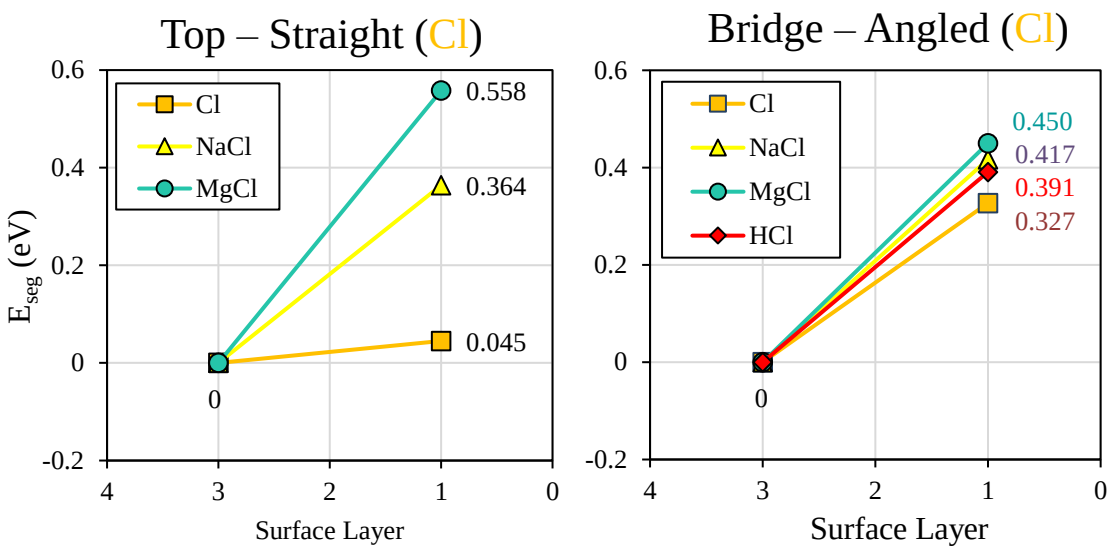


**Figure 5.9**. (Left) the segregation energies found for the Cl-cation pairs in the top-straight configuration. The H-Cl configuration was unstable and so is not shown. (Right) the segregation energies found for the Cl-cation pairs in the bridge-angled configuration.

#### 5.3.3.3 Fluorine -Cation Influenced Segregation

The calculated segregation energies for the fluorine-cation configurations are shown next in **Figure 5.10**. We see a very similar effect here with the addition of the cation causing the first layer energies to go back up closer to their original clean surface level. While the energies are overall lower than those of the Cl-cation configurations, the F-cation first layer energies do rise enough to suggest the nullification effect might still be enough to prevent the strong influence of the F anion from significantly affecting overall segregation behaviors.

As mentioned in the previous section, the H-F configuration was found to be unstable in these simulations, and so an energy line is not reported. We can also see

something similar happening in the bridge-angled configuration here as well. This time, however, the F-cation molecule does not move away from the surface, but instead shifts its base position from the bridge site to the top site, while maintaining its angled orientation. Following the same naming convention used earlier, this shift, which only occurs for the Mg-F and Na-F pairs, results in a structure which could be called a top-angled configuration. The cause for this shift may be related to the electronegativity of F, which is higher than that of O and Cl, and so when F is within the effective interaction distance of a negatively charged ion like the ionized Cr in these surfaces, the strength of the bond formed between them may be great enough to pull F into the top site. Separate segregation energy lines are calculated for these two structures and are reported in **Figure 5.11**. These energies were calculated using a new third layer reference structure (*i.e.,* Cr in third layer) which mimicked the top-angled position of the of the molecule. In this graph, the single F anion line corresponds to the top site configuration energy. Expectedly, we see a very similar behavior between the top-straight and top-angled configurations.

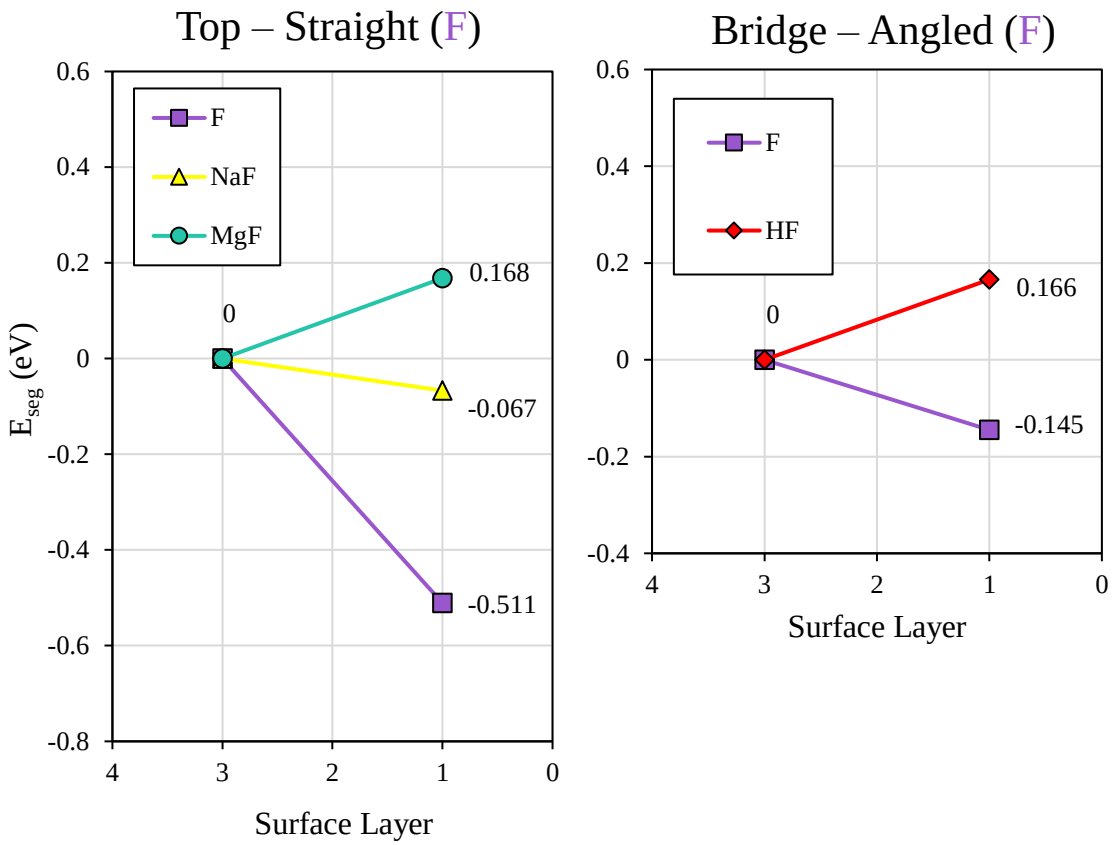


**Figure 5.10.** (Left) the segregation energies found for the F-cation pairs in the top-straight configuration. The H-F configuration was unstable and so is not shown. (Right) the segregation energies found for the F-cation pairs in the bridge-angled configuration. The MgF and NaF bride-angled configuration were unstable with respect to a top-angled shift and so not shown.

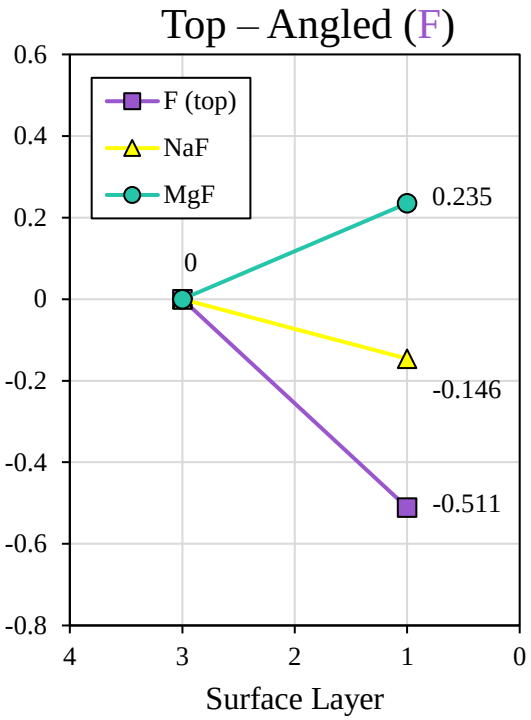


**Figure 5.11.** The calculated segregation energies of MgF and NaF in the top-angled configurations. This structure was formed when the MgF and NaF molecules, originally placed in the bridge-angled configuration, shifted into the top position over the Cr.

#### 5.3.3.4 Oxygen-Cation Influenced Segregation

Finally, the O-cation segregation energies are reported in **Figure 5.12**. With O as the base anion, every pair anion-cation combination for both of the primary adsorption configurations was stable. These calculated O-cation segregation energies represent, perhaps, the most interesting results in this section. As can be seen, the nullifying effect is still present for O-cation pairs, however, in each case, the effect of the O anion influence was so strong that the first layer segregation energies still remain significantly in the negative. This suggests that O, a salt impurity, is far more likely to be involved in the

processes that result in Cr being brought to and eventually removed from the surface, than the natural salt components, F and Cl. This is in excellent agreement with the analysis provided by Raiman et al [135], which showed that the purity of the salt had by far the strongest correlation with overall corrosion rates in molten salt systems.

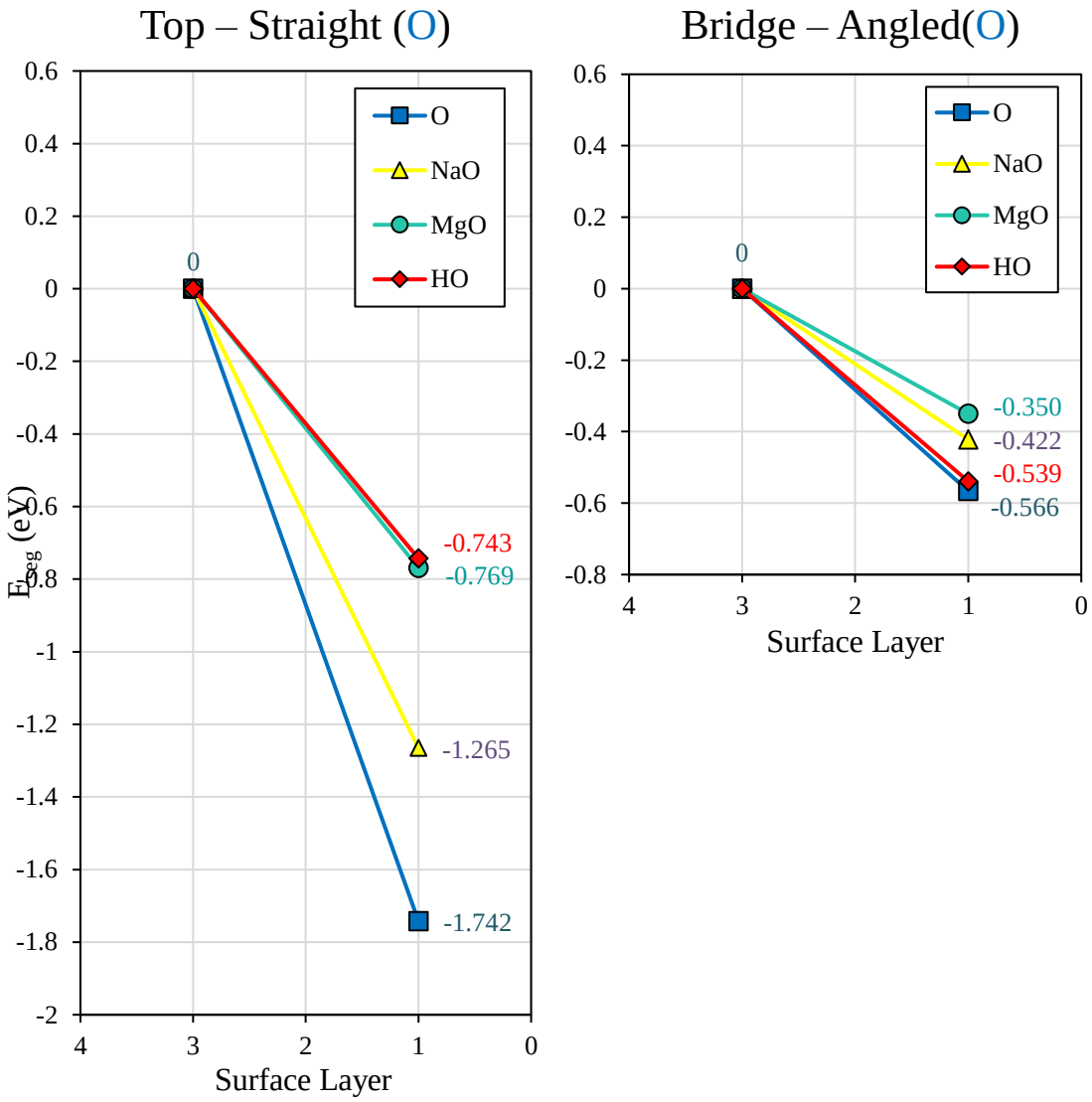


**Figure 5.12.** (Left) the segregation energies calculated for the O-cation pairs in the top-straight configuration. (Right) the segregation energies calculated for the O-cation pairs in the bridge-angled configuration.

### *5.3.4 Charge Transfer During the Adsorption-Segregation Interaction*

We have now seen that Cl, F, and O anions each influence the segregation behavior in these systems in a way that promotes Cr segregation in the first atomic surface layer.

We have also seen, though, that the presence of a single cation near the adsorbed anion reduces the relative strength of this effect, and that for Cl and F, this reduction is enough effectively nullify the effects of the halide anions.

In order to understand why this happens we can look at the charge of the atoms and the transfer of electrons occurring in these local interactions. Just as in Chapter 4, the Bader charge counting method is used to count the charge in each atomic volume [122–125]. In the following sections, the electronic charge transfer behaviors exhibited by these adatom configurations will be presented and discussed according to the most significant configurational trends.

#### 5.3.4.1 Top and Bridge Site Electron Transfer

The charge transfer in the single anion top and bridge site configurations are shown first, in **Figure 5.13** and in **Figure 5.14**, respectively. In every configuration, it's clear that the adatom is stripping electron charge from the Cr. If we relate the degree of this electron transfer between the Cr atom and the anion adatom, then we can that there is a remarkable degree of correlation with the first layer segregation energies. In both the top and bridge sites, the Cl adatom has the weakest effect, pulling the smallest amount of charge, while the O has the strongest effect, pulling the most charge of the Cr.

We can also see the adatoms are able to pull the Cr upwards, slightly out of the surface. The magnitude of the Cr atoms upward displacement also seems to be proportional to both the level of charge transfer and the segregation energy of the first layer with the Cl atom have the weakest effect and the O atom having the greatest effect.

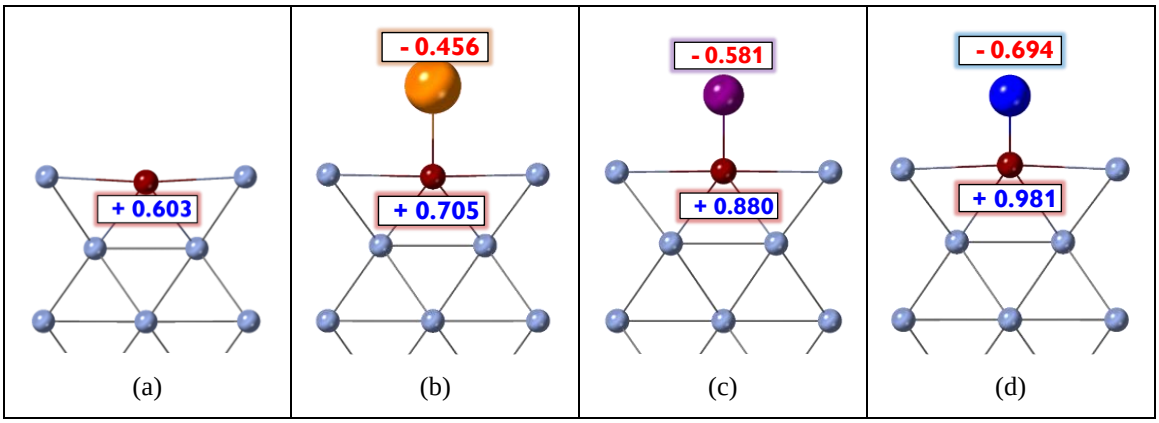


**Figure 5.13.** Atomic charge states of the single anion in the top site configuration when the Cr atom (maroon) is in the first layer. The clean surface is shown in (a), the Cl (orange) adatom in (b), the F (purple) adatom in (c) and the O (blue) adatom in (d). The atomic charge of each atom is indicated by the number in the box nearest the atom. A blue number indicates electron loss (*i.e.*, positive charge) and a red number indicates electron gain (*i.e.*, negative charge).

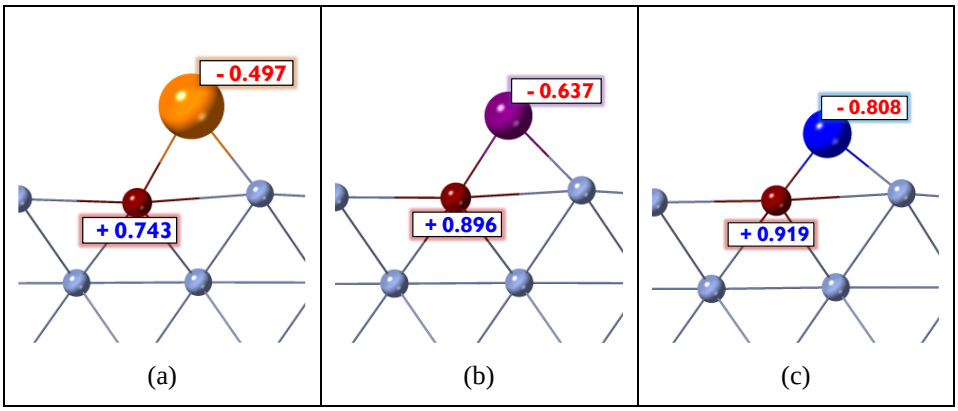


**Figure 5.14.** Atomic charge states of the single anion in the bridge site configuration when the Cr atom (maroon) is in the first layer. The Cl (orange) adatom is shown in (a), the F (purple) adatom in (b), and the O (blue) adatom in (c).

#### 5.3.4.2 Top-Straight Electron Transfer

Next, we turn our attention to the anion-cation pair configurations. Recall that the cations had the effect of reducing the strength of the anions' influence on segregation. If

the first layer segregation energies are truly correlated to the degree of charge transfer between Cr and adatom, then we should see this same effect in the charge transfer behavior when we bond cations to simulation. In fact, this is exactly what we see happen in both for the types of pair configurations.

Examining first the charge transfer in the top-straight configurations, shown in **Figure 5.15** and **Figure 5.16** just a few representative systems, the effect of the cation is clear. In every case, the positive charge on the Cr atom has been reduced slightly, relative to its charge in the single anion configuration. The anion is instead taking on a significant amount of charge from the cation, reducing its ability to take electrons from the Cr. If we think about this in relation to the anion valence shell, we can begin to draw a strong connection between of charge transfer and the relative reductions seen in the halides versus the oxygen atom. The valence structures of Cl and F are each one electron short of a full valence, while O's valence is two electrons short. In a charge transfer interaction, we can think of this as meaning O is capable of taking on more electrons than either Cl or F. This could be the reason the O's effect on segregation remains strong in the presence of a cation when Cl and F's effects do not. When a cation bonds with one of the halides it imparts a significant amount of electron charge on the halide, effectively filling the empty hole in its valence, and making it less able take charge from the Cr. When a cation bonds with the O, however, a similar amount of charge transfer occurs which does to an extent lessen the O's ability to take charge from the Cr, but in this case the O has additional space left in unoccupied in its valence, allowing to still interact strongly with the Cr.

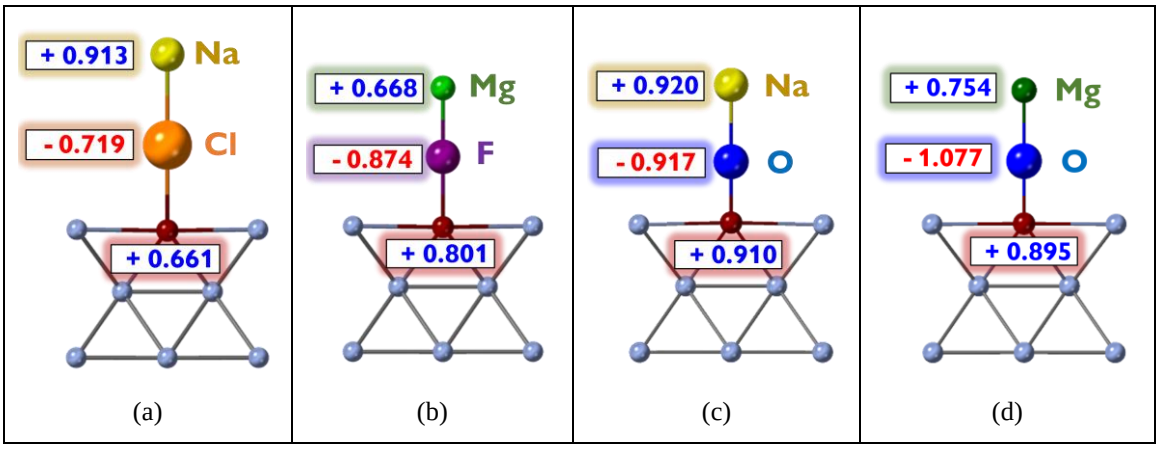


**Figure 5.15** Atomic charge states of the top-straight anion-cation configurations when Cr (maroon) is in the first Ni (light blue) layer. Individual anion and cation types are denoted by color and label. A negative red charge means electrons were gained and a positive blue number means electrons were lost.

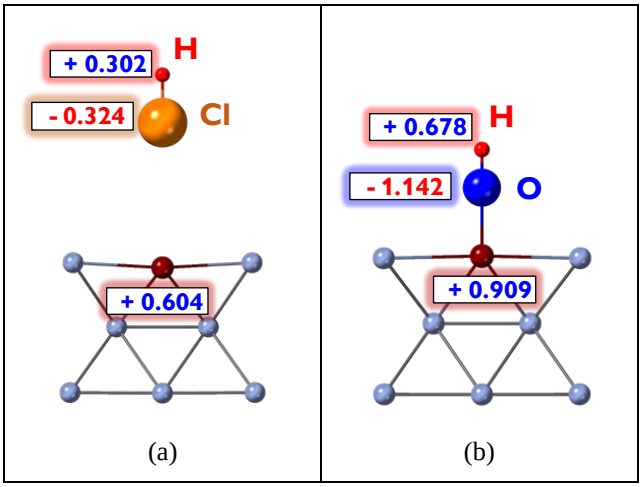


**Figure 5.16.** Atomic charge states of representative top-straight anion-H configurations when Cr (maroon) is in the first Ni (light blue) layer. In figure (a), the H-Cl molecule has drifted away from the surface during relaxation. This was also observed for H-F.

We can also similarly relate these behaviors to the electronegativities of the Cl, F, and O atoms. Each of these anions is highly electronegative with F having the strongest electronegativity (3.98), O the next strongest (3.44) and Cl being the least strong (3.16). In

every type of interaction analyzed in this study, Cl generally had the weakest effect, F the next strong effect, and O the strongest effect. This at first doesn't match up, but if we take into account the O's greater capacity to take on additional electrons then we can begin to see a correlation. F has the strongest pull on electrons but it only has room for one extra electron in its valence, hence why it always has stronger influence than Cl, which has the same amount of room in its valence. O's pull is not as strong as F's pull, but it can fit more stolen electron charge in its valence before its electronegative attraction is screened.

#### 5.3.4.3 Bridge-Angled Cation Behaviors

If this combination of electronegative strength and valance shell occupation is behind the segregation behavior seen in these calculations, then we should see this same effect in the Bridge-Angled configuration calculations. The discussion of which is divided and presented in the following sections according to the cation species. This distinction is made because each cation behaved in its own distinct manner.

As will be shown in each cation section, the height (or angle) of the cation seemed to depend on the specific type of cation. The position of the relaxed Na atom was always high and away from the surface, the Mg atoms preferred to sit nearly flush with the anion, and the H atoms always sat low and below the height of the anion.

#### 5.3.4.4 Sodium (Na) Behavior

The charge transfer and relaxed positions of the Na configurations are shown in **Figure 5.17**. At first glance, the electron transfer in these surfaces appears to break our theory connecting the charge transfer to segregation energy as the F now shows the highest

level of charge transfer, instead of O. Recall, however, that the Na-F molecule shifted out of the bridge-angled configuration and into the top-angled configuration. With the anion now positioned over the top site, it is more appropriate to compare the charge transfer of the angled Na-F molecule with other molecules also positioned in the top site (*i.e.*, those in **Figure 5.15** {above}), as opposed to molecules positioned over the bridge site. In doing so, we can see that the amount of charge transfer in the top-angled Na-F molecule is still less than the corresponding O configurations and the theory presented in second XX still holds.

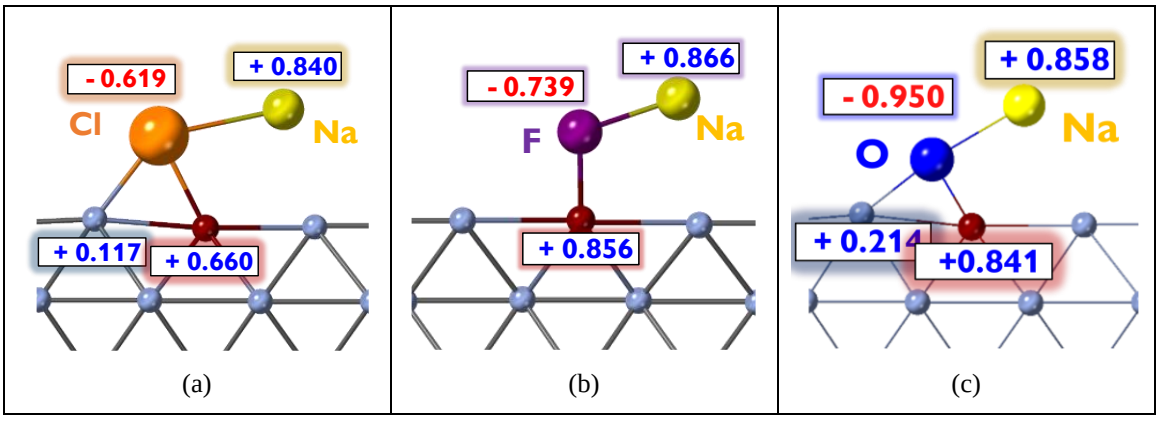


**Figure 5.17.** Atomic charge states of the angled anion-Na configurations when Cr (maroon) is in the first Ni (light blue) layer. Individual anion and cation types are denoted by color and label. A negative red charge means electrons were gained and a positive blue number means electrons were lost.

5.3.4.5 Magnesium (Mg) Behavior

The charge transfer and relaxed positions of the Mg based bridge-angled configurations are shown in **Figure 5.18**. The Mg-F molecule here has also shifted into the top-angled configuration resulting in greater charge transfer than in the bridge site

structures in (a) and (c), but again the magnitude of charge transfer in the top-angled Mg-F molecule is less than in the top-straight Mg-O molecule.

Interestingly, as previously mentioned the Mg atom has shifted closer the surface relative to the Na atom. In doing so it has imparted some charge onto the nearest Ni atom. Despite this, the Cr-anion-Mg interaction does not seem to be affected too much by this additional interaction.

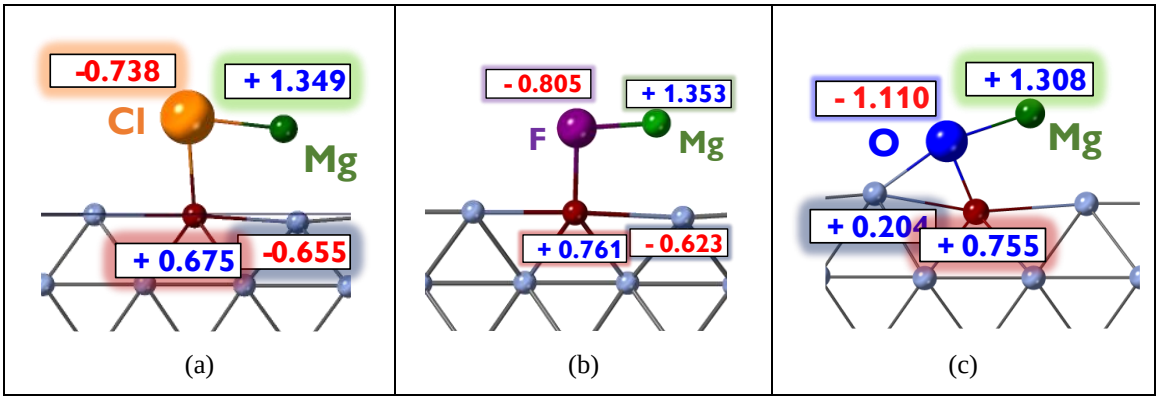


**Figure 5.18.** Atomic charge states of the angled anion-Mg configurations when Cr (maroon) is in the first Ni (light blue) layer. Individual anion and cation types are denoted by color and label. A negative red charge means electrons were gained and a positive blue number means electrons were lost.

5.3.4.6 Hydrogen (H) Behavior

The charge transfer and relaxation positions of the H containing molecules are shown last in **Figure 5.19**. Here the H-F molecule maintains its bridge-angled position, and the magnitudes of the charge transfer through each anion matches the previously observed trend, with O showing the greatest effect. These configurations are unique, however, in that the H atom appears to be interacting directly with both the Cr and the

anion. The H-Cr interaction seems to be interfering with and weakening the Cr-anion interaction, as suggested by the lower overall charges on the anions. The Cr is still able to achieve a high positive charge, however, by transferring some of its charge to the H atom. In fact, these configurations resulted the greatest positive charge around the Cr atom in any of the calculations, with more than entire electron's worth of charge being lost in the case of H-O.

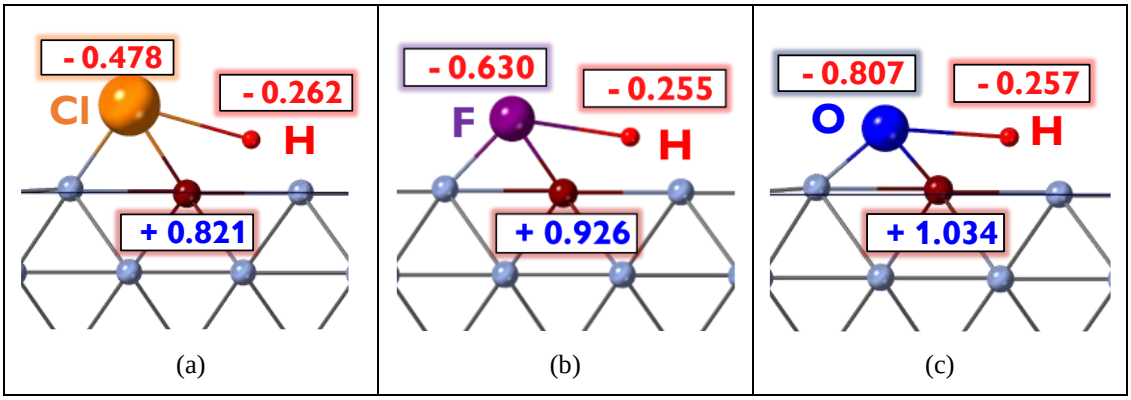


**Figure 5.19.** Atomic charge states of the angled anion-H configurations when Cr (maroon) is in the first Ni (light blue) layer. Individual anion and cation types are denoted by color and label. A negative red charge means electrons were gained and a positive blue number means electrons were lost.

### *5.3.5 Relation to Corrosion Mechanisms*

The results shown here paint a picture of ionic-like charge driven interactions governing the corrosion and segregation related phenomena at the alloy surface/salt interfaces. As was hypothesized in CHAPTER 4, the electronic charge transfer that found to occur between Cr and Ni results in localized pockets of positively charged regions embedded in the surface that might then interact more strongly with the ionically charged species floating by in the molten salt then the rest of the more neutrally charged Ni atom in the surface. The strength of interaction, if measured in terms of adsorbate bonding

distances, charge transfer screening, and effects on segregation were strongest for the most electronegative salt species, and those which could facilitate the greatest movement of electron density. In this way, O showed by far the strongest effect, having a high electronegativity and two open valance orbitals to store the stolen electron charge. This suggests O and other like contaminants in the salt may contribute most strongly to overall corrosion. While Cl and F adsorption both showed Cr segregation promoting effects, their more filled valence, relative to O, meant that charge transfer effects were limited in terms of the magnitude of electron transfer, regardless of the strength of the electron attraction (*i.e.*, electronegativity), and that the damping from nearby cations was more effective.

In the aim of reducing overall corrosion rates in molten salt systems, the development of quick and economically efficient methods of salt purification, in addition to the development of alloys that limit the Ni-Cr charge transfer interaction might pay dividends to the development of economically viable molten salt reactors, concentrated solar power plants, and other high-temperature molten salt based systems.

### *5.3.6 Charge Data for Every Cation-Anion Configuration*

A summary of all the atomic charge states (of interest) of all modelled configurations is listed in **Table 5.4**. Charges are included both for configurations in which the Cr is in the first a layer and for the configurations with Cr in the third layer. In these third layer configurations, the Cr atom charge is nearly identical for every configuration and so is uninteresting. Instead the charge of the Ni atom (or atoms in the bridge site) directly below the anion is reported.

**Table 5.4.** Atomic charge states of all adsorption configurations modelled in this work. Shown are charges for only the atoms relevant to the adsorption-segregation calculation.

**Chlorine**

| | | Cl | | Na-Cl | | Mg-Cl | | H-Cl | |
|---|---|---|---|---|---|---|---|---|---|
| | | Top | Bridge | TS | BA | TS | BA | TS * | BA |
| 1st layer | cation | | | 0.9130 | 0.8398 | 0.5858 | 1.3490 | *0.3026* | -0.2622 |
| | Cl | -0.4557 | -0.4970 | -0.7225 | -0.6190 | -0.7575 | -0.7381 | *-0.3237* | -0.4777 |
| | Cr | 0.7052 | 0.7425 | 0.6661 | 0.6606 | 0.7192 | 0.6748 | *0.6035* | 0.8207 |
| 3rd layer | cation | | | 0.8953 | 0.8441 | 0.6433 | 1.4083 | *0.3040* | -0.1569 |
| | Cl | -0.4553 | -0.4572 | -0.7254 | -0.5856 | -0.7579 | -0.7189 | *-0.3303* | -0.4601 |
| | Ni | 0.1650 | 0.1616 | 0.1714 | 0.1208 | 0.1601 | -0.2587 | *-0.0039* | 0.1884 |

**Fluorine**

| | | F | | Na-F | | Mg-F | | H-F | |
|---|---|---|---|---|---|---|---|---|---|
| | | Top | Bridge | TS | **TA** | TS | **TA** | TS * | BA |
| 1st layer | cation | | | 0.9310 | 0.8656 | 0.6682 | 1.3528 | *0.7373* | -0.2554 |
| | F | -0.5810 | -0.6369 | -0.7834 | -0.7390 | -0.8735 | -0.8049 | *-0.7661* | -0.6289 |
| | Cr | 0.8798 | 0.8961 | 0.8175 | 0.8560 | 0.8008 | 0.7613 | *0.6733* | 0.9256 |
| 3rd layer | cation | | | 0.9251 | 0.8664 | 0.7532 | 1.3291 | *0.7734* | -0.1981 |
| | F | -0.6283 | -0.6431 | -0.7725 | -0.7408 | -0.8532 | -0.1117 | *-0.7970* | -0.6472 |
| | Ni | 0.3394 | 0.2553 | 0.2670 | 0.0998 | 0.2430 | 0.0123 | *0.0401* | 0.3455 |

**Oxygen**

| | | O | | Na-O | | Mg-O | | H-O | |
|---|---|---|---|---|---|---|---|---|---|
| | | Top | Bridge | TS | BA | TS | BA | TS | BA |
| 1st layer | cation | | | 0.9199 | 0.8575 | 0.7539 | 1.3088 | 0.6772 | -0.2570 |
| | O | -0.6936 | -0.8075 | -0.9169 | -0.9503 | -1.0765 | -1.1103 | -1.1425 | -0.8073 |
| | Cr | 0.9812 | 0.9191 | 0.9095 | 0.8412 | 0.8947 | 0.7553 | 0.9093 | 1.0343 |
| 3rd layer | cation | | | 0.9090 | 0.8663 | 0.8959 | 1.3291 | 0.6379 | -0.1888 |
| | O | -0.6283 | -0.7583 | -0.9486 | -0.9445 | -1.2066 | -1.1117 | -1.1844 | -0.7599 |
| | Ni | 0.2847 | 0.3234 | 0.2800 | 0.1962 | 0.3314 | 0.0123 | 0.3603 | 0.3966 |

* These H-Cl and H-F molecules moved away from the surface

TS = Top-Straight, TA = Top-Angled, BA = Bridge-Angled

## 5.4 Conclusion

In this study, the effects of salt anion and cation species on the segregation behavior of Cr in Ni-Cr alloy was investigated using DFT. Segregation energies were calculated for Cr in a (100) Ni surface covered by single anion salt species (Cl, F, and O) and then again

by anion-cation (Na, Mg, H) molecule species, where the O and H species represent salt impurities. It was found that single adsorbed anions had the effect of significantly reducing first layer segregation energies, promoting the segregation of Cr at the surface. Conversely, cations bonded to the adsorbed anions had the effect of raising the segregation energies back up, essentially nullifying the effects of Cl and F, but not O.

The cause of this behavior was found to be closely related the amount of charge transfer occurring between the Cr atom and the adsorbed species. The anions effectively stripped the Cr atom, which had already been partially ionized by the Ni lattice, of further electron charge. The addition of the cations was found to hinder and reduce the amount of charge that the anion was able to take from the Cr. The subsequent changes to the segregation energy appear to be proportional to the atomic charge state of the first layer Cr atom and the amount of charge transfer between it and the adsorbed anion.

Of the anions, the O produced by far the strongest effects, followed by F and then by Cl. This behavior appeared to be connected to each anion's ability to take electron charge from the Cr, which is related to both the strength of the anion's pull on electrons (*i.e.,* its electronegativity) and its capacity to take on additional electron charge (*i.e.,* its valence shell). In terms of the cations' influence, Mg was found to have the strongest reducing effect on the Cr-anion interaction, with H and Na showing varied behaviors.

The DFT results in this work suggest that salt impurities have a much stronger effect than standard salt species on the Cr segregation behaviors in Ni-Cr alloy surfaces. While the halides may individually want to interact with surface Cr atoms, the other species in the salt, assuming they are in sufficient quantity, should suppress this interaction. It's

important to remember, however, that in these simulations, only small and local interactions can be accounted for. It is difficult to predict how these behaviors might evolve or change when these isolated adsorption structures become surrounded by the rest of the molten salt ions at a realistic density. Experimental investigation of these surface behaviors is thus needed, in addition to the development of higher order computational models which can replicate these local electronically driven interactions while accounting for appreciably larger system sizes and microscopic behaviors.

# CHAPTER 6. ATOMIC ORDERING IN URANIUM-ZIRCONIUM METALLIC FUELS

Uranium-rich U-Zr alloys have been identified as a promising metallic fuel for use in generation IV fast reactors. Metallic fuels have been of interest for use in fast nuclear reactors since the Clementine reactor was first built in 1949 and demonstrated the potential for a larger breeder reactor fueled by a metallic actinide alloy. Metallic fuels have since been used in the experimental breeder reactors EBR-I (1951-1964) and EBR-II (1961-1994), built at Argonne National Laboratory, and in a handful of other experimental and commercial fast reactors built around the same time such as the Dounreay Fast Reactor (DFR, 1959-1977) in Scotland and the Fermi 1 reactor (1963-1972) in Michigan [26,213].

Metallic fuels offer several advantages over the ceramic based fuels currently employed in most commercial reactors. This includes higher thermal conductivities, simpler processing and fabrication techniques, easier fuel recycling, higher burnups, and the potential for improved neutronics [213,214]. Metallic fuels could also allow for low-enriched uranium (LEU) fuel designs in accordance with the Department of Energy's Global Threat Reduction Initiative (GTRI) and could offer passive safety features during reactor transient events [215].

Metallic fuels are not without their disadvantages, however, as undesirable volume-changing phase transformations and fuel redistributions can occur during temperature changes. U metal, for example, undergoes transformations from its groundstate orthorhombic α phase to a tetragonal β phase at 667.7°C± 1.3°C, then to a body-centered

cubic (bcc) γ phase at 774.8°C ± 1.6°C, before melting at 1132.8°C ± 0.8°C [216]. Not only do the low overall melting temperatures pose an inherent risk, but the integrity of fuel cladding and other structural components is also threatened by the anisotropic thermal expansions in the α and β phases that would accompany potential transformations associated with these phases.

### *6.1.1 U-Zr Alloy*

Alloying uranium with other transition metals often serves to negate some of the potential drawbacks of an all-metal fuel. One of the more promising transition metals being considered for U alloy fuels is zirconium, a material already widely used in the nuclear industry because of its excellent high temperature phase stability, high melting temperatures (1,855°C), very low thermal neutron absorption cross-section and relatively low costs. When alloyed with U, Zr acts to stabilize the high-temperature bcc γ phase, a phase ideal for reactor operating conditions, by lowering the α → β transition temperature and increasing the overall melting temperature [217].

In off-normal temperature conditions, however, such as during the starting up or the cooling down of a reactor, it may be possible for phase transformations to occur in the U-Zr metal as temperatures cross the α ↔ β phase boundary. During these transient events, the occurrence of phase decomposition can result in a number of fairly complex microstructures usually depending on the Zr concentration, initial phase structure, and the rapidity of cooling [218–220]. Phase decomposition in the in the initially single-phase bcc U-rich U-Zr alloys envisioned for these nuclear fuels can result in lamellar or acicular multi-phase microstructures consisting of the orthorhombic α phase and a hexagonal δ-U-

$Zr_2$ intermetallic phase [221,222]. Transformations such as these can easily result in a redistribution of fissile U atoms, which can negatively affect reactor neutronics and fuel lifetimes. Therefore, it is of high importance to fully understand both the thermodynamics of the $\gamma \rightarrow \alpha + \delta$ decomposition and the atomic ordering and structure of the product α and δ phases.

The γ- and α-U-Zr phases have already received an extensive amount focus and are well understood from both an experimental and computational perspective [221,223–237] The intermetallic δ phase has been far less studied, however, and as such, there are some discrepancies in what is understood about its solubility and structural characteristics. There was initially some debate over the general stability of the δ phase and it was actually thought to be only metastable [238–240] but Rough *et al*. [218] was able to confirm its stability using X-ray techniques and showed that the previously reported instability in the phase was due to oxygen contamination. There is still some uncertainty, however, on the bounds of the solubility region [241,242]. Ogawa *et al*. [243] has suggested that the δ phase may be so sensitive to oxygen and nitrogen destabilization that efforts to determine the true solubility range are just too difficult.

### *6.1.2 U ordering in δ-U-$Zr_2$*

The atomic structure of the δ phase has been studied with both X-ray diffraction [244,245] and high-resolution neutron diffraction [246] methods and is believed to exhibit a modified partially-ordered C32 ($AlB_2$-type) structure with a P6/mmm space group (or $P\bar{3}m1$ if the B-sites are separable). In reference to the prototype $AlB_2$ structure, which is shown in **Figure 6.1**. the Zr atoms in the δ-U-$Zr_2$ structure would sit in the Al-site at the

corner positions (0, 0, 0) of the hexagonal unit cell and a random mixture of U and Zr atoms would inhabit the two B-sites located in the interior of the unit cell at the (2/3, 1/3, 1/2) and (1/3, 2/3, 1/2) positions. This same structure has been observed in several other U based alloys including $U_3Si_5$, UHf, $U_2Ti$, $U_2Ti_{0.082}Zr_{0.18}$, and $UHg_2$ [218,245–251].

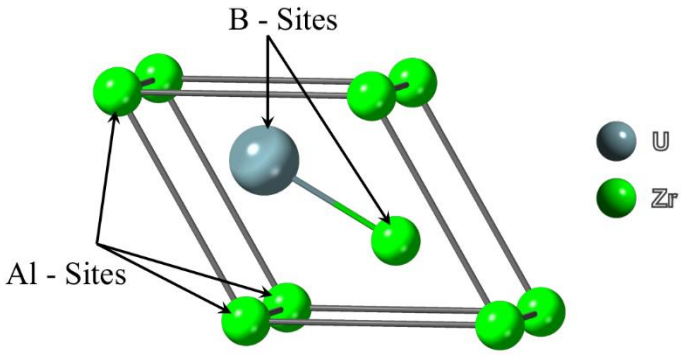


**Figure 6.1**. Atomic structure of the hexagonal δ-U-$Zr_2$ phase. The green atoms correspond to Zr atoms and the blue-grey atoms represent the U atoms.

While the atomic lattice structure is generally well agreed upon, there is some evidence that a small degree of ordering may actually be present among the U atoms located in the B-sites of the structure. The δ-U-$Zr_2$ phase is formed by means of an omega transformation mechanism in which alternating (111) planes in the bcc γ phase collapse to form the basal planes of the hexagonal δ phase structure [252]. Using a semi-empirical modified embedded atom method (MEAM) with molecular dynamics (MD) and Monte Carlo (kMC) simulations Moore *et al.*[221,225] found that there was a thermodynamic driving force towards ordered structures in the U-Zr system. Specifically, in the bcc γ phase, it was found that while there was a preference for U atoms to be third or fourth nearest neighbors (3NN or 4NN), 1NN U atoms were still occasionally present and that the

presence of these 1NN U atoms at the beginning of the omega transformation resulted in an ordered δ-U-$Zr_2$ structure being more readily formed than the partially disordered structure which only formed when there were no 1NN U atoms present at the start of the transformation.

Previous computational studies on the δ-U-$Zr_2$ structure were either limited in scope or did not bother to examine the specific ordering nature in the phase. In the only study to investigate ordering, Landa *et al*. [235] used a Korringa-Kohn-Rostoker method within the atomic-sphere approximation (KKR-ASA) combined with the coherent potential approximation (CPA) and the scalar-relativistic exact muffin-tin orbital method (EMTO) to investigate groundstate properties of the γ-U-Zr and δ-U-$Zr_2$ phases including ordering and found that Zr d-band occupancy could be directly correlated to the stability of the δ phase. Ordering in the δ phase was investigated by calculating and comparing total energies for three different configurations of U and Zr among the Al and B sites in the unit cell and it was found that the configuration depicting the partially ordered structure, with random B site occupations, was lowest in energy and the most stable. The two other configurations modelled, however, one which was a totally random structure with U and Zr atoms dispersed over all sites and the other consisting of a complete ordering in which the Al-sites were occupied by U atoms and the B-sites were occupied by Zr, represent the virtual extremes at the bounds of the disorder/order range. While the perceived stability of the partially ordered structure agreed with experiment it does not necessarily disprove the notion that some form or level of short-range order may exist amongst the U atoms in the B-sites.

### *6.1.3 δ-U-$Zr_2$ Modelling*

In this work the ordering behavior of δ-U-$Zr_2$ is investigated by calculating formation enthalpies for a series of supercell structures with ordered configurations of the B-site positions using standard plane-wave pseudopotential-based DFT. The enthalpy of formation, defined as the change in enthalpy associated with the formation of one mole of a substance from its base constituents, is used to compare the relative stabilities of each ordered supercell structure. In DFT terms, for a compound $A_{(1-x)}B_x$, where x is the mole fraction, the formation enthalpy, $E^{form}_{A_{(1-x)}B_x}$, is defined as:

$$E^{form}_{A_{(1-x)}B_x} = E^0_{A_{(1-x)}B_x} - (1-x)E^0_{A_{gs}} - xE^0_{B_{gs}} \quad (41)$$

Where $E^0_{A_{(1-x)}B_x}$ is total energy per atom calculated in a DFT simulation of the compound $A_{(1-x)}B_x$ and $E^0_{A_{gs}}$ and $E^0_{B_{gs}}$ are the total energies per atom calculated for the groundstate reference systems of the constituents A and B. Since DFT calculations are performed at 0 K, the calculated total energy is equivalent to the internal energy, $U$, of a system.

Partially ordered structures are constructed out of 1x1x1, 2x2x2 and 3x3x3 supercells based on the C32 ($AlB_2$ prototype). In these structures, the Al sites are always occupied Zr atoms, while the B sites are randomly occupied by U and Zr atoms, in a 50/50 (B-site) composition, corresponding to a U-66at%Zr overall composition. A totally random structure, in which both sites share a random occupation of U and Zr, and also exhibited the same U-66at%Zr composition, is also modelled for the 3x3x3 sized supercell as well.

## 6.2 Computational Methods

### *6.2.1 DFT Parameters*

The DFT simulations were performed using the Vienna *ab initio* Simulation Package (VASP) [15–18] with a variety of pseudopotentials using the projector augmented wave (PAW) method [19,20]. The calculations were performed using the Perdew-Burke-Ernzerhof (PBE) [11] exchange-correlation functional. The uranium PAW pseudopotential was modeled with the $6s^2$ $6p^6$ $5f^3$ $6d^1$ $7s^2$ valence electronic configuration and a core represented by [Xe, 5d, 4f], and the zirconium PAW pseudopotential was modeled with the $4s^2$ $4p^6$ $4d^2$ $5s^2$ valence electronic configuration and a core represented by [Ar, 3d]. The maximum energy cutoff of the plane-wave basis set found to be necessary to minimize the energy was 450 eV. Partial orbital occupancies were set according to the smearing method of Methfessel-Paxton of order one [66], with a smearing width of 0.2 eV. Spin polarization effects were not included in any of these calculations.

### *6.2.2 Partially Ordered Supercell Structures*

Eight supercells were modelled in total. These include one 1x1x1 unit cell sized structure containing 3 atoms (1U, 2Zr), five ordered 2x2x2 supercells each containing 24 atoms (8U,16Zr), one ordered 3x3x3 supercell and one randomly ordered (B-site only) 3x3x3 supercell each containing 81 atoms (27U, 54Zr). A k-point mesh of 16x16x22 was used for the single 1x1x1 unit cell structure, while a mesh 9x9x13 was used for the 2x2x2 supercells, and a mesh of 6x6x9 was used for the large 3x3x3 supercells.

The 1x1x1 single unit cell structure is shown in **Figure 6.2**, while each of the 2x2x2 ordered supercells are shown in **Figure 6.3**, **Figure 6.4** and **Figure 6.5**. Each of these ordered structures can be classified according the coordination of its U atoms, which is shown for each configuration in the right column. In these images, the range of visible atoms is increased and all Zr atoms are hidden. Bonds are drawn between neighboring atoms for all U-U pairs which are less than 4.5 Å apart. Drawing these images like this allows us to see the unique U-U coordination in each structure. Each consecutive ordered 2x2x2 supercell structure exhibits a greater number of U-U neighbors.

The ordered 3x3x3 unit cell consists of the same ordering as the primitive unit cell and the "Order 2" 2x2x2 supercell in which the U atoms are only coordinated with two other nearby uranium atoms.

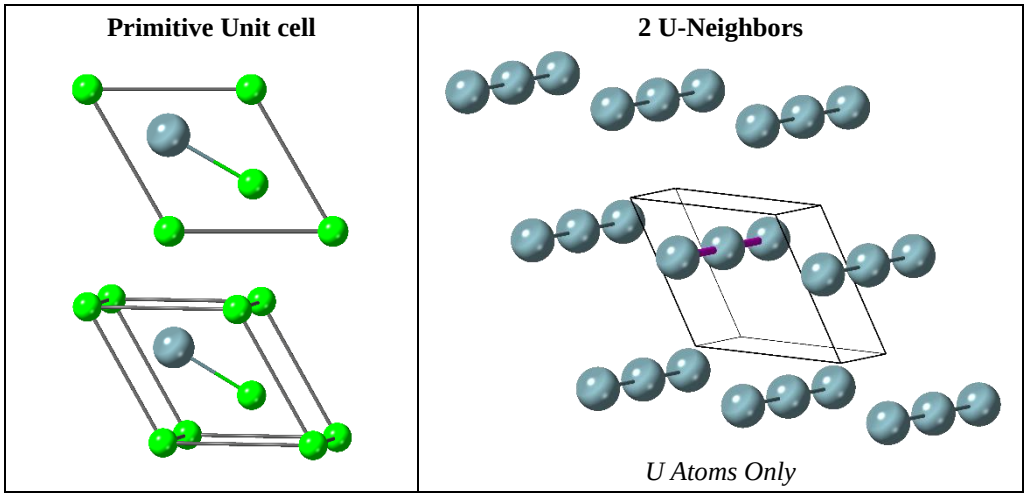


**Figure 6.2**. (left) Structure of the single δ-U-$Zr_2$ unit cell, with ordered B-sites, shown from two angles. (right) Zr atoms have been hidden and the visible range has been increased to show that U atoms typically neighbor on two other U atoms within a 4.5 Å radius shell. The U-U coordination of one atom is highlighted by purple colored bonds.

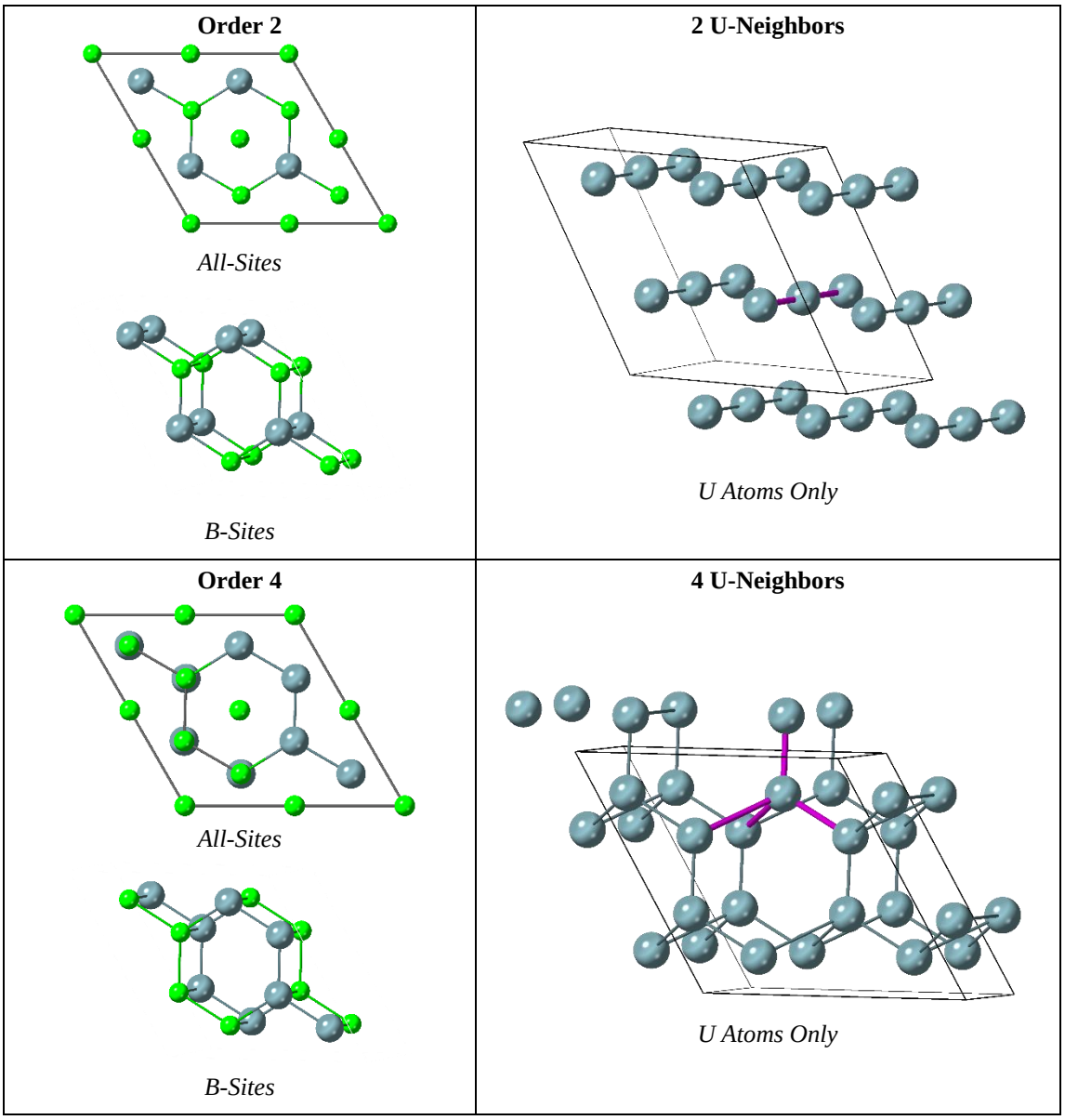


**Figure 6.3.** (left) Structure of the 2x2x2 δ-U-$Zr_2$ ordered supercells, shown from two angles. In the second angle (on the bottom) the Al sites have been hidden leaving only the interior B-sites visible. (right) Zr atoms have been hidden and the visible range has been increased to show number of U-U neighbors within a shell of 4.5 Å. The U-U coordination of one atom is highlighted by purple colored bonds.

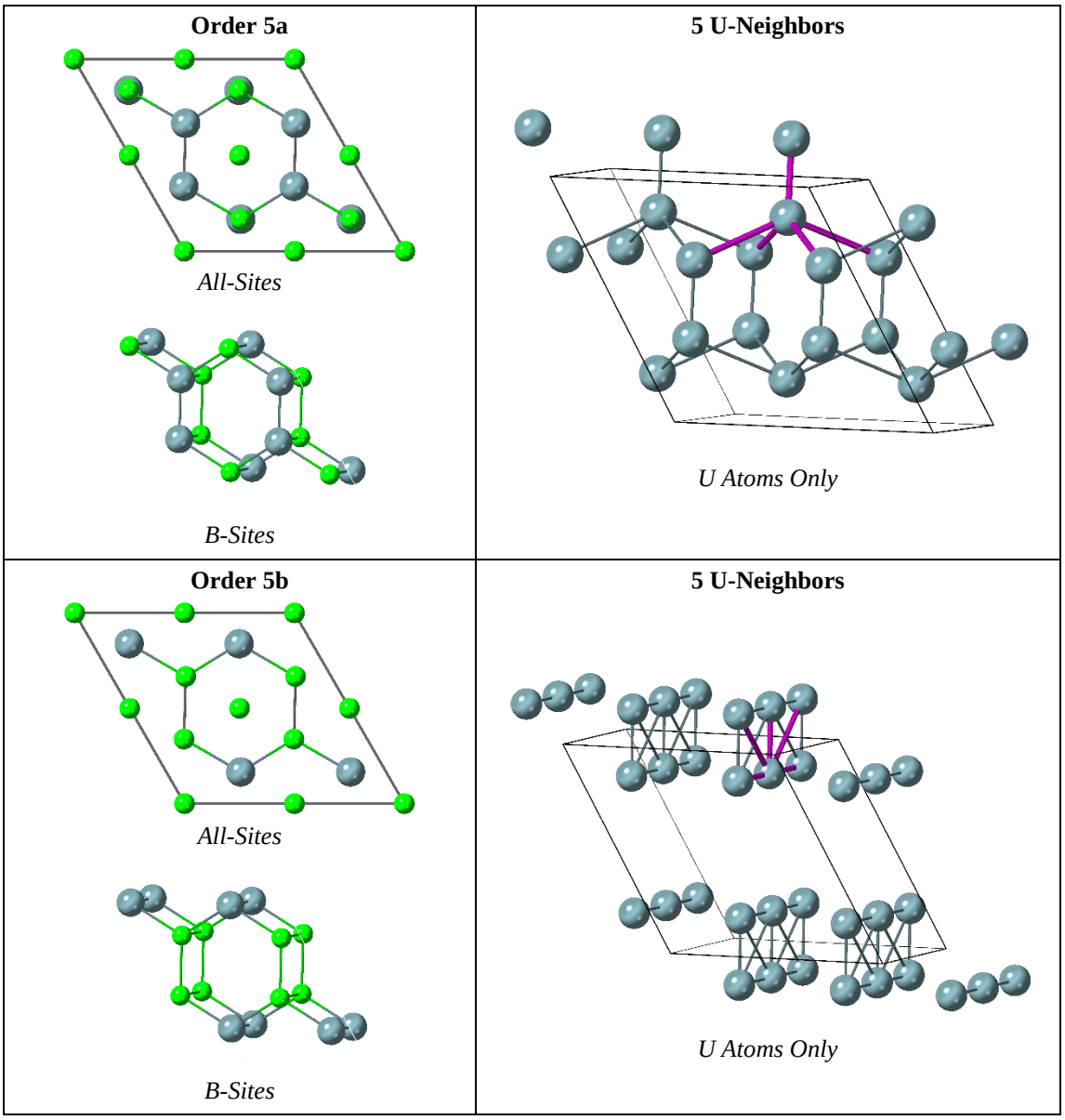


**Figure 6.4.** (*continued*) (left) Structure of the 2x2x2 δ-U-$Zr_2$ ordered supercells, shown from two angles. In the second angle (on the bottom) the Al sites have been hidden leaving only the interior B-sites visible. (right) Zr atoms have been hidden and the visible range has been increased to show number of U-U neighbors within a shell of 4.5 Å. The U-U coordination of one atom is highlighted by purple colored bonds.

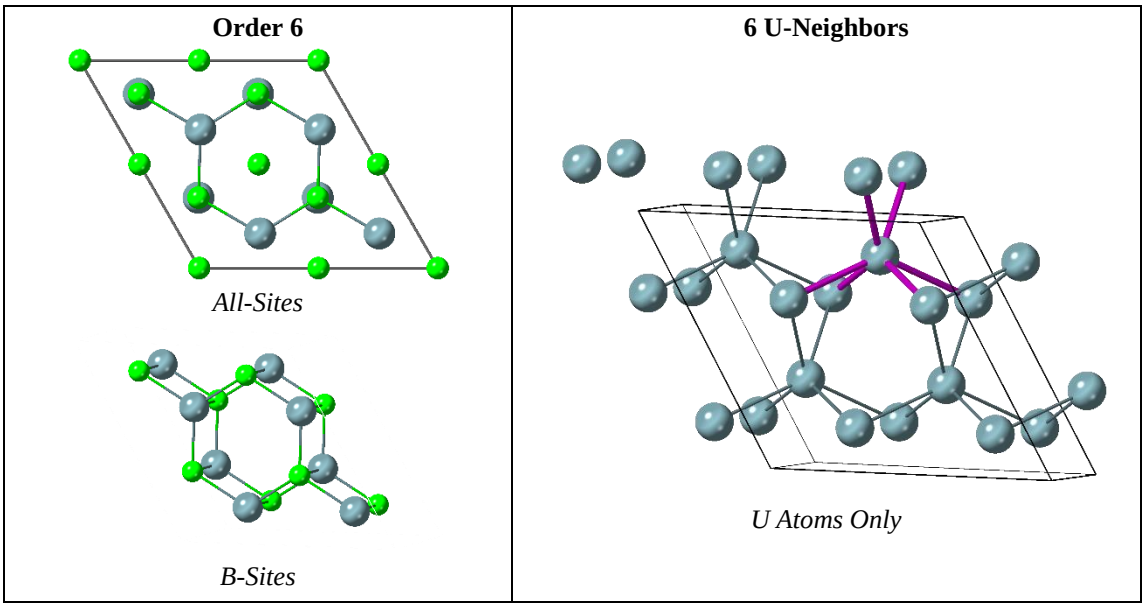


**Figure 6.5**. (*continued*) (left) Structure of the 2x2x2 δ-U-$Zr_2$ ordered supercells, shown from two angles. In the second angle (on the bottom) the Al sites have been hidden leaving only the interior B-sites visible. (right) Zr atoms have been hidden and the visible range has been increased to show number of U-U neighbors within a shell of 4.5 Å. The U-U coordination of one atom is highlighted by purple colored bonds.

## 6.3 Results and Discussion

### *6.3.1 Formation Enthalpies*

The calculated formation enthalpies and relaxed lattice constants of each structure are presented in **Table 6.1**. As can be seen there does not appear to be any obvious or apparent trend in regard to the coordination of U atoms and the formation of enthalpy. The lowest formation enthalpy (0.1055 eV) corresponded to the order 5b structure, in which each U had 5 other U neighbors within the 4.5 Å shell, while the highest enthalpy (0.4147 eV) was found for the order 6 structure with 6 neighboring U atoms. The lowest U coordinated structure (order 2) was found to have a formation enthalpy of 0. 2382 eV,

which was near the middle of the range. Interestingly for this order 2 structure, though, which was modelled for all three sizes of supercell, the energy of the smallest cell (the single unit cell) was slightly different than the energies found for the 2x2x2 and 3x3x3 versions. This indicates the single unit cell may not be large enough to truly minimize the energy in this system, which may indicate that short-range ordering effects, which could extend beyond the size of the primitive cell, actually are influencing the groundstate energy. Another interesting observation from these formation enthalpies is that the large 3x3x3 random supercell produced a fairly low enthalpy, relative to the other "ordered" enthalpies. This may actually suggest a random ordering truly is necessary for phase stability.

Unfortunately, none of the predicted formation enthalpies come close to the experimentally determined enthalpies, which are both in the negative. The positive formation enthalpies calculated through for these structures actually suggest that this phase is unstable and should decompose into the groundstate α-U and α-Zr structures. This, however, is not the experimentally observed case, which suggests these simple DFT calculations may not be enough to accurately model this system. Three possibilities arise from this: (1) the phase truly is random and the imposed "order" is driving the energy up, (2) the level of DFT formulation is not sufficient for modeling this system (*i.e.,* Hubbard corrections or spin-orbit coupling effects may need to included), or (3) the short-range ordering effects may extend beyond the dimensions of these supercells and so are not accounted for in these simulations (*i.e.,* larger supercells may lower the formation enthalpy further).

**Table 6.1.** Calculated lattice constants ($a_0$ and $c_0$) and enthalpy of formation for each ordered structure. The first set of $a_0$ and $c_0$ constants refer to the simulation supercell size and the second set, denoted by "Prim." refer to the size of the primitive unit cell within the supercell.

| | | | | | Prim. $a_0$ (Å) | Prim. $c_0$ (Å) | $a_0/c_0$ | Enthalpy of Formation (eV) |
|---|---|---|---|---|---|---|---|---|
| | | | | *Exp.* | 5.0271 [1] | 3.082 [1] | 0.613 | -0.04146 [3] |
| | | | | *Exp.* | 5.028 [2] | 3.09 [2] | 0.615 | -0.01347 [4] |
| Structure | | No. Atoms | a (Å) | C (Å) | prim $a_0$ (Å) | prim $c_0$ (Å) | $a_0/c_0$ | Enthalpy of Formation (eV) |
| 1x1x1 | unit cell | 3 | | | 5.065 | 3.033 | 0.599 | 0.2201 |
| 2x2x2 | order 5b | 24 | 10.198 | 6.122 | 5.099 | 3.061 | 0.600 | 0.1055 |
| | order 4 | 24 | 9.833 | 6.090 | 4.916 | 3.045 | 0.619 | 0.2144 |
| | order 5a | 24 | 10.168 | 6.164 | 5.084 | 3.082 | 0.607 | 0.2354 |
| | order 2 | 24 | 10.117 | 6.061 | 5.059 | 3.030 | 0.606 | 0.2382 |
| | order 6 | 24 | 10.152 | 6.128 | 5.076 | 3.064 | 0.599 | 0.4147 |
| 3x3x3 | ordered | 81 | 15.171 | 9.086 | 5.057 | 3.029 | 0.604 | 0.2376 |
| | random | 81 | 15.035 | 9.254 | 5.012 | 3.085 | 0.615 | 0.1289 |

[1] Okuniewski et al. [253,254]
[2] Akabori et al. [242,246]
[3] Nagarajan et al. [255]
[4] Ogawa [243]

### *6.3.2 U-U Dimerization*

The calculated formation enthalpies suggest larger supercell sizes might yield more accurate results. In order to understand why this may be the case, we can examine the local relaxation behavior of the atoms. What we see, in almost every case, is a dimerization of U-U neighbor pairs. What this means is that the U atoms that sit particularly close to one another tend to shift towards each other during relaxation, eventually forming a dimer pair within the lattice. This is observed in every modelled structure except for the order 6 structure, which showed the highest formation enthalpy, so it's likely that U dimerization leads to a decrease in system energy, and thus greater phase stability. In the 3x3x3 random supercell, when more than two U atoms are nearby each other (*i.e.*, a cluster) they all shifted towards the mid-point of the "cluster". It should not be forgotten that this 3x3x3 structure

showed a fairly low enthalpy relative to the others. This all suggests that in these DFT implementations the U atoms likely prefer to bond with other U atoms than Zr, and more tightly than the lattice site spacing allows for, and so more randomized structures result in more energy lowering U-U dimers and U-U-U+ clusters. This is also strengthened by the fact that the lattice constants of the random 3x3x3 structure were the closest to the known experimentally measured lattice constants [242,246,253,254].

Examples of the U-U dimerization in the Order 4 and Order 5b structures are shown in **Figure 6.6** and the U-U-U+ clustering in the 3x3x3 random supercell is shown in **Figure 6.7**. In these images the U-U dimers and U-U-U+ clusters are indicated by the red bonds, which are only drawn for the U-U bonds shorter than 2.8 Å that formed during relaxation. The U-U movement in these structures also caused some the Zr atoms, in both Al and B sites, to be pushed slightly out of their lattice site positions.

**Order 4 Structure**

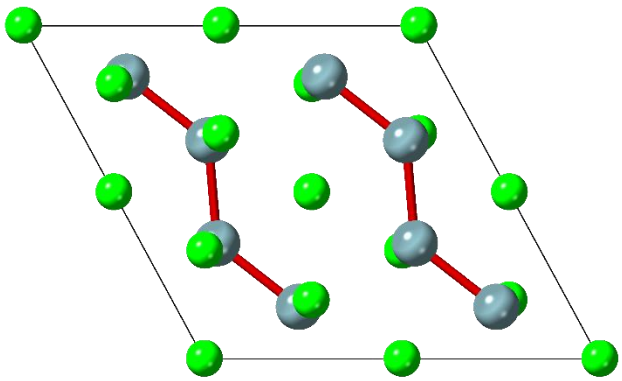

*<001> direction*

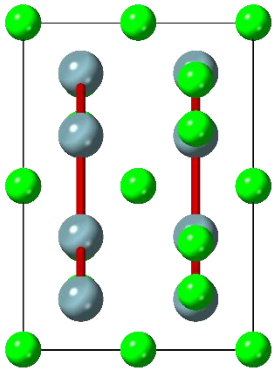

*<100> direction*

**Order 5b Structure**

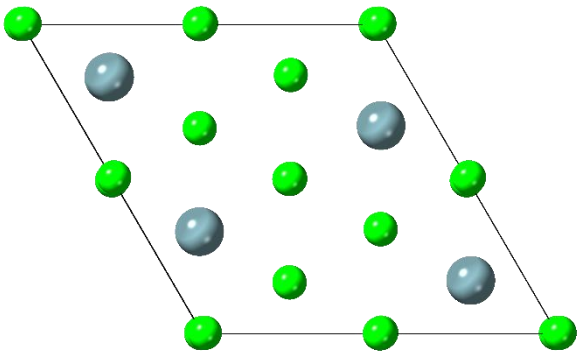

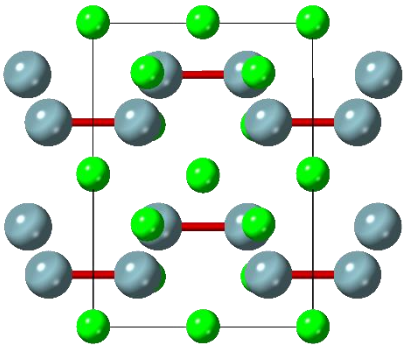

**Figure 6.6.** Dimerization behavior of U-U neighbors. Shown are front and side views of two of modelled structures; (top) the order 4 structure, and (bottom) the order 5b structure. U-U dimer pairs, which shifted towards each other during relaxation, are depicted by the red bonds. Bonds are only drawn for U-U bond distances shorter than 2.8 Å.

**3x3x3 Random Order Structure**

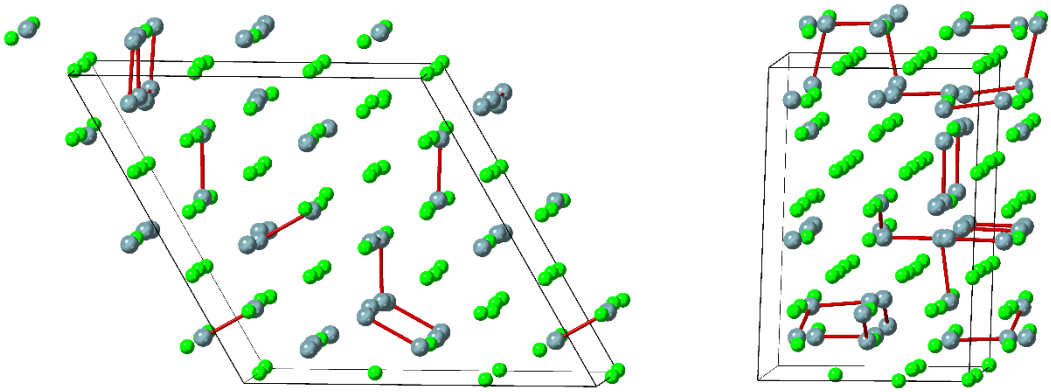

*<001> direction* *<100> direction*

**Figure 6.7.** U-U clustering in the random 3x3x3 supercell. Shown are front (left) and side (right) views of the relaxed structure. U-U dimer pairs and U-U-U+ clusters, which formed during relaxation, are depicted by the red bonds. Bonds are only drawn for U-U bond distances shorter than 2.8 Å.

Radial distribution functions (RDF) for each structure are also shown in **Figure 6.8**. These show the relative probability of finding any particle at distance, $r$, from another particle. Generally, very large supercells are needed to generate meaningful RDFs, so in the case of these relatively small supercell systems, trends are somewhat difficult to observe. What we can see fairly easily, however, is that the distribution in the structure with the lowest enthalpy (order 5b) shows the widest and shortest peaks, meaning a greater distribution of bond distances exists in this structure. Unfortunately, this trend does not carry over into the remaining RDFs, and so it's difficult to gauge whether this is correlated to the formation enthalpy.

| Structure | Radial Distribution Function, g(r) [units in Å] | Formation Enthalpy (eV) |
|---|---|---|
| Order 5b | 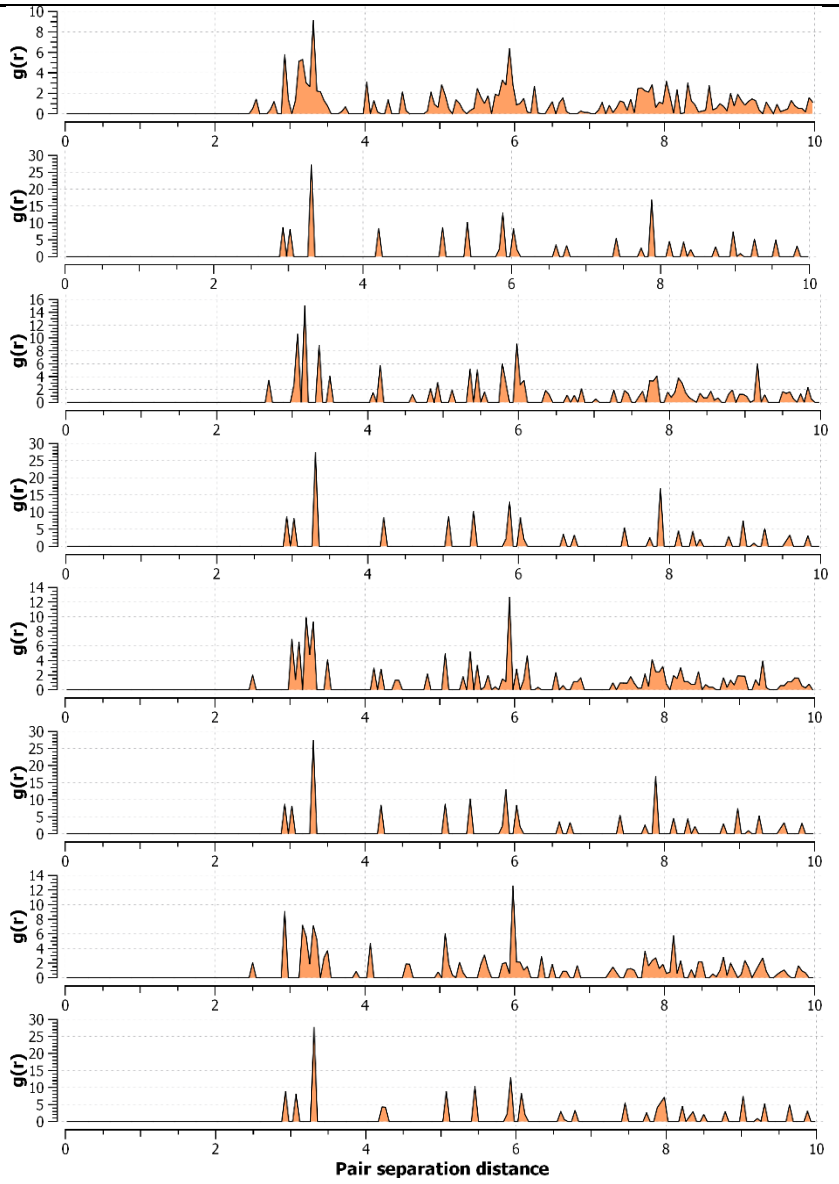 | 0.1055 |
| 3x3x3 random | | 0.1289 |
| Order 4 | | 0.2144 |
| Single Unit Cell (2) | | 0.2201 |
| Order 5a | | 0.2354 |
| 3x3x3 Ordered (2) | | 0.2376 |
| Order 2 | | 0.2382 |
| Order 6 | | 0.4147 |



**Figure 6.8.** Radial distribution functions (RDF), $\boldsymbol{g(r)}$, corresponding to each modeled structure. This shows the distribution of pair distances in each structure. They are listed in in order of formation enthalpy, from low to high.

### *6.3.3 DFT Uncertainty*

When it comes to predicting structural properties of metals DFT has generally performed well, even for heavier d-band metals with greater numbers electrons. Actinide

metals, however, which contain complex f-electrons, have not always received the same success. In general, DFT predications tend to deviate or err more in systems with increasing f-electron occupation, however, this associated error is generally small and treatable with higher levels of DFT approximation. For example, GGA functionals generally tend better predict the structural properties of U systems, such as volume and lattice constants, than LDA functionals [256,257]. On average, however, GGA's slightly underpredict actinide metal volumes, contrary to GGA volume predictions in other non-f-electron metals, which are usually slightly overpredicted [143]. In this work, we see more a varied outcome in lattice constant prediction. The $a_0$ constant is fairly consistently overpredicted by the PBE-GGA for most structures, while the $c_0$ constant is generally underpredicted. The resulting $c_0/a_0$ ratios are also generally underpredicted. Only the randomly ordered 3x3x3 supercell came close to experimental lattice constants and showed a slight underprediction in the $a_0$ constant, more in line with traditional U DFT predictions.

Volume under-prediction in these models is likely associated with the PAW method employed in the VASP framework and its ability to handle f-electron occupation. Full-potential linear muffin tin (FP-LMTO) methods have been able to avoid this this volume contraction in U-Zr [258] and Xie et al. showed that the magnitude of volume error decreases in the U-Zr systems with higher concentrations of Zr when using PAW methods [259]. These errors most likely stem from an under-prediction in f-electron occupation by PAW methods and so the overall errors on predicted properties are generally small because of the relatively low level of f-occupation in U [260,261]

Energy predictions, on the other hand, have been harder to quantify in U-Zr systems due to the lack of sufficient thermochemical data, particularly in relation to the δ-$UZr_2$

phase. Xie et al. found that PAW based DFT overpredicted mixing enthalpies in every U-Zr phase, not just in the δ-phase [259]. In this case even higher levels of DFT approximations may be needed, such as Hubbard +U corrections, or the inclusion of more fundamental effects, such as relativistic effects in the form of spin-orbit coupling (SOC). Xie et al. also included both of these in their study of the U-Zr system and found that the inclusion of both did improve mixing enthalpies. SOC by itself was found to slightly lower the mixing enthalpy while also increasing volume. The overall effect, however, was relatively minor, and so its computational burdensome inclusion in a simulation may not always be absolutely necessary, such as in computational heavy simulations containing large numbers of atoms and electrons. Significant changes did not occur until Hubbard +U corrections were included in addition to SOC effects. In these cases, with optimized Hubbard parameters, a negative mixing enthalpies were found for δ-$UZr_2$, however, the inclusion of the Hubbard +U correction also resulted in unrealistically large volumes [258,259]. The volume expansion was found to become greater with greater +U values.

Interestingly, while only cursorily studied, Xie et al. used an SQS approach to model the partial ordering in the δ-phase and indicated that a 16 atom supercell was at minimum necessary to minimize the their energies, relative to U ordering. While this doesn't immediately suggest even larger supercells may yield more accurate mixing enthalpy predictions, it does at least fall in line somewhat with the observations made in this work. It just may be that larger supercells in conjunction with SOC effects may be necessary to achieve more accurate predictions of energetic properties in U-Zr alloy. Full-potential methods, or all-electron methods, if computationally feasible to scale up in size may also

be an avenue worth exploring with the more modern computing power now more generally available.

## 6.4 Conclusion

Stemming from recent molecular dynamics investigations and diffraction experiments in the literature, some uncertainty has arisen regarding the exact atomic ordering of U atoms the δ-intermetallic phase of U-Zr alloys. This specific uncertainty is centered on the U and Zr occupation of the B-sites in the $AlB_2$ structure exhibited by the δ phase. In an attempt to investigate this potential ordering behavior, DFT simulations aimed at uncovering the true ordering behavior of the δ-U-$Zr_2$ phase were pursued in this study. This involved constructing a series of ordered supercell variants and then calculating the enthalpy of formation for each.

Calculated formation enthalpies showed no real trends in terms of U coordination within the modeled structures. Some results, however, did seem to suggest that a random occupation of U and Zr atoms in the B-sites might lead to the lowest overall enthalpies and thus more stable structures, such as the 3x3x3 randomly ordered supercell structure, which produced one of the lowest overall formation enthalpies.

Largely, though, these results appear to be mostly limited by the DFT implementation in this work, of which there are several things that could potentially lead to improved results. First, it may be that spin-orbit orbit coupling and or Hubbard corrections are necessary to properly model this U based system. Soderlind et al. [262][] and Xie et al. [45] both showed spin-orbit coupling did improve simulations, however, the improvement was not large, and the implementation of Hubbard corrections, is difficult,

time-consuming, and computationally expensive if done correctly. The Hubbard correction are also not guaranteed to improve accuracy, however, as Soderlind et al. also showed that these corrections applied to U-Zr DFT systems tended to spuriously over-predict volumes and lattice constants [262]. In the case of the models used in this work, the most obvious next step necessary to achieve greater accuracy and higher precision is the use of larger supercell sizes. Atomic ordering forces in the δ-U-$Zr_2$ phase may extend farther into the lattice than the simulation cells in this study could account for. Larger supercells, such as 4x4x4 or possibly even 5x5x5 supercells, could be used to model both truly random structures and more longer range variants of ordered structures. For this, however, greater computational resources are required.

# CHAPTER 7. CONCLUSIONS

In this thesis, structure-property relationships were investigated for a series of nuclear material systems using density functional theory (DFT). Each chapter presented a unique problem within the field of nuclear materials engineering and demonstrated the application of computational methods in support of existing experimental framework or in the guidance or suggestion of new experimental investigation.

The primary atomistic technique employed in this thses was density functional theory, which serves as an electronic structure modeling framework capable of solving for the groundstate electronic wavefunction of a collection or "system" of atoms. DFT solves for this wavefunction by solving the Kohn-Sham potential equations for a set atomic coordinates, which are derived after several successive, and exact, approximations to the Schrödinger equation are made, principal among these being the Born-Oppenheimer approximation and the single-particle mean field approximation for modeling many-body systems. The only inexact approximation, and the primary source of error in DFT is the exchange-correlation functional.

The modeling methods presented in each study demonstrate distinct DFT techniques. In study I, point defect formation energies were modelled for the fcc α- and bcc β-phases of Th metal. Defects included both Th-self defects and U impurity defects. An emphasis was placed on evaluating the performance of several popular versions of the exchange-correlation functional. These were the PBE, RPBE, and AM05 functionals. Since experimental defect formation energies in the Th system are rare, accuracy evaluation was based each functionals ability to reproduce known structural and elastic properties. In this

regard the PBE functional outperformed the other functionals. A logical next step for the direction of this work, would be to implement these calculated formation enthalpies in the development of higher order molecular dynamics (MD) or kinetic Monte Carlo (kMC) models which could then defect balances over time and under various operating conditions. Further DFT investigations could also be pursued which employ the use of nudge elastic band (NEB) theory to model the energy barriers associated with the migration and diffusion of these defects through a lattice, for more accurate defect concentration predictions.

In study II, the segregation of Cr in Ni surfaces is modeled using DFT. In this surface behavior investigation, surface slabs corresponding to the (100) and (111) surfaces of fcc Ni were first constructed and used to calculate the segregation energy corresponding to a single Cr moving from the bulk to the surface. An oscillatory behavior was observed in the top layers, in which the Cr exhibits a high positive energy in the first layer, and then a low negative energy in the second layer. In previous investigations, this behavior had most often been associated with the release of strain in the lattice that arose due to an atomic size mismatch. The mismatch between the size of Cr and Ni, however, is minimal at best, which suggest something else must be behind the buildup and eventual release of stress in the lattice. It was found in this case, that Cr is partially ionized by the Ni lattice, which strips the Cr atom of more than half an electron's worth of charge. This electronic charge transfer results the Cr and Ni interactions taking on a partially ionic-like nature which leads to additional stresses in the lattice. This stress was released by the lattice when the Cr resided in the top most layers which resulted in a decrease in the segregation energy for all but the topmost layer, which was dominated by relative surface energy effects. A next step in the evaluation of this oscillatory behavior would be to examine this charge transfer and

subsequent stress release effect in other alloy systems. Particularly, in those systems which exhibit this oscillatory segregation behavior but do not show an appropriate size mismatch.

In study III, the segregation behavior in Ni-Cr surfaces is further investigated by extending the models to include the effects of adsorbed salt species on the surface. The salt species, which were chosen to be representative of the most common salt components and impurities in a nuclear reactor style salt, were systematically adsorbed to onto the unique sites of the (100) Ni surface. Cr segregation was then modeled for each salt/site configuration. It was found that the salt impurities had the strongest effect on segregation behavior, relative to the natural salt components. Single anions, such as the halides in the salt, or the O of an $H_2O$ impurity were able to pull electron charge off of the Cr atom, which drove the stability of the system up, and segregation energy down. Salt cations had the effect of reducing the strength of this anion effect. This reducing effect was approximately equal for all salt-cation configurations, which was enough to almost totally nullify the Cr segregation promoting effects of the halide anions. For the O anion, however, who's effect was incredibly large compared to the halides, the cation influence was not enough to drive preferential Ni segregation back into favor. There are many directions one could look to as a next step in this study. Many questions remain about the behaviors observed in this study, like how the segregation of the single Cr atom might be affected by the addition of other Cr atoms to the surface, or how the Cr-salt interaction might behave in the near a vacancy at the surface. There is also still a question of how the Cr is actually removed from the surface, and so further studies could be directed at investigating Cr removal by extending these same types of DFT models to DFT-MD models which could provide for a much more realistic representation of the salt and account for the evolution of time.

In the fourth and final study, ordering behaviors in the δ phase of U-Zr alloy were investigated with DFT. Uncertainty regarding the exact ordering of the B-sites in the $AlB_2$ type structure exhibited by this U-Zr intermetallic phase had been caused by recently published molecular dynamics calculations. In an effort to investigate this behavior, several supercell structures were constructed to test and model the different variants of atomic ordering in this structure. To gauge the ordering tendency, formation enthalpies were calculated for each structure and compared with experimental values from literature. A conclusion on the overall ordering behavior was not found, however, as the formation enthalpies found for each structure were unable to be sufficiently correlated with any kind U coordination or order. Further investigation into this topic could be pursued by the inclusion and analysis of further approximations in the DFT implementation. Namely, through the inclusion of spin-orbit coupling effects and Hubbard +U corrections. Another avenue for extending this study would be the construction and modeling of larger supercells, which might be able to better account for longer-range ordering effects if present. It would also be possible to more accurately model the energy and enthalpies of truly random order with these larger supercells.

Density functional theory is a powerful computational tool which offers an opportunity to probe and study the most fundamental levels of behaviors and interactions that drive the most important processes in chemistry and solid-state physics. The application of DFT in nuclear related sciences is more than demonstrated by each of the four studies presented in this thesis, each which employ a unique modelling technique within the DFT framework to extract relevant and useful information from the once thought to be unsolvable electronic wavefunction. With the advent of quantum computing

appearing to be just on the horizon [263], which is expected to heavily benefit DFT type models in the form of much larger simulation sizes and greatly improved simulation speeds, DFT will undoubtedly reach an even greater level of success and achieve greater applicability in a far wider range of atomistic sciences. This boost in our ability to understand materials and their behaviors at a quantum level, will only serve to better our ability develop and employ higher order models (*e.g.*, MD , kMC, etc), paying dividends all the way up the chain towards our macroscopic understandings of material behaviors and workings.

# REFERENCES


[1] J.C. Slater, Note on hartree's method, Phys. Rev. 35 (1930) 210–211. https://doi.org/10.1103/PhysRev.35.210.2.

[2] P. Hohenberg, W. Kohn, Inhomogensous Electron Gas*, Phys. Rev. 136 (1964) B864-871. https://doi.org/10.1007/BF01198136.

[3] W. Kohn, L.J. Sham, Self-Consistent Equations Including Exchange and Correlation Effects*, Phys. Rev. 140 (1965) A1133–A1138.

[4] C.G. Broyden, A Class of Methods for Solving Nonlinear Simultaneous Equations, Math. Comput. 19 (1965) 577–593.

[5] P.H. Dederichs, R. Zeller, Self-consistency iterations in electronic-structure calculations, Phys. Rev. B. 28 (1983) 5462–5472. https://doi.org/10.1103/PhysRevB.28.5462.

[6] R.O. Jones, O. Gunnarsson, The density functional formalism, its applications and prospects, Rev. Mod. Phys. 61 (1989) 689–746.

[7] L. Hedin, B.I. Lundqvist, Explicit local exchange-correlation potentials, J. Phys. C Solid State Phys. 4 (1971) 2064–2083. https://doi.org/10.1088/0022-3719/4/14/022.

[8] D.M. Ceperley, B.J. Alder, Ground state of the electron gas by a stochastic method, Phys. Rev. Lett. 45 (1980) 566–569. https://doi.org/10.1103/PhysRevLett.45.566.

[9] J.P. Perdew, Y. Wang, Accurate and simple analytic representation of the electron-

gas correlation energy, Phys. Rev. B. 45 (1992) 13244–13249.

[10] A.D. Becke, Density-funnctional exchange-energy approximation with correct asymptotic behavior, Phys. Rev. A. 38 (1988) 3098–3100.

[11] J.P. Perdew, K. Burke, M. Ernzerhof, Generalized Gradient Approximation Made Simple John, Phys. Rev. Lett. 77 (1996) 3865–3868.

[12] H.J. Monkhorst, J.D. Pack, Special points for Brillouin-zone integrations, Phys. Rev. B. 16 (1976) 5188–5192.

[13] P.E. Blöchl, Generalized separable potentials for electronic-structure calculations, Phys. Rev. B. 41 (1990) 5414–5416. https://doi.org/10.1103/PhysRevB.41.5414.

[14] D. Vanderbilt, Soft self-consistent pseudopotentials in a generalized eigenvalue formalism, Phys. Rev. B. 41 (1990) 7892–7895.

[15] G. Kresse, J. Hafner, Ab initio molecular dynamics for liquid metals, Phys. Rev. B. 47 (1993) 558–561. https://doi.org/10.1103/PhysRevB.47.558.

[16] G. Kresse, J. Hafner, Ab initio molecular-dynamics simulation of the liquid-metalamorphous- semiconductor transition in germanium, Phys. Rev. B. 49 (1994) 14251–14269. https://doi.org/10.1103/PhysRevB.49.14251.

[17] G. Kresse, J. Furthmiiller, Efficiency of ab-initio total energy calculations for metals and semiconductors using a plane-wave basis set, Comput. Mater. Sci. 6 (1996) 15–50.

[18] G. Kresse, J. Furthmüller, Efficient iterative schemes for ab initio total-energy

calculations using a plane-wave basis set, Phys. Rev. B - Condens. Matter Mater. Phys. 54 (1996) 11169–11186. https://doi.org/10.1103/PhysRevB.54.11169.

[19] P.E. Blöchl, Projector augmented-wave method, Phys. Rev. B. 50 (1994) 17953–17979. https://doi.org/10.1103/PhysRevB.50.17953.

[20] G. Kresse, D. Joubert, From ultrasoft pseudopotentials to the projector augmented-wave method, Phys. Rev. B - Condens. Matter Mater. Phys. 59 (1999) 1758–1775. https://doi.org/10.1103/PhysRevB.59.1758.

[21] IAEA, Thorium Fuel Cycle - Potential Benefits and Challenges IAEA TECDOC 1450, IAEA Publ. (2005).

[22] J. Serp, M. Allibert, O. Beneš, S. Delpech, O. Feynberg, V. Ghetta, D. Heuer, D. Holcomb, V. Ignatiev, J.L. Kloosterman, L. Luzzi, E. Merle-Lucotte, J. Uhlíř, R. Yoshioka, D. Zhimin, The molten salt reactor (MSR) in generation IV: Overview and perspectives, Prog. Nucl. Energy. 77 (2014) 308–319. https://doi.org/10.1016/j.pnucene.2014.02.014.

[23] H. György, S. Czifrus, The utilization of thorium in Generation IV reactors, Prog. Nucl. Energy. 93 (2016) 306–317. https://doi.org/10.1016/j.pnucene.2016.09.007.

[24] R. Ramanna, S.M. Lee, The thorium cycle for fast breeder reactors, Pramana. 27 (1986) 129–137. https://doi.org/10.1007/BF02846334.

[25] B.R. Sehgal, J.A. Naser, C.-L. Lin, W.B. Loewenstein, Thorium-Based Fuels in Fast Breeder Reactors, Nucl. Technol. 35 (2017) 635–650.

https://doi.org/10.13182/nt77-a31872.

[26] H. Nifenecker, S. David, J.M. Loiseaux, O. Meplan, Basics of accelerator driven subcritical reactors, Nucl. Instruments Methods Phys. Res. Sect. A Accel. Spectrometers, Detect. Assoc. Equip. 463 (2001) 428–467. https://doi.org/10.1016/S0168-9002(01)00160-7.

[27] P. Rodriguez, C. V. Sundaram, Nuclear and materials aspects of the thorium fuel cycle, J. Nucl. Mater. 100 (1981) 227–249. https://doi.org/10.1016/0022-3115(81)90534-1.

[28] D.E. Peterson, The Th-U (Thorium-Uranium) system, Bull. Alloy Phase Diagrams. 6 (1985) 443–445. https://doi.org/10.1007/BF02869507.

[29] P. Chiotti, High Temperature Crystal Structure of Thorium, J. Electrochem. Soc. 101 (1954) 567. https://doi.org/10.1149/1.2781155.

[30] P.R. Roy, D.N. Sah, Irradiation behaviour of nuclear fuels, Pramana. 24 (1985) 397–421. https://doi.org/10.1007/BF02894841.

[31] A.T. Motta, D.R. Olander, eds., Light Water Reactor Materials Volume 1: Fundamentals, 1st ed., merican Nuclear Society, 2017.

[32] G.H. Vineyard, G.J. Dienes, The theory of defect concentration in crystals, Phys. Rev. 93 (1954) 265–268. https://doi.org/10.1103/PhysRev.93.265.

[33] M.J. Fluss, L.C. Smedskjaer, M.K. Chason, D.G. Legnini, R.W. Siegel, Measurements of the vacancy formation enthalpy in aluminum using positron

annihilation spectroscopy, Phys. Rev. B. 17 (1978) 3444–3455.

[34] M.J. Fluss, L.C. Smedskjaer, A new positron source for positron annihilation lifetime experiments, Appl. Phys. 18 (1979) 305–306. https://doi.org/10.1007/BF00885519.

[35] R.O. Simmons, R.W. Balluffi, Measurements of equilibrium vacancy concentrations in aluminum, Phys. Rev. 117 (1960) 52–61. https://doi.org/10.1103/PhysRev.117.52.

[36] W.E. Schoknecht, R.O. Simmons, H.C. Wolfe, M.G. Graham, H.E. Hagy, Thermal Vacancies and Thermal Expansion, in: AIP Conf. Proc. 3, American Institute of Physics, 1972: pp. 169–182. https://doi.org/10.1063/1.2948554.

[37] Y.A. Kraftmakher, Modulation method for measuring specific heat, High Temp. - High Press. V. 5 (1972) 433–454.

[38] K.F. McCarty, J.A. Nobel, N.C. Bartelt, Vacancies in solids and the stability of surface morphology, Nature. 412 (2001) 622–625. https://doi.org/10.1038/35088026.

[39] C. Freysoldt, B. Grabowski, T. Hickel, J. Neugebauer, G. Kresse, A. Janotti, C.G. Van De Walle, First-principles calculations for point defects in solids, Rev. Mod. Phys. 86 (2014) 253–305. https://doi.org/10.1103/RevModPhys.86.253.

[40] K. Matsunaga, T. Tanaka, T. Yamamoto, Y. Ikuhara, First-principles calculations of intrinsic defects in Al2O3 , Phys. Rev. B. 68 (2003) 1–9.

https://doi.org/10.1103/physrevb.68.085110.

[41] O. Eriksson, P. Söderlind, J.M. Wills, A.M. Boring, First principles studies of crystal structures of f elements, Phys. B Phys. Condens. Matter. 190 (1993) 5–11. https://doi.org/10.1016/0921-4526(93)90436-A.

[42] L. Nordström, J.M. Wills, P.H. Andersson, P. Söderlind, O. Eriksson, Spin-orbit coupling in the actinide elements: A critical evaluation of theoretical equilibrium volumes, Phys. Rev. B - Condens. Matter Mater. Phys. 63 (2001) 1–5. https://doi.org/10.1103/PhysRevB.63.035103.

[43] R. Devanathan, L. Van Brutzel, A. Chartier, C. Guéneau, A.E. Mattsson, V. Tikare, T. Bartel, T. Besmann, M. Stan, P. Van Uffelen, Modeling and simulation of nuclear fuel materials, Energy Environ. Sci. 3 (2010) 1406–1426. https://doi.org/10.1039/c0ee00028k.

[44] P. Söderlind, B. Sadigh, V. Lordi, A. Landa, P.E.A. Turchi, Electron correlation and relativity of the 5f electrons in the U–Zr alloy system, J. Nucl. Mater. 444 (2013) 356–358. https://doi.org/10.1016/j.jnucmat.2013.10.021.

[45] P. Söderlind, A. Landa, P.E.A. Turchi, Comment on “correlation and relativistic effects in U metal and U-Zr alloy: Validation of ab initio approaches,” Phys. Rev. B - Condens. Matter Mater. Phys. 90 (2014) 18–20. https://doi.org/10.1103/PhysRevB.90.157101.

[46] P. Söderlind, A. Landa, J.G. Tobin, P. Allen, S. Medling, C.H. Booth, E.D. Bauer, J.C. Cooley, D. Sokaras, T.C. Weng, D. Nordlund, On the valence fluctuation in the

early actinide metals, J. Electron Spectros. Relat. Phenomena. 207 (2016) 14–18. https://doi.org/10.1016/j.elspec.2015.11.014.

[47] A.E. Mattsson, J.M. Wills, Density functional theory for d- and f-electron materials and compounds, Int. J. Quantum Chem. 116 (2016) 834–846. https://doi.org/10.1002/qua.25097.

[48] P. Söderlind, David A. Young, Assessing Density-Functional Theory for Equation-Of-State, Computation. 6 (2018) 13. https://doi.org/10.3390/computation6010013.

[49] R.S. Rao, B.K. Godwal, S.K. Sikka, Thorium: A 5f-band metal at ultrahigh pressures, Phys. Rev. B. 46 (1992) 5780–5782. https://doi.org/10.1103/PhysRevB.46.5780.

[50] B. Johansson, R. Ahuja, O. Eriksson, J.M. Wills, Anomalous fcc Crystal Structure of Thorium Metal, Phys. Rev. Lett. 75 (1995) 3320–3323.

[51] P. Söderlind, O. Eriksson, J.M. Wills, A.M. Boring, Elastic constants of cubic f-electron elements: Theory, Phys. Rev. B. 48 (1993) 9306–9312. https://doi.org/10.1103/PhysRevB.48.9306.

[52] C.E. Hu, Z.Y. Zeng, L. Zhang, X.R. Chen, L.C. Cai, Phase transition and thermodynamics of thorium from first-principles calculations, Solid State Commun. 150 (2010) 393–398. https://doi.org/10.1016/j.ssc.2009.11.042.

[53] J. Bouchet, Lattice dynamics of <math display="inline"> <mi>α</mi> </math> uranium, Phys. Rev. B. 77 (2008) 024113.

https://doi.org/10.1103/PhysRevB.77.024113.

[54] J. Bouchet, R.C. Albers, Elastic properties of the light actinides at high pressure, J. Phys. Condens. Matter. 23 (2011). https://doi.org/10.1088/0953-8984/23/21/215402.

[55] J. Bouchet, F. Jollet, G. Zérah, High-pressure lattice dynamics and thermodynamic properties of Th: An ab initio study of phonon dispersion curves, Phys. Rev. B - Condens. Matter Mater. Phys. 74 (2006) 1–7. https://doi.org/10.1103/PhysRevB.74.134304.

[56] D.P. Daroca, Ab initio modeling of point defects, self-diffusion, and incorporation of impurities in thorium, Solid State Commun. 252 (2017) 11–15. https://doi.org/10.1016/j.ssc.2017.01.002.

[57] N. Troullier, Jose Lurs Martins, for Calculations, Phys. Rev. B. 43 (1991) 1993.

[58] R. Nazarov, T. Hickel, J. Neugebauer, Vacancy formation energies in fcc metals: Influence of exchange-correlation functionals and correction schemes, Phys. Rev. B - Condens. Matter Mater. Phys. 85 (2012) 1–7. https://doi.org/10.1103/PhysRevB.85.144118.

[59] A.E. Mattsson, R. Armiento, J. Paier, G. Kresse, J.M. Wills, T.R. Mattsson, The AM05 density functional applied to solids, J. Chem. Phys. 128 (2008). https://doi.org/10.1063/1.2835596.

[60] B. Hammer, L.B. Hansen, J.K. No, A new parametrization of exchange-correlation

generalized gradient approximation functionals, J. Chem. Phys. 59 (1999) 1–9. https://doi.org/10.1103/PhysRevB.59.7413.

[61] R. Armiento, A.E. Mattsson, Functional designed to include surface effects in self-consistent density functional theory, Phys. Rev. B - Condens. Matter Mater. Phys. 72 (2005) 1–5. https://doi.org/10.1103/PhysRevB.72.085108.

[62] H. Zhao, A. Chang, Y. Wang, First-principles study of the structural, elastic, and electronic properties of the cubic perovskite BaHfO_3, Appl. Phys. Lett. 92 (2008) 13. http://arxiv.org/abs/0809.3506.

[63] N. Bork, N. Bonanos, J. Rossmeisl, T. Vegge, Thermodynamic and kinetic properties of hydrogen defect pairs in SrTiO 3 from density functional theory, Phys. Chem. Chem. Phys. 13 (2011) 15256–15263. https://doi.org/10.1039/c1cp20406h.

[64] C. Ganeshraj, P.N. Santhosh, First-principles study of structural, electronic, vibrational, dielectric and elastic properties of tetragonal Ba2YTaO6, J. Appl. Phys. 116 (2014). https://doi.org/10.1063/1.4897452.

[65] A.E. Mattsson, R. Armiento, Implementing and testing the AM05 spin density functional, Phys. Rev. B - Condens. Matter Mater. Phys. 79 (2009) 1–13. https://doi.org/10.1103/PhysRevB.79.155101.

[66] M. Methfessel, A.T. Paxton, High-precision sampling for Brillouin-zone integration in metals, Phys. Rev. B. 40 (1989) 3616–3621. https://doi.org/10.1103/PhysRevB.40.3616.

[67] Y. Le Page, P. Saxe, Symmetry-general least-squares extraction of elastic data for strained materials from *ab initio* calculations of stress, Phys. Rev. B. 65 (2002) 104104. https://doi.org/10.1103/PhysRevB.65.104104.

[68] R. Hill, The Elastic Behaviour of a Crystalline Aggregate, Proc. Phys. Soc. A. A 65 (1952) 349–354.

[69] W. Voight, Lehrbuch der Kristallphysik, B. B. Teubner, Leipzig Und Berlin. 739 (1928).

[70] A. Reuss, Berechnung der Fließgrenze von Mischkristallen auf Grund der Plastizitätsbedingung für Einkristalle ., ZAMM - J. Appl. Math. Mech. / Zeitschrift Für Angew. Math. Und Mech. 9 (1929) 49–58. https://doi.org/10.1002/zamm.19290090104.

[71] M.A. Ghebouli, B. Ghebouli, M. Fatmi, First-principles calculations on structural, elastic, electronic, optical and thermal properties of CsPbCl3 perovskite, Phys. B Condens. Matter. 406 (2011) 1837–1843. https://doi.org/10.1016/j.physb.2011.02.040.

[72] O.L. Anderson, A Simplified Method for Calculating the Debye Temperature from Elastic Constants, J. Phys. Chem. Solids. 24 (1963) 909–917.

[73] P. Chiotti, High Temperature Crystal Structure of Thorium, J. Electrochem. Soc. 101 (1954) 567. https://doi.org/10.1149/1.2781155.

[74] K.A. Gschneider, Solid State Physics, 1964.

[75] P.E. Armstrong, O.N. Carlson, J.F. Smith, Elastic constants of thorium single crystals in the range 77-400°K, J. Appl. Phys. 30 (1959) 36–41. https://doi.org/10.1063/1.1734971.

[76] J. Frye, Interim Report on Metallurgy of Thorium and Thorium Alloys, Oak Ridge, TN, 1951.

[77] P. Soderlind, L. Nordstrom, L. Yongming, B. Johansson, Relativistic effects on the thermal expansion of the actinide elements, Phys. Revew B. 42 (1990) 4544–4552.

[78] M. Born, R.D. Misra, On the stability of crystal lattices., Math. Proc. Cambridge Philos. Soc. 36 (1940) 466–478. https://doi.org/10.1017/S0305004100017515.

[79] C. Zener, Relation between residual strain energy and elastic moduli, Acta Crystallogr. 2 (1949) 163–166. https://doi.org/10.1107/s0365110x49000448.

[80] S.M. Kim, J.A. Jackman, W.J.L. Buyers, D.T. Peterson, Vacancy formation energy in thorium by positron annihilation, J. Phys. F Met. Phys. 14 (1984) 2323–2328. https://doi.org/10.1088/0305-4608/14/10/011.

[81] S.M. Kim, W.J.L. Buyers, Vacancy formation energy in iron by positron annihilation, J. Phys. F Met. Phys. 8 (1978) 103–108. https://doi.org/10.1088/0305-4608/14/10/011.

[82] P. Schultz, T. Jackman, J. Fabian, E. Williams, J. MacDonald, I. MacKenzie, The composition dependence of the effective vacancy formation enthalpy in copper-rich brass as deduced from the threshold temperature for positron trapping in vacancies,

Can. J. Phys. 56 (2011) 1077–1083. https://doi.org/10.1139/p78-140.

[83] A.K. Bandyopadhyay, S.K. Sen, A Pseudopotential calculation of the self-interstitial formation energy in f.c.c. metals, Solid State Commun. 65 (1988) 543–545. https://doi.org/10.1016/0038-1098(88)90452-8.

[84] T.P.C. Klaver, J.H. Chen, Density functional theory study of alloy element interstitials in Al, J. Comput. Mater. Des. 10 (2003) 155–162. https://doi.org/10.1007/s10820-005-1526-5.

[85] N.Q. Lam, L. Dagens, N. V. Doan, Calculations of the properties of self-interstitials and vacancies in the face-centred cubic metals Cu, Ag and Au, J. Phys. F Met. Phys. 13 (1983) 2503–2516. https://doi.org/10.1088/0305-4608/13/12/009.

[86] K.W. Ingle, R.C. Perrin, H.R. Schober, Interstitial cluster in FCC metals, J. Phys. F Met. Phys. 11 (1981) 1161–1173. https://doi.org/10.1088/0305-4608/11/6/004.

[87] S. Han, L.A. Zepeda-Ruiz, G.J. Ackland, R. Car, D.J. Srolovitz, Self-interstitials in V and Mo, Phys. Rev. B - Condens. Matter Mater. Phys. 66 (2002) 1–4. https://doi.org/10.1103/PhysRevB.66.220101.

[88] D. Nguyen-Manh, A.P. Horsfield, S.L. Dudarev, Self-interstitial atom defects in bcc transition metals: Group-specific trends, Phys. Rev. B - Condens. Matter Mater. Phys. 73 (2006) 4–7. https://doi.org/10.1103/PhysRevB.73.020101.

[89] C.C. Fu, F. Willaime, P. Ordejón, Stability and mobility of mono- and Di-interstitials in α-Fe, Phys. Rev. Lett. 92 (2004) 1–4.

https://doi.org/10.1103/PhysRevLett.92.175503.

[90] D. Finkenstadt, N. Bernstein, J.L. Feldman, M.J. Mehl, D.A. Papaconstantopoulos, Vibrational modes and diffusion of self-interstitial atoms in body-centered-cubic transition metals: A tight-binding molecular-dynamics study, Phys. Rev. B - Condens. Matter Mater. Phys. 74 (2006) 1–8. https://doi.org/10.1103/PhysRevB.74.184118.

[91] D. Connétable, É. Andrieu, D. Monceau, First-principles nickel database: Energetics of impurities and defects, Comput. Mater. Sci. 101 (2015) 77–87. https://doi.org/10.1016/j.commatsci.2015.01.017.

[92] X.T. Zu, L. Yang, F. Gao, S.M. Peng, H.L. Heinisch, X.G. Long, R.J. Kurtz, Properties of helium defects in bcc and fcc metals investigated with density functional theory, Phys. Rev. B - Condens. Matter Mater. Phys. 80 (2009) 1–6. https://doi.org/10.1103/PhysRevB.80.054104.

[93] Z.Q. Zhu, L. Yang, J.L. Nie, S.M. Peng, X.G. Long, X.S. Zhou, X.T. Zu, F. Gao, Ab initio study of He point defects in fcc Au-Ag alloys, J. Alloys Compd. 557 (2013) 5–10. https://doi.org/10.1016/j.jallcom.2012.12.118.

[94] Z.Q. Zhu, Y.L. Zhang, J.J. Xie, L. Yang, J.L. Nie, X.T. Zu, Ab initio study of He migrations in Fcc Au-Ag alloys, Acta Phys. Pol. A. 129 (2016) 1151–1154. https://doi.org/10.12693/APhysPolA.129.1151.

[95] M. David, D. Connétable, Diffusion of interstitials in metallic systems, illustration of a complex study case: Aluminum, J. Phys. Condens. Matter. 29 (2017).

https://doi.org/10.1088/1361-648X/aa8e5e.

[96] Q.F. Han, Z.Y. Zhou, Y. Ma, Y.L. Liu, A comparative investigation of the behaviors of H in Au and Ag from first principles, Model. Simul. Mater. Sci. Eng. 24 (2016). https://doi.org/10.1088/0965-0393/24/4/045009.

[97] Y. Zhang, W. Yang, Comment on "generalized gradient approximation made simple," Phys. Rev. Lett. 80 (1998) 890. https://doi.org/10.1103/PhysRevLett.80.890.

[98] G.. Deny, Surface segregation in binary metal alloys, in Handbook of Surfaces and Interfaces of Materials, Academic Press, 2001.

[99] D.A. Vermilyea, Physics of corrosion, Phys. Today. 29 (1976) 23–31. https://doi.org/10.1063/1.3023896.

[100] A.M. P. A. Dowben, Surface Segregation Phenomena, CRC Press, Boca Raton, Florida, 1990.

[101] J.A. Rodriguez, Physical and chemical properties of bimetallic surfaces, Surf. Sci. 24 (1996) 223–287.

[102] M. Polak, L. Rubinovich, The interplay of surface segregation and atomic order in alloys, Surf. Sci. Rep. 38 (2000) 127–194. https://doi.org/10.1016/s0167-5729(99)00010-2.

[103] A. V Ruban, H.L. Skriver, J.K. Nørskov, Surface segregation energies in transition-metal alloys, Phys. Rev. B - Condens. Matter Mater. Phys. 59 (1999) 15990–16000.

https://doi.org/10.1103/PhysRevB.59.15990.

[104] A. V. Ruban, H.L. Skriver, Calculated surface segregation in transition metal alloys, Comput. Mater. Sci. 15 (1999) 119–143. https://doi.org/10.1016/s0927-0256(99)00003-8.

[105] G. Treglia, B. Legrand, F. Ducastelle, Segregation and ordering at surfaces of transition metal alloys: The tight-binding ising model, Europhys. Lett. 7 (1988) 575–580. https://doi.org/10.1209/0295-5075/7/7/001.

[106] N. Martensson, H. B.Saalfeld, H. Kuhlenbeck, M. Neuman, Structural dependence of the 5d-metal surface energies as deduced from surface core-level shift measurements, 39 (1989) 8181–8186.

[107] M. Aldén, H.L. Skriver, B. Johansson, Surface core-level shifts for simple metals, Phys. Rev. B. 50 (1994) 12118–12130. https://doi.org/10.1103/PhysRevB.50.12118.

[108] M. Aldén, I.A. Abrikosov, B. Johansson, N.M. Rosengaard, H.L. Skriver, Self-consistent Green's-function technique for bulk and surface impurity calculations: Surface core-level shifts by complete screening, Phys. Rev. B. 50 (1994) 5131–5146. https://doi.org/10.1103/PhysRevB.50.5131.

[109] F.L. Williams, D. Nason, Binary alloy surface compositions from bulk alloy thermodynamic data, Surf. Sci. 45 (1974) 377–408. https://doi.org/10.1016/0039-6028(74)90177-0.

[110] Y.S. Ng, T.T. Tsong, S.B. McLane, Absolute composition depth profile of a NiCu alloy in a surface segregation study, Phys. Rev. Lett. 42 (1979) 588–591. https://doi.org/10.1103/PhysRevLett.42.588.

[111] T.S. King, R.G. Donnelly, Recent developments in modeling binary alloy surface segregation: Low index planes, steps, kinks, and chemisorption, Surf. Sci. 141 (1984) 417–454. https://doi.org/10.1016/0039-6028(84)90141-9.

[112] S.M. Foiles, Calculation of the surface segregation of Ni-Cu alloys with the use of the embedded-atom method, Phys. Rev. B. 32 (1985).

[113] J. Tersoff, Oscillatory segregation at a metal alloy surface: Relation to ordered bulk phases, Phys. Rev. B. 42 (1990) 10965–10968. https://doi.org/10.1103/PhysRevB.42.10965.

[114] M. Ren, J.H. Qin, J. B.Wang, T.T. Tsong, Oscillatory compositional depth profiles in surface segregation of a Pt-Rh alloy D., 47 (1993) 3944–3946.

[115] S. Zhao, Y. Osetsky, Y. Zhang, Preferential diffusion in concentrated solid solution alloys: NiFe, NiCo and NiCoCr, Acta Mater. 128 (2017) 391–399. https://doi.org/10.1016/j.actamat.2017.01.056.

[116] Y. Yu, W. Xiao, J. Wang, L. Wang, Understanding the surface segregation behavior of transition metals on Ni(111): A first-principles study, Phys. Chem. Chem. Phys. 18 (2016) 26616–26622. https://doi.org/10.1039/c6cp02983c.

[117] Y. Yu, W. Xiao, J. Wang, L. Wang, First-principles study of Mo segregation in

MoNi(111): Effects of chemisorbed atomic oxygen, Materials (Basel). 9 (2016) 21–23. https://doi.org/10.3390/ma9010005.

[118] R.N. Barnett, R.G. Barrera, C.L. Cleveland, U. Landman, Single-ion and pair-interaction potentials near simple metal surfaces, Phys. Rev. B. 28 (1983) 1667–1684. https://doi.org/10.1103/PhysRevB.28.1667.

[119] B. Legrand, G. Tréglia, F. Ducastelle, Phase transitions in surface segregation of PtcNi1-c alloys from tight-binding Ising-model calculations, Phys. Rev. B. 41 (1990) 4422–4434. https://doi.org/10.1103/PhysRevB.41.4422.

[120] N.N. Greenwood, A. Earnshaw, eds., 27 - Nickel, Palladium and Platinum, in: Chem. Elem., 2nd ed., Butterworth-Heinemann, Oxford, 1997: pp. 1144–1172. https://doi.org/https://doi.org/10.1016/B978-0-7506-3365-9.50033-X.

[121] N.N. Greenwood, A. Earnshaw, eds., 23 - Chromium, Molybdenum and Tungsten, in: Chem. Elem., 2nd ed., Butterworth-Heinemann, Oxford, 1997: pp. 1002–1039. https://doi.org/https://doi.org/10.1016/B978-0-7506-3365-9.50029-8.

[122] W. Tang, E. Sanville, G. Henkelman, A grid-based Bader analysis algorithm without lattice bias, J. Phys. Condens. Matter. 21 (2009). https://doi.org/10.1088/0953-8984/21/8/084204.

[123] E. Sanville, S.D. Kenny, R. Smith, G. Henkelman, Improved Grid-Based Algorithm for Bader Charge Allocation, J. Comput. Chem. 28 (2007) 899–908.

[124] G. Henkelman, A. Arnaldsson, H. Jónsson, A fast and robust algorithm for Bader

decomposition of charge density, Comput. Mater. Sci. 36 (2006) 354–360. https://doi.org/10.1016/j.commatsci.2005.04.010.

[125] M. Yu, D.R. Trinkle, Accurate and efficient algorithm for Bader charge integration, J. Chem. Phys. 134 (2011) 1–8. https://doi.org/10.1063/1.3553716.

[126] A. Dianat, J. Zimmermann, N. Seriani, M. Bobeth, W. Pompe, L.C. Ciacchi, Ab initio study of element segregation and oxygen adsorption on PtPd and CoCr binary alloy surfaces, Surf. Sci. 602 (2008) 876–884. https://doi.org/10.1016/j.susc.2007.12.016.

[127] G. Collinge, Y. Xiang, R. Barbosa, J.S. McEwen, N. Kruse, CO-induced inversion of the layer sequence of a model CoCu catalyst, Surf. Sci. 648 (2016) 74–83. https://doi.org/10.1016/j.susc.2015.10.014.

[128] F. Chen, R.L. Johnston, Charge transfer driven surface segregation of gold atoms in 13-atom Au-Ag nanoalloys and its relevance to their structural, optical and electronic properties, Acta Mater. 56 (2008) 2374–2380. https://doi.org/10.1016/j.actamat.2008.01.048.

[129] R.L. Johnston, L.O. Paz-Borbón, G. Barcaro, A. Fortunelli, Structural motifs, mixing, and segregation effects in 38-atom binary clusters, J. Chem. Phys. 128 (2008). https://doi.org/10.1063/1.2897435.

[130] S.B. Rao, R. Chowdhary, Evaluation on the Corrosion of the Three Ni-Cr Alloys with Different Composition, Int. J. Dent. 2011 (2011) 1–5. https://doi.org/10.1155/2011/397029.

[131] C.C. Chen, R.G.S. Chen, S. Te Huang, Effect of chemical composition on the corrosion behavior of Ni-Cr-Mo dental casting alloys, J. Biomed. Mater. Res. 60 (2002) 458–465. https://doi.org/10.1002/jbm.10080.

[132] T. Bellezze, G. Roventi, R. Fratesi, Electrochemical characterization of three corrosion-resistant alloys after processing for heating-element sheathing, Electrochim. Acta. 49 (2004) 3005–3014. https://doi.org/10.1016/j.electacta.2004.01.060.

[133] H. Liu, W. Sun, S. Xu, An extremely simple thermocouple made of a single layer of metal, Adv. Mater. 24 (2012) 3275–3279. https://doi.org/10.1002/adma.201200644.

[134] S.S. Raiman, G. Muralidharan, R.T. Mayes, J.M. Kurley, Compatibility Studies of Cladding Candidates and Advanced Low-Cr Superalloys in Molten NaCl-MgCl 2, 2019. www.osti.gov.

[135] S.S. Raiman, S. Lee, Aggregation and data analysis of corrosion studies in molten chloride and fluoride salts, J. Nucl. Mater. 511 (2018) 523–535. https://doi.org/10.1016/j.jnucmat.2018.07.036.

[136] C. Le Brun, Molten salts and nuclear energy production, J. Nucl. Mater. 360 (2007) 1–5. https://doi.org/10.1016/j.jnucmat.2006.08.017.

[137] F.Y. Ouyang, C.H. Chang, B.C. You, T.K. Yeh, J.J. Kai, Effect of moisture on corrosion of Ni-based alloys in molten alkali fluoride FLiNaK salt environments, J. Nucl. Mater. 437 (2013) 201–207. https://doi.org/10.1016/j.jnucmat.2013.02.021.

[138] A.E. Danon, O. Muránsky, I. Karatchevtseva, Z. Zhang, Z.J. Li, N. Scales, J.J. Kruzic, L. Edwards, Molten salt corrosion (FLiNaK) of a Ni–Mo–Cr alloy and its welds for application in energy-generation and energy-storage systems, Corros. Sci. 164 (2020). https://doi.org/10.1016/j.corsci.2019.108306.

[139] B.A. Pint, J.W. McMurray, A.W. Willoughby, J.M. Kurley, S.R. Pearson, M.J. Lance, D.N. Leonard, H.M. Meyer, J. Jun, S.S. Raiman, R.T. Mayes, Re-establishing the paradigm for evaluating halide salt compatibility to study commercial chloride salts at 600°C–800°C, Mater. Corros. (2019) 1–11. https://doi.org/10.1002/maco.201810638.

[140] M. Hofmeister, L. Klein, H. Miran, R. Rettig, S. Virtanen, R.F. Singer, Corrosion behaviour of stainless steels and a single crystal superalloy in a ternary LiCl-KCl-CsCl molten salt, Corros. Sci. 90 (2015) 46–53. https://doi.org/10.1016/j.corsci.2014.09.009.

[141] W. Ding, H. Shi, Y. Xiu, A. Bonk, A. Weisenburger, A. Jianu, T. Bauer, Hot corrosion behavior of commercial alloys in thermal energy storage material of molten MgCl2/KCl/NaCl under inert atmosphere, Sol. Energy Mater. Sol. Cells. 184 (2018) 22–30. https://doi.org/10.1016/j.solmat.2018.04.025.

[142] H. Sun, J. Wang, Z. Li, P. Zhang, X. Su, Corrosion behavior of 316SS and Ni-based alloys in a ternary NaCl-KCl-MgCl2 molten salt, Sol. Energy. 171 (2018) 320–329. https://doi.org/10.1016/j.solener.2018.06.094.

[143] A. Jain, G. Hautier, C.J. Moore, S. Ping Ong, C.C. Fischer, T. Mueller, K.A.

Persson, G. Ceder, A high-throughput infrastructure for density functional theory calculations, Comput. Mater. Sci. 50 (2011) 2295–2310. https://doi.org/10.1016/j.commatsci.2011.02.023.

[144] B. Legendre, M. Sghaier, Curie temperature of nickel, J. Therm. Anal. Calorim. 105 (2011) 141–143. https://doi.org/10.1007/s10973-011-1448-2.

[145] M.J. Besnus, Y. Gottehrer, G. Munschy, Magnetic Properties of Ni-Cr Alloys, 597 (1972).

[146] J.R. Thompson, A. Goyal, D.K. Christen, D.M. Kroeger, Ni-Cr textured substrates with reduced ferromagnetism for coated conductor applications, (2008).

[147] M. Aldén, H.L. Skriver, S. Mirbt, B. Johansson, Surface energy and magnetism of the 3d metals, Surf. Sci. 315 (1994) 157–172. https://doi.org/10.1016/0039-6028(94)90551-7.

[148] L. Vitos, A. V. Ruban, H.L. Skriver, J. Kollár, The surface energy of metals, Surf. Sci. 411 (1998) 186–202. https://doi.org/10.1016/S0039-6028(98)00363-X.

[149] J.M. Zhang, F. Ma, K.W. Xu, Calculation of the surface energy of bcc metals by using the modified embedded-atom method, Surf. Interface Anal. 35 (2003) 662–666. https://doi.org/10.1002/sia.1587.

[150] M.P.J. Punkkinen, Q.-M. Hu, S.K. Kwon, B. Johansson, J. Kollár, L. Vitos, Surface properties of 3d transition metals, Philos. Mag. 91 (2011) 3627–3640.

[151] W.R. Tyson, W.A. Miller, Surface Free Energies of Solid Metals. Estimation From

Liquid Surface Tension, Surf. Sci. 62 (1977) 267–276.

[152] S.P. Jeng, P.H. Holloway, C.D. Batich, Equilibrium surface segregation for Ni15%Cr(110), Surf. Sci. 193 (1988) 63–68. https://doi.org/10.1016/0039-6028(88)90437-2.

[153] J.H. DeVan, Effect of Alloying Additions on Corrosion Behavior of Nickel-Molybdenum Alloys in Fused Fluoride Mixtures, ORNL- TM- 2021, Oak Ridge, 1969. https://doi.org/ORNL-TM-2021.

[154] R.B. Briggs, Molten-Salt Reactor Program Semi-Annual Prgoress Report, Oak Ridge, 1964.

[155] Y.L. Wang, Q. Wang, H.J. Liu, C.L. Zeng, Effects of the oxidants H2O and CrF3 on the corrosion of pure metals in molten (Li,Na,K)F, Corros. Sci. 103 (2016) 268–282. https://doi.org/10.1016/j.corsci.2015.11.032.

[156] Y.L. Wang, Q. Wang, H.J. Liu, C.L. Zeng, Effect of grain refinement on the corrosion of Ni-Cr alloys in molten (Li,Na,K)F, Corros. Sci. 109 (2016) 43–49. https://doi.org/10.1016/j.corsci.2016.03.027.

[157] X.X. Ye, H. Ai, Z. Guo, H. Huang, L. Jiang, J. Wang, Z. Li, X. Zhou, The high-temperature corrosion of Hastelloy N alloy (UNS N10003) in molten fluoride salts analysed by STXM, XAS, XRD, SEM, EPMA, TEM/EDS, Corros. Sci. 106 (2016) 249–259. https://doi.org/10.1016/j.corsci.2016.02.010.

[158] L.C. Olson, J.W. Ambrosek, K. Sridharan, M.H. Anderson, T.R. Allen, Materials

corrosion in molten LiF-NaF-KF salt, J. Fluor. Chem. 130 (2009) 67–73. https://doi.org/10.1016/j.jfluchem.2008.05.008.

[159] L. Olson, K. Sridharan, M. Anderson, T. Allen, Intergranular corrosion of high temperature alloys in molten fluoride salts, Mater. High Temp. 27 (2010) 145–149. https://doi.org/10.3184/096034010X12743509428336.

[160] F.Y. Ouyang, C.H. Chang, J.J. Kai, Long-term corrosion behaviors of Hastelloy-N and Hastelloy-B3 in moisture-containing molten FLiNaK salt environments, J. Nucl. Mater. 446 (2014) 81–89. https://doi.org/10.1016/j.jnucmat.2013.11.045.

[161] A. Van De Walle, P. Tiwary, M. De Jong, D.L. Olmsted, M. Asta, A. Dick, D. Shin, Y. Wang, L.Q. Chen, Z.K. Liu, Efficient stochastic generation of special quasirandom structures, Calphad Comput. Coupling Phase Diagrams Thermochem. 42 (2013) 13–18. https://doi.org/10.1016/j.calphad.2013.06.006.

[162] W.B.A. Sharp, Incorporation of divalent cations in Cr2O3 during the oxidation of Fe-18%Cr-Ni alloys at 1123°, Corros. Sci. 10 (1970) 283–295. https://doi.org/10.1016/S0010-938X(70)80021-X.

[163] F.N. Mazandarany, R.D. Pehlke, THERMODYNAMIC PROPERTIES OF SOLID ALLOYS OF CHROMIUM WITH NICKEL AND IRON., Metall. Trans. 4 (1973) 2067–2076. https://doi.org/10.1007/BF02643269.

[164] S.J. Rothman, L.J. Nowicki, G.E. Murch, Self-diffusion in austenitic Fe-Cr-Ni alloys, J. Phys. F Met. Phys. 10 (1980) 383. https://doi.org/10.1088/0305-4608/10/3/009.

[165] M.S. Sohal, M.A. Ebner, P. Sabharwall, P. Sharpe, Engineering Database of Liquid Salt Thermophysical and Thermochemical Properties, INL/EXT-10-18297, Idaho Falls, 2010.

[166] D.F. Williams, Assessment of Candidate Molten Salt Coolants for the NGNP/NHI Heat-Transfer Loop, U.S. DEPARTMENT OF ENERGY, Oak Ridge, Tennesse, 2006. https://doi.org/ORNL/TM-2006/69.

[167] D.F. Williams, L. Toth, K. Clarno, Assessment of Candidate Molten Salt Coolants for the AHTR, Oak Ridge, Tennessee, 2006. https://doi.org/ORNL/TM-2006/69.

[168] C.W. Forsberg, P.F. Peterson, D.F. Williams, Practical Aspects of Liquid-Salt-Cooled Fast-Neutron Reactors, in: Proc. ICAPP'05, American Nuclear Society, Seoul, KOREA, 2005.

[169] B. Yildiz, M.S. Kazimi, Efficiency of hydrogen production systems using alternative nuclear energy technologies, Int. J. Hydrogen Energy. 31 (2006) 77–92. https://doi.org/10.1016/j.ijhydene.2005.02.009.

[170] D. LeBlanc, Molten salt reactors: A new beginning for an old idea, Nucl. Eng. Des. 240 (2010) 1644–1656. https://doi.org/10.1016/j.nucengdes.2009.12.033.

[171] Nuclear Energy Research and Development Roadmap: Report to Congress, 2010.

[172] W.R. Grimes, Chemical Research and Development for Molten-Salt Breeder Reactors, ORNL-TM-1853, (1967) 141. https://doi.org/ORNL-TM-1853.

[173] D.T. Ingersoll, C. Forsberg, P.E. MacDonald, Trade Studies for the Liquid-Salt-

Cooled Very High-Temperature Reactor: Fiscal Year 2006 Progress Report, OAK RIDGE, 2007. ftp://oesvr.ujv.cz/Liblice2011/CD/GIV-Reactor/02VHTR-doe/status_report_fy06_ornl-tm-2006-140.pdf.

[174] D.G. Lovering, R.J. Gale, Molten salt techniques. Vol. 1, (1983). https://inis.iaea.org/search/search.aspx?orig_q=RN:18057676 (accessed April 19, 2019).

[175] R. Kane, Molten Salt Corrosion, in: S. Cramer, B. Covino (Eds.), ASM Handb. VOL 13A Corros. – Fundam. Testing, Prot., ASM International, 2003: pp. 216–219.

[176] M.W. Rosenthal, P.N. Haubenreich, R.B. Briggs, The Development Status of Molten-Salt Breeder Reactors, Oak Ridge National Laboratory, Oak Ridge, 1972. http://moltensalt.org/references/static/downloads/pdf/ORNL-4812.pdf.

[177] D. Wen, B. Jiang, Q. Wang, F. Yu, X. Li, R. Tang, R. Zhang, G. Chen, C. Dong, Influences of Mo/Zr minor-alloying on the phase precipitation behavior in modified 310S austenitic stainless steels at high temperatures, Mater. Des. 128 (2017) 34–46. https://doi.org/10.1016/j.matdes.2017.04.095.

[178] C. Boulesteix, F. Pedraza, Characterisation of aluminium diffusion coatings elaborated on austenitic stainless steels and on ferritic-martensitic steels, Surf. Coatings Technol. 339 (2018) 27–36. https://doi.org/10.1016/j.surfcoat.2018.01.086.

[179] M. Bohra, P. Grammatikopoulos, R.E. Diaz, V. Singh, J. Zhao, J.F. Bobo, A. Kuronen, F. Djurabekova, K. Nordlund, M. Sowwan, Surface segregation in

chromium-doped NiCr alloy nanoparticles and its effect on their magnetic behavior, Chem. Mater. 27 (2015) 3216–3225. https://doi.org/10.1021/acs.chemmater.5b00837.

[180] M. Bohra, V. Singh, P. Grammatikopoulos, E. Toulkeridou, R.E. Diaz, J.F. Bobo, M. Sowwan, Control of Surface Segregation in Bimetallic NiCr Nanoalloys Immersed in Ag Matrix, Sci. Rep. 6 (2016) 1–8. https://doi.org/10.1038/srep19153.

[181] M. Bohra, P. Grammatikopoulos, V. Singh, J. Zhao, E. Toulkeridou, S. Steinhauer, J. Kioseoglou, J.F. Bobo, K. Nordlund, F. Djurabekova, M. Sowwan, Tuning the onset of ferromagnetism in heterogeneous bimetallic nanoparticles by gas phase doping, Phys. Rev. Mater. 1 (2017) 1–12. https://doi.org/10.1103/PhysRevMaterials.1.066001.

[182] X. Zhou, X.X. Yu, T. Kaub, R.L. Martens, G.B. Thompson, Grain Boundary Specific Segregation in Nanocrystalline Fe(Cr), Sci. Rep. 6 (2016) 1–14. https://doi.org/10.1038/srep34642.

[183] K. TAKAHASHI, Y. ISHIKAWA, T. YOSHIMURA, O. NISHIKAWA, a Study of Surface Segregation of a Type 304 Stainless Steel By Atom-Probe, Le J. Phys. Colloq. 47 (1986) C7-233-C7-237. https://doi.org/10.1051/jphyscol:1986740.

[184] E. Clauberg, C. Uebing, H.J. Grabke, Surface segregation on Fe-25% Cr-2% Ni-0.1% Sb single crystals, Surf. Sci. 433–435 (1999) 617–621. https://doi.org/10.1016/S0039-6028(99)00028-X.

[185] B. Johansson, N. Mårtensson, Core-level binding-energy shifts for the metallic

elements, Phys. Rev. B. 21 (1980) 4427–4457. https://doi.org/10.1103/PhysRevB.21.4427.

[186] B. Johansson, N. Mårtensson, Theory of surface core-level shifts in metals, Helv. Phys. Acta. 56 (1983).

[187] J.R. Chelikowsky, Predictions for surface segregation in intermetallic alloys, Surf. Sci. 139 (1984) 197–203. https://doi.org/10.1016/0039-6028(84)90047-5.

[188] P. Lambin, J.P. Gaspard, Analysis of the density of states of binary alloys: I. Comparison with the CPA, J. Phys. F Met. Phys. 10 (1980) 651–660. https://doi.org/10.1088/0305-4608/10/4/016.

[189] S. Mukherjee, J.L. Moran-Lopez, Charge transfer effects on the surface segregation in binary alloys, Prog. Surf. Sci. 25 (1987) 139–145. https://doi.org/10.1016/S0079-6816(87)80010-2.

[190] M. Brejnak, P. Modrak, Electronic theory of surface segregation for dilute transition metal alloys: predictions based on rigid-band-like approach, Surf. Sci. 247 (1991) 215–221. https://doi.org/10.1016/0039-6028(91)90129-G.

[191] P.M. Ossi, Surface segregation in transition metal alloys: Experiments and theories, Surf. Sci. 201 (1988) 519–531. https://doi.org/10.1016/0039-6028(88)90491-8.

[192] R. Riedinger and H. Dreysse, Electronic structure of dilute impurities near surfaces. An approach to dissolution and segregation energies, Phys. Rev. B. 27 (1983) 2073–2081.

[193] H. Dreysse and R. Riedinger, Surface-orientation dependence on the segregation energies of impurities, Phys. Rev. B. 28 (1983) 5669–5674.

[194] M. C. Desjonqueres, D. Spanjaard, Surface segregation in dilute binary fcc transition-metal alloys, Phys. Rev. B. 35 (1987) 952–965.

[195] M. Aldén, B. Johansson, H.L. Skriver, Surface shift of the occupied and unoccupied 4f levels of the rare-earth metals, Phys. Rev. B. 51 (1995) 5386–5396. https://doi.org/10.1103/PhysRevB.51.5386.

[196] I.A. Abrikosov, A. V. Ruban, H.L. Skriver, B. Johansson, Calculated orientation dependence of surface segregations in Pt50Ni50, Phys. Rev. B. 50 (1994) 2039–2042. https://doi.org/10.1103/PhysRevB.50.2039.

[197] A. Christensen, A. V Ruban, P. Stoltze, K.W. Jacobsen, H.L. Skriver, J.K. No, F. Besenbacher, Phase diagrams for surface alloys, Phys. Rev. B. 56 (1997) 5822–5834.

[198] B. Nonas, K. Wildberger, R. Zeller, P.H. Dederichs, Energetics of 3d Impurities on the (001) Surface of Iron, Phys. Rev. Lett. 80 (1998) 4574–4577. https://doi.org/10.1103/PhysRevLett.80.4574.

[199] J.W. Han, J.R. Kitchin, D.S. Sholl, Step decoration of chiral metal surfaces, J. Chem. Phys. 130 (2009). https://doi.org/10.1063/1.3096964.

[200] C. Jiang, B. Gleeson, Surface segregation of Pt in γ′-Ni3Al: A first-principles study, Acta Mater. 55 (2007) 1641–1647. https://doi.org/10.1016/j.actamat.2006.10.024.

[201] X. Zhang, J. Liu, J. Tang, L. Li, M. Chen, S. Liu, B. Zhu, Element segregation on the surfaces of pure aluminum foils, Appl. Surf. Sci. 256 (2010) 7300–7304. https://doi.org/10.1016/j.apsusc.2010.05.067.

[202] Y. Zhang, Z. Duan, C. Xiao, G. Wang, Density functional theory calculation of platinum surface segregation energy in Pt3Ni (111) surface doped with a third transition metal, Surf. Sci. 605 (2011) 1577–1582. https://doi.org/10.1016/j.susc.2011.05.032.

[203] K.J. Andersson, F. Calle-Vallejo, J. Rossmeisl, I. Chorkendorff, Adsorption-driven surface segregation of the less reactive alloy component, J. Am. Chem. Soc. 131 (2009) 2404–2407. https://doi.org/10.1021/ja8089087.

[204] C.A. Menning, J.G. Chen, General trend for adsorbate-induced segregation of subsurface metal atoms in bimetallic surfaces, J. Chem. Phys. 130 (2009). https://doi.org/10.1063/1.3125926.

[205] A. Dhouib, H. Guesmi, DFT study of the M segregation on MAu alloys (M = Ni, Pd, Pt) in presence of adsorbed oxygen O and O 2, Chem. Phys. Lett. 521 (2012) 98–103. https://doi.org/10.1016/j.cplett.2011.11.050.

[206] Y.R. Yin, C.L. Ren, H. Han, J.X. Dai, H. Wang, P. Huai, Z.Y. Zhu, First-principle atomistic thermodynamic study on the early-stage corrosion of NiCr alloy under fluoride salt environment, Phys. Chem. Chem. Phys. 20 (2018) 28832–28839. https://doi.org/10.1039/c8cp05045g.

[207] V. Marian, No Title, Ann. Phys. 7 (1937) 469.

[208] S. Sadron, No Title, Ann. Phys. 17 (1932).

[209] F.R. de Boer, R. Boom, W.C.M. Mattens, A.R. Miedema, A.K. Niessen, Cohesion in Metals, North-Holland, Amsterdam, 1988.

[210] H.L. Skriver, N.M. Rosengaard, Surface energy and work function of elemental metals, Phys. Rev. B. 46 (1992) 7157–7168.

[211] V.L. Moruzz, A.R. Williams, J.F. Janak, Local density theory of metallic cohesions V., Phys. Rev. B. 15 (1977) 2854–2857.

[212] M.S.S. Brooks, B. Johansson, Exchange integral matrices and cohesive energies of transition metal atoms, J. Phys. F Met. Phys. 13 (1983). https://doi.org/10.1088/0305-4608/13/10/003.

[213] G.L. Hofman, L.C. Walters, T. Bauer, Metallic Fast Reactor Fuels, Prog. Nucl. Energy. 31 (1997) 83–110. https://doi.org/10.1002/9783527603978.mst0105.

[214] C.E. Till, Y.I. Chang, W.H. Hannum, The intergral fast reactor-an overview, Prog. Nucl. Energy. 31 (2002) 3–11. https://doi.org/10.1016/0149-1970(96)00001-7.

[215] Y.-I. Chang, Technical Rationale for Metal Fuel in Fast Reactors, Nucl. Eng. Technol. 39 (2007) 161–170. https://doi.org/10.5516/net.2007.39.3.161.

[216] B. Blumenthal, The transformation temperatures of high-purity uranium, J. Nucl. Mater. 2 (1960) 23–30. https://doi.org/10.1016/0022-3115(60)90020-9.

[217] R.I. Sheldon, D.E. Peterson, The U-Zr (Uranium-Zirconium) system, Bull. Alloy Phase Diagrams. 10 (1989) 165–171. https://doi.org/10.1007/BF02881432.

[218] F.A. Rough, A.A. Bauer, Constitution of uranium and thorium alloys, Columbus, OH, 1958.

[219] J.H. Kim, K.H. Kim, C.B. Lee, Preparation of U-Zr-Mn, a Surrogate Alloy for Recycling Fast Reactor Fuel, Adv. Mater. Sci. Eng. 2015 (2015). https://doi.org/10.1155/2015/131704.

[220] C. Basak, G.J. Prasad, H.S. Kamath, N. Prabhu, An evaluation of the properties of As-cast U-rich U-Zr alloys, J. Alloys Compd. 480 (2009) 857–862. https://doi.org/10.1016/j.jallcom.2009.02.077.

[221] A.P. Moore, C. Deo, M.I. Baskes, M.A. Okuniewski, Atomistic mechanisms of morphological evolution and segregation in U-Zr alloys, Acta Mater. 115 (2016) 178–188. https://doi.org/10.1016/j.actamat.2016.05.052.

[222] J.T. McKeown, S. Irukuvarghula, S. Ahn, M.A. Wall, L.L. Hsiung, S. McDeavitt, P.E.A. Turchi, Coexistence of the α and δ phases in an as-cast uranium-rich U-Zr alloy, J. Nucl. Mater. 436 (2013) 100–104. https://doi.org/10.1016/j.jnucmat.2013.01.313.

[223] P. Chiotti, V. V Akhachinskij, I. Ansara, M.H. Rand, The chemical thermodynamics of actinide elements and compounds, IAEA, International Atomic Energy Agency (IAEA), 1981. http://inis.iaea.org/search/search.aspx?orig_q=RN:12640812.

[224] A.P. Moore, B. Beeler, M. Baskes, M. Okuniewski, C.S. Deo, Atomistic Ordering in Body Centered Cubic Uranium-Zirconium Alloy, MRS Proc. 1514 (2013) 27–35. https://doi.org/DOI: 10.1557/opl.2013.517.

[225] A.P. Moore, B. Beeler, C. Deo, M.I. Baskes, M.A. Okuniewski, Atomistic modeling of high temperature uranium-zirconium alloy structure and thermodynamics, J. Nucl. Mater. 467 (2015) 802–819. https://doi.org/10.1016/j.jnucmat.2015.10.016.

[226] B. Beeler, C. Deo, M. Baskes, M. Okuniewski, Atomistic properties of γ uranium, J. Phys. Condens. Matter. 24 (2012) 75401. https://doi.org/10.1088/0953-8984/24/7/075401.

[227] B. Beeler, C. Deo, M. Baskes, M. Okuniewski, First principles calculations of the structure and elastic constants of α, β and γ uranium, J. Nucl. Mater. 433 (2013) 143–151. https://doi.org/https://doi.org/10.1016/j.jnucmat.2012.09.019.

[228] S. Lu, H. Zhang, Q.M. Hu, M.P.J. Punkkinen, B. Johansson, L. Vitos, Magnetic effect on the interfacial energy of the Ni(1 1 1)/Cr(1 1 0) interface, J. Phys. Condens. Matter. 26 (2014). https://doi.org/10.1088/0953-8984/26/35/355001.

[229] C. Bin Zhang, X.P. Li, W.D. Li, P. Zhang, W. Yin, F. Wang, B.T. Wang, Structural, electronic, and elastic properties of equiatomic UZr alloys from first-principles, J. Nucl. Mater. 496 (2017) 333–342. https://doi.org/10.1016/j.jnucmat.2017.09.028.

[230] G.B. Fedorov, E.A. Smirnov, Thermodynamic properties of the γ-phase in the uranium-zirconium system, Sov. At. Energy. 21 (1966) 837–840. https://doi.org/10.1007/BF01125562.

[231] G.B. Fedorov, E.A. Smirnov, Heat capacity of uranium-zirconium systems, Sov. At. Energy. 25 (1968) 795–797. https://doi.org/10.1007/BF01114245.

[232] Y.A. Shevchuk, E.A. Smirnov, G.B. Fedorov, Thermodynamic properties of the uranium-zirconium alloys, Sov. At. Energy. 71 (1991) 642–646. https://doi.org/10.1007/BF01121655.

[233] L. Leibowitz, R.A. Blomquist, A.D. Pelton, Thermodynamics of the uranium-zirconium system, J. Nucl. Mater. 167 (1989) 76–81. https://doi.org/https://doi.org/10.1016/0022-3115(89)90426-1.

[234] H. Okamoto, U-Zr (uranium-zirconium), J. Phase Equilibria. 13 (2007) 109–110. https://doi.org/10.1007/BF02645399.

[235] A. Landa, P. Söderlind, P.E.A. Turchi, Density-functional study of the U-Zr system, J. Alloys Compd. 478 (2009) 103–110. https://doi.org/10.1016/j.jallcom.2008.12.052.

[236] G. Bozzolo, H.O. Mosca, A.M. Yacout, G.L. Hofman, Y.S. Kim, Surface properties, thermal expansion, and segregation in the U–Zr solid solution, Comput. Mater. Sci. 50 (2010) 447–453. https://doi.org/https://doi.org/10.1016/j.commatsci.2010.09.002.

[237] W. Xie, W. Xiong, C.A. Marianetti, D. Morgan, Correlation and relativistic effects in U metal and U-Zr alloy: Validation of *ab initio* approaches, Phys. Rev. B. 88 (2013) 235128. https://doi.org/10.1103/PhysRevB.88.235128.

[238] R.W. Buzzard, R.B. Liss, D.P. Fickle, The Uranium-Zirconium Binary System, J. React. Sci. Technol. 2 (1952).

[239] H.A. Saller, F.A. Rough, A.A. Bauer, The Uranium--- Zirconium Constitutional Diagram, BMI-824 (April, 1953). (1953).

[240] D. Peterson, Phase Studies of Uranium-Zirconium Alloys, (1950).

[241] W. Xiong, W. Xie, C. Shen, D. Morgan, Thermodynamic modeling of the U-Zr system - A revisit, J. Nucl. Mater. 443 (2013) 331–341. https://doi.org/10.1016/j.jnucmat.2013.07.034.

[242] M. Akabori, A. Itoh, T. Ogawa, F. Kobayashi, Y. Suzuki, Stability and structure of the δ phase of the U-Zr alloys, J. Nucl. Mater. 188 (1992) 249–254. https://doi.org/10.1016/0022-3115(92)90480-9.

[243] T. Ogawa, Free energy of formation of δ-UZr2 comment on the paper: K. Nagarajan, R. Babu and C.K. Mathews, Enthalpy of formation of UZr2 by calorimetry, J. Nucl. Mater. 209 (1994) 107–108. https://doi.org/10.1016/0022-3115(94)90251-8.

[244] J.M. Silcock, Intermediate Phase In The Uranium-Zirconium System-Discussion, Trans. Am. Inst. Min. Metall. Eng. 209 (1957) 521.

[245] E.R. Boyko, The structure of the δ phase in the uranium–zirconium system, Acta Crystallogr. 10 (2002) 712–713. https://doi.org/10.1107/s0365110x57002492.

[246] M. Akabori, T. Ogawa, A. Itoh, Y. Morii, The lattice stability and structure of delta -UZr2 at elevated temperatures, J. Phys. Condens. Matter. 7 (1995) 8249–8257. https://doi.org/10.1088/0953-8984/7/43/005.

[247] H.L. Yakel, A review of X-Ray difraction studies in Uranium alloys, Oak Ridge,

TN, 1974.

[248] W. Howlett, The Alloy System Uranium-Titanium-Zirconium, J. Nucl. Mater. 3 (1959) 289–299.

[249] A.G. Knapton, The crystal structure of TiU2, Acta Crystallogr. 7 (1954) 457–458. https://doi.org/10.1107/S0365110X54001405.

[250] R.E. Rundle, A.S. Wilson, The structures of some metal compounds of uranium, Acta Crystallogr. 2 (1948) 148–150. https://doi.org/10.1107/s0365110x49000400.

[251] H. Okamoto, Si-U (Silicon-uranium), J. Phase Equilibria Diffus. 34 (2013) 167–168. https://doi.org/10.1007/s11669-012-0183-0.

[252] C.B. Basak, N. Prabhu, M. Krishnan, On the formation mechanism of UZr2 phase, Intermetallics. 18 (2010) 1707–1712. https://doi.org/10.1016/j.intermet.2010.05.006.

[253] M.A. Okuniewski, Fabrication and Characterization of the High Flux Isotope Reactor Rabbit Specimens, Idaho Falls, 2012.

[254] M.A. Okuniewski, PIE Status Report on HFIR Metallic Fuel Specimens, Idaho Falls, 2014.

[255] K. Nagarajan, R. Babu, C.K. Mathews, Enthalpy of formation of UZr2 by calorimetry, J. Nucl. Mater. 203 (1993) 221–223. https://doi.org/10.1016/0022-3115(93)90378-C.

[256] P. Söderlind, O. Eriksson, B. Johansson, J.M. Wills, Electronic properties of f-

electron metals using the generalized gradient approximation, Phys. Rev. B. 50 (1994) 7291–7294. https://doi.org/10.1103/PhysRevB.50.7291.

[257] L. Vitos, J. Kollár, H.L. Skriver, Local density approximation versus generalized gradient approximation: Full charge density study of the atomic volume of the light actinides, J. Alloys Compd. 271–273 (1998) 339–341. https://doi.org/10.1016/S0925-8388(98)00084-X.

[258] P. Söderlind, A. Landa, P.E.A. Turchi, Comment on "correlation and relativistic effects in U metal and U-Zr alloy: Validation of ab initio approaches," Phys. Rev. B - Condens. Matter Mater. Phys. 90 (2014) 157101. https://doi.org/10.1103/PhysRevB.90.157101.

[259] W. Xie, W. Xiong, C.A. Marianetti, D. Morgan, Correlation and relativistic effects in U metal and U-Zr alloy: Validation of ab initio approaches, Phys. Rev. B - Condens. Matter Mater. Phys. 88 (2013) 235128. https://doi.org/10.1103/PhysRevB.88.235128.

[260] P. Söderlind, First-principles elastic and structural properties of uranium metal, Phys. Rev. B - Condens. Matter Mater. Phys. 66 (2002) 1–7. https://doi.org/10.1103/PhysRevB.66.085113.

[261] A.N. Chantis, R.C. Albers, M.D. Jones, M. Van Schilfgaarde, T. Kotani, Many-body electronic structure of metallic α -uranium, Phys. Rev. B - Condens. Matter Mater. Phys. 78 (2008). https://doi.org/10.1103/PhysRevB.78.081101.

[262] W. Xie, C.A. Marianetti, D. Morgan, Response to letter Electron correlation and

relativity of the 5f electrons in the U-Zr alloy system, J. Nucl. Mater. 476 (2016) 110–112. https://doi.org/10.1016/j.jnucmat.2016.04.043.

[263] R.P. Feynman, Simulating physics with computers, Int. J. Theor. Phys. 21 (1982) 467–488. https://doi.org/10.1007/BF02650179.